NEXRES 7 (2026) 101497

Contents lists available at ScienceDirect

Next Research

journal homepage: www.elsevier.com/locate/nexres

Voltage sensitive probes for membrane potential determination in life science

Alfons Penzkofer

Fakultät für Physik, Universität Regensburg, Universitätsstraße 31, D-93053 Regensburg, Germany

ARTICLE INFO

Keywords:
Electrophysiology
Optical electrophysiology
Electric field dependent molecular effects
Voltage sensitive dyes and nanoparticles
Genetically encoded voltage indicators (GEVIs)
Voltage-gated ion channels and phosphatases
Microbial rhodopsin-based voltage indicators

ABSTRACT

The membrane potential of a cell regulates several physiological processes. Membrane potential fundamentals are presented including electrophysiologic methods of membrane potential measurement. Voltage sensitive probes have been developed to record effects caused by membrane voltage changes. The electrical field dependent molecular effects used in optical membrane voltage determination are described. They comprise polar molecule effects, donor-acceptor pair effects (Förster-type resonant energy transfer, photoinduced electron transfer, photoinduced excited state intramolecular proton transfer), ground-state intermolecular proton transfer in genetically encoded microbial rhodopsins, and transmembrane helix strand displacement in voltage sensitive domains of genetically encoded voltage-gated ion channels and phosphatases. An overview of voltage sensitive probes is given, including voltage sensitive dyes, voltage sensitive semiconductor nanoparticles, fluorescent proteins, voltage-gated ion channels, voltage sensitive phosphatases, and microbial rhodopsins.

1. Introduction

Biological cells and cellular compartments are surrounded by membranes (cell membranes, plasma membranes) [1]. Intracellular and extracellular ionic concentration differences are managed by the selective permeable membrane lipid bilayer and the integral protein passive ion channels (passive transporters) and active ion pumps (active transporters) in the membrane [2]. They build up, maintain, and change an electrical potential difference (membrane voltage, more precise transmembrane electrical potential difference) between the cell inside and cell outside. The measurement of the membrane voltage and the monitoring of membrane voltage changes is essential in cell characterization and cell functioning studies and is the field of electrophysiology [3]. Optical electrophysiology [4,5] using voltage-sensitive indicators [6–8] enables multicellular *in vitro* and *in vivo* membrane voltage imaging [4–13].

Membrane potential fundamentals are presented in Section 2. There, the electrophysiologic methods of membrane potential measurement are included (glass microelectrode impalement in cell without voltage or current application, patch-clamp techniques with applied voltage or applied current, bioimpedance spectroscopy) [3]. In Section 3 electric field dependent molecular effects are described which are applied in optical membrane voltage monitoring with voltage sensitive probes. The various applied voltage sensitive probes are presented in Section 4.

Calcium ions are second messengers in cellular biology. They generate versatile intracellular signals to regulate cell function. The intracellular calcium concentration is nonlinearly influenced by the membrane potential. Calcium indicators (chemical Ca^{2+} indicators and

Abbreviations: Ace, *Acetabularia acetabulum*; Arch, Archaerhodopsin 3 from *Halorubrum sodomense*; ATP, Adenosine triphosphate; BP, bioluminescent protein; BR, bacteriorhodopsin from *Halobacterium salinarum*; BRET, bioluminescent resonant energy transfer; CB, conduction band; CFP, Cyan fluorescent protein; CI, Coulombic interaction; Ci-VSP, *Ciona intestinalis* voltage sensitive phosphatase; cpFP, circular-permuted fluorescent protein; CT, charge transfer state; DPA, dipicrylamine; ec, extracellular; ecFRET, electrochromic Förster-type resonant energy transfer; eoFRET, electro-orientational Förster-type resonant energy transfer; esFRET, electro-spatial Förster-type resonant energy transfer; ESIPT, excited-state intramolecular proton transfer; FP, fluorescent protein; FRET, Förster-type resonant energy transfer; GECI, genetically encoded calcium indicator; GEVI, genetically encoded voltage indicator; GFP, green fluorescent protein; Gg-VSP, *Gallus gallus* voltage sensitive phosphatase; GSPT, ground-state proton transfer; HOMO, highest occupied molecular orbital; ic, intracellular; LUMO, lowest unoccupied molecular orbital; Mac, *Leptosphaeria maculans*; MEA, multi-electrode array; PeT, photoinduced electron transfer; PeT_o, oxidative photoinduced electron transfer; PeT_r, reductive photoinduced electron transfer; PRSB, protonated retinal Schiff base; QCSE, quantum-confined Stark effect; QD, quantum dot; QR, quantum rod; REC, charge recombination; RFP, red fluorescent protein; RSB, retinal Schiff base; UCNP, upconversion nanoparticle; VB, valence band; VSD, voltage sensing domain; VSP, voltage sensing phosphatase; YFP, yellow fluorescent protein.

E-mail address: alfons.penzkofer@physik.uni-regensburg.de.

https://doi.org/10.1016/j.nexres.2026.101497
Received 2 December 2025; Received in revised form 6 February 2026; Accepted 13 February 2026
Available online 19 February 2026

genetically encoded Ca^{2+} indicators (GECIs)) are used to measure the calcium concentration. Monitoring the cytosolic Ca^{2+} content in nervous systems with GECIs has been applied to follow the neural activity in nervous systems [14–17]. Chemical Ca^{2+} indicators and genetically encoded Ca^{2+} indicators were described in [18] and are not further discussed here.

2. Membrane potential fundamentals

2.1. Membrane basics

Membranes function to organize biological processes by compartmentalizing them [19–22]. Every cell is enclosed in a cell membrane (also called plasma membrane). Plasma membranes are boundaries of a cell or of an organelle (functional compartments in an eukaryotic cell, like nuclei, mitochondria, chloroplasts, endoplasmic reticulum, Golgi apparatus). In animal cells, the cell membrane is the outermost layer which separates the cellular content (cytoplasmic region) from the external environment (plasma region). Plant cells, fungal cells and bacterial cells have a cell wall surrounding the cell membrane.

Both cell membranes and plasma membranes are selectively permeable (semipermeable) to molecules. The membranes have the structure of a lipid bilayer (phospholipids) with many types of large molecules embedded in it (integral proteins) and attached to it (peripheral proteins) [23]. The lipid bilayer has a high electric resistivity (no intrinsic permeability to ions). Some of the integral proteins are active transporters. They are capable of actively transporting solutes (like ions) through the membrane against a concentration gradient using the energy expenditure of ATP hydrolysis. To them belong ion pumps like Ca^{2+}-ATPase for Ca^{2+} transport, Na^+/K^+-ATPase for maintenance of Na^+ and K^+ gradients. Other integral proteins provide highly selective pores for passive transport of solutes (like ions) along the concentration gradient. They are passive transporters. To them belong ion channels like voltage-gated ion channels, external or internal ligand-gated ion channels, mechanical stress-gated ion channels, light-gated ion channels [24].

Membrane proteins play a crucial role in ensuring selective transport of molecules across membranes and controlling interactions between cells. They act as channels, pumps, receptors, enzymes, energy transduces. The selective permeability of the cell membrane is responsible for the regulation of basic cellular processes including endocytosis (uptake of macromolecules into the cell) and exocytosis (discharge of material from vesicles at the cell surface) [24].

According to the reaction of membranes to electrical stimuli, cells are characterized as electrically excitable cells and electrically non-excitable cells [20,21]. In excitable cells, an electrical stimulus, that changes the steady-state equilibrium membrane voltage (resting membrane potential U_{RP}) above a threshold value (action potential threshold U_{AT}), causes a nonlinear response of the transmembrane ion channels which leads to the generation of a transient membrane voltage spike, characterized by depolarization with positive overshoot, repolarization with negative overshoot (hyperpolarization) and recovery to the steady-state resting potential. The spiky membrane potential is called action potential [25]. To excitable cells belong nerve cells (neurons), cardiac muscle cells (cardiomyocytes), skeletal muscle cells, smooth muscle cells, secretory cells, touch receptor cells [26]. Non-excitable cells do not generate an action potential. In non-excitable cells, the steady-state equilibrium membrane voltage responses linear proportional to external electrical voltage impacts (generates a graded potential).

2.2. Extracellular and intracellular ion concentrations

The selective semipermeable lipid bilayer cell membrane with integral protein passive ion channels and active ion pumps stabilizes different extracellular (plasma) and intracellular (cytosolic) concentrations of Na^+, K^+, Ca^{2+}, Mg^{2+}, H^+ and Cl^-. Typical concentrations in cells of mammals are listed in Table 1 (taken from [27]).

2.3. Electric potential profile across membranes

The cell membranes are made of phospholipid bilayers consisting of charged head groups and a non-polar hydrocarbon interior. They are surrounded by extracellular plasma and intracellular cytosol. The electrical potential distribution $\Psi(x)$ across the lipid bilayer and the extracellular and intracellular surroundings is complex [28–32]. It is schematically displayed in Fig. 1a. The extracellular potential is set per definition to zero ($\Psi_{extracellular} = \Psi_{ec} = 0$). There are contributions from the surface potentials $\Delta\Psi_s$, the membrane lipid dipole potentials $\Delta\Psi_d$, and the transmembrane potential $\Delta\Psi_m = U_m = \Psi_{ic} - \Psi_{ec}$ ($\Psi_{ic}$is intracellular potential). U_m is called membrane voltage. The transmembrane potential (membrane voltage) $U_m = \Psi_{ic} - \Psi_{ec}$ is due to the differences in intracellular and extracellular ion concentration. The surface potential contributions $\Delta\Psi_s$at the solution-membrane interfaces are due to surface interaction of lipid headgroups with ions at the membrane-solution interface. The dipole potential contributions $\Delta\Psi_d$ at the membrane leaflets are caused by zwitterionic headgroups of the lipids (acting like parallel plate capacitors).

It depends on the electrical potential measurement technique what electrical potential at which position is probed or what potential difference between separate positions is measured, whether temporal potential changes or temporal potential difference changes are followed. Patch-clamp techniques measure the compartmental voltage difference between intracellular and extracellular spaces, i.e. they measure the transmembrane potential U_m at their microelectrode position [3]. Electric field sensitive dyes probe the local electric field at their local position in the membrane [29].

2.4. Membrane capacitor action and static transmembrane potential behavior

2.4.1. Membrane capacitor action

Considering the transmembrane potential behavior, the cell membrane (plasma membrane) may be described as a plate capacitor [3,20]. Only the phospholipid bilayer part is considered and treated as a plate capacitor consisting of two electrical conductors separated by a dielectric medium. The passive ion channels (leak channels) giving a resistor part and the active ion pumps giving a voltage source of the whole electrical circuit are not included [33]. The heterogenous non-polar hydrocarbon interior of lipids is considered as a homogenous dielectric medium [33]. The cell membrane voltage U_m is the electrical potential difference between membrane inside (intracellular) potential Ψ_{ic} and membrane outside (extracellular) potential Ψ_{ec}. In the cell membrane description as a plate capacitor the electrical potential distribution is simplified by a linear electrical potential distribution inside the membrane as displayed in Fig. 1b. The membrane voltage is determined by the quotient of stored charge $Q_{s,ic}$ at the intracellular membrane surface (equal to minus the stored charge $-Q_{s,ec}$ at the extracellular membrane surface) to the cell membrane capacitance C_m [33,34]. That

Table 1
Ionic concentrations in cells of mammals and corresponding Nernst equilibrium potentials for temperature $T = 37°C$ (taken from [27]).

Ion	Extracellular concentration c_{ec} (mM)	Intracellular concentration c_{ic} (mM)	Nernst equilibrium potential U_{Nernst} (mV)
Na^+	145	≈12	+67
K^+	4.5	≈150	-94
Ca^{2+}	≈1.5	$\approx 1 \times 10^{-4}$	+129
Mg^{2+}	≈0.5	≈0.5	0
Cl^-	115	≈10	-65
H^+	4×10^{-5}	$\approx 1 \times 10^{-4}$	-24

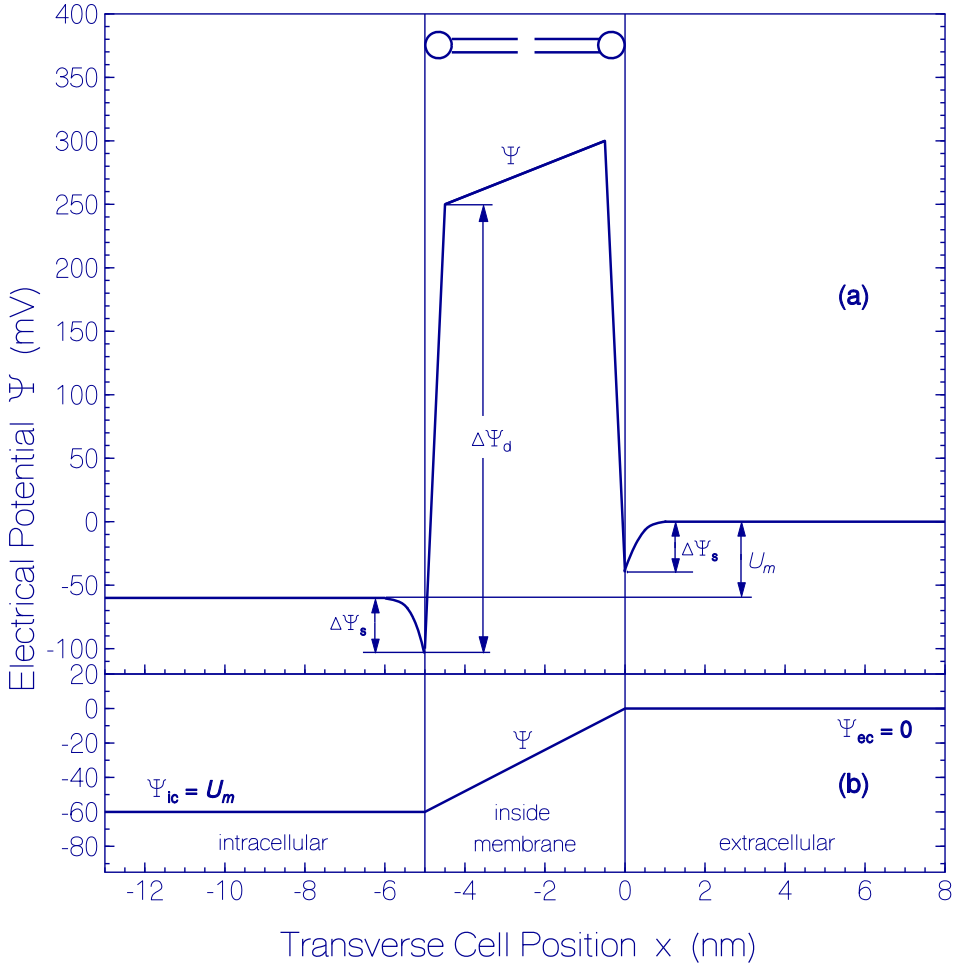

Fig. 1. **(a)** Typical electrical potential Ψ versus transverse cell position x. $\Delta\Psi_s$: surface potential. $\Delta\Psi_d$: dipole potential. U_m: transmembrane potential = membrane voltage. **(b)** Applied electrical potential Ψ versus transverse cell position x in membrane capacitor description.

is

$$U_m = \Psi_{ic} - \Psi_{ec} = \frac{Q_{s,ic}}{C_m} = -\frac{Q_{s,ec}}{C_m}. \tag{1}$$

The capacitance is given by

$$C_m = \frac{\varepsilon_r \varepsilon_0 A_m}{d_m}, \tag{2}$$

where ε_r is the relative permittivity of the membrane, $\varepsilon_0 = 8.85416 \times 10^{-12}$ $CV^{-1}m^{-1}$ is the permittivity of free space, A_m is the membrane surface area, and d_m is the membrane thickness. The specific capacitance $C_{m,sp}$, per surface area, is

$$C_{m,sp} = \frac{C_m}{A_m} = \frac{Q_{s,ic}/A_m}{U_m} = \frac{\sigma_{s,ic}}{U_m} = \frac{n_{s,ic} e}{U_m} = \frac{\varepsilon_r \varepsilon_0}{d_m}, \tag{3}$$

where $\sigma_{s,ic} = Q_{s,ic}/A_m$ is the intracellular surface charge density, $n_{s,ic} = \sigma_{s,ic}/e$, is the intracellular surface charge number density, and $e = 1.60217733 \times 10^{-19}$ C is the elementary electric charge.

Rearrangement of Eq. 3 gives

$$U_m = \sigma_{s,ic}\frac{d_m}{\varepsilon_r \varepsilon_0} = n_{s,ic}\frac{d_m e}{\varepsilon_r \varepsilon_0}. \tag{4}$$

The dependence of the membrane voltage on the intracellular membrane surface charge number density $n_{s,ic}$ is displayed in Fig. 2 (left side ordinate). There is used a membrane thickness of $d_m = 5$ nm [33] and a relative membrane permittivity of $\varepsilon_r = 11$ [33], giving $C_{m,sp} = 0.0195$ $CV^{-1}m^{-2}$.

The electrical field strength E_m inside the membrane is given by

$$E_m = \frac{U_m}{d_m} = n_{s,ic}\frac{e}{\varepsilon_r \varepsilon_0}. \tag{5}$$

In the intracellular and extracellular space, the electrical field strength is zero. In Fig. 2 the electrical field strength inside the membrane E_m versus the intracellular membrane surface charge number density $n_{s,ic}$ is displayed (right side ordinate).

The intracellular, $n_{s,ic}$, and extracellular, $n_{s,ec} = -n_{s,ic}$, membrane surface charge number densities are determined by the intracellular, $\Delta n_{v,ic}$, and extracellular, $\Delta n_{v,ec}$, excess volume charge number densities which are caused by cation and anion transport through the selective permeable membrane. They are given by

$$n_{s,ic} = \int \Delta n_{v,ic}(x)dx = \int \Delta n_{v,ic,0}\exp\left(-\frac{|x - x_{m,ic}|}{\ell_{Debye,ic}}\right)dx = \Delta n_{v,ic,0}\ell_{Debye,ic}, \tag{6a}$$

$$n_{s,ec} = -n_{s,ic} = \int \Delta n_{v,ec}(x)dx = \int \Delta n_{v,ec,0}\exp\left(-\frac{|x - x_{m,ec}|}{\ell_{Debye,ec}}\right)dx = \Delta n_{v,ec,0}\ell_{Debye,ec}. \tag{6b}$$

The integration occurs along the transverse coordinate x to the membrane surfaces at positions $x_{m,ic}$ (intracellular) and $x_{m,ec}$ (extracellular). The excess volume charge number densities at the membrane surfaces are $\Delta n_{v,ic,0}$ and $\Delta n_{v,ec,0}$. They decay exponentially with distance from the membrane surfaces $x_{m,ic}$ and $x_{m,ec}$ with the Debye

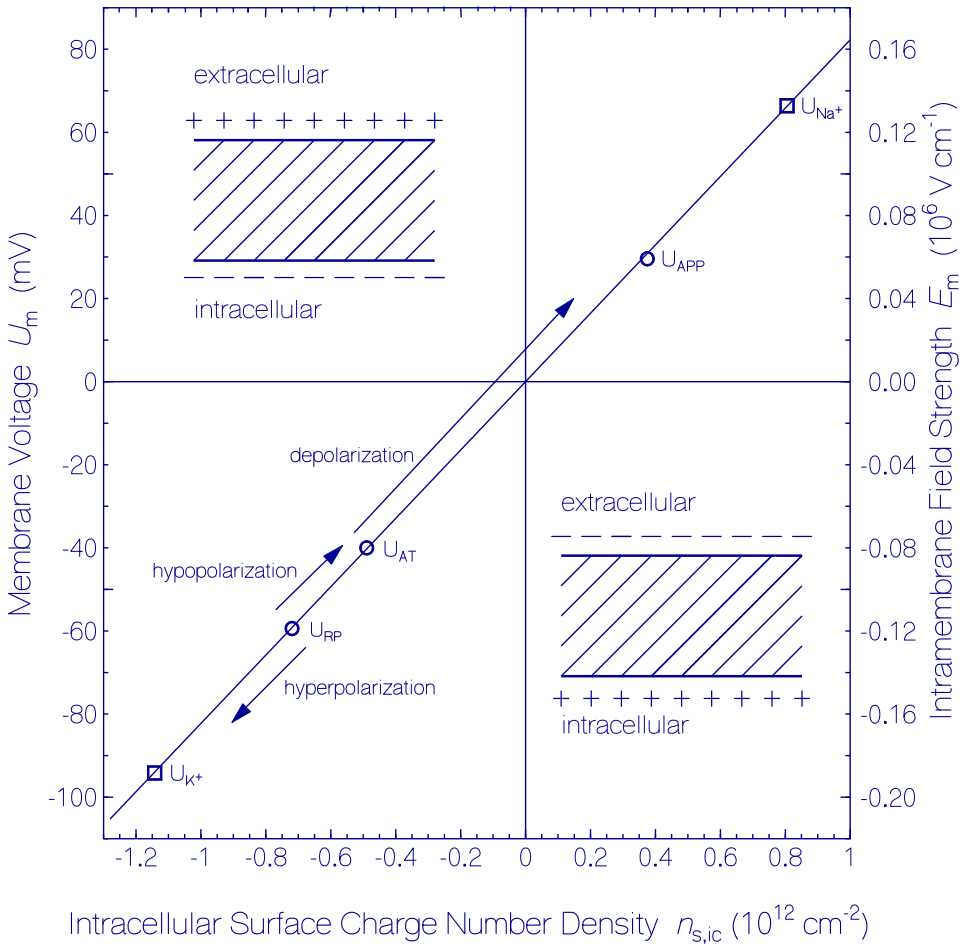

Fig. 2. Dependence of membrane voltage U_m (left side) and intramembrane field strength E_m (right side) on intracellular surface charge number density $n_{s,ic}$. The parameters used are relative permittivity $\varepsilon_r = 11$ and membrane thickness $d_m = 5$ nm. Indicated characteristic neuron membrane potentials are: U_{RP} = -60 mV: resting potential, U_{AT} = -40 mV: activation threshold potential, U_{APP} = 30 mV: activation peak potential, U_{K^+} = -94 mV: K^+ Nernst membrane equilibrium potential, U_{Na^+} = 67 mV: Na^+ Nernst membrane equilibrium potential. The inserted drawings show the charging situation of the membrane for $n_{s,ic} < 0$ (left side) and $n_{s,ic} > 0$ (right side).

lengths $\ell_{Debye,ic}$ and $\ell_{Debye,ec}$ which are given by [35,36]

$$\ell_{Debye,ic} = \left(\frac{\varepsilon_r \varepsilon_0 k_B T}{e^2 \sum_{i_{ic}} |n_{i_{ic}}| z_{i_{ic}}^2}\right)^{1/2}, \tag{7a}$$

$$\ell_{Debye,ec} = \left(\frac{\varepsilon_r \varepsilon_0 k_B T}{e^2 \sum_{i_{ec}} |n_{i_{ec}}| z_{i_{ec}}^2}\right)^{1/2}, \tag{7b}$$

where $k_B = 1.38054 \times 10^{-23}$ JK^{-1} is the Boltzmann constant, T is the temperature (in K), $n_{i_{ic}}$ is the number density of intracellular ions i_{ic} of valence $z_{i_{ic}}$, and $n_{i_{ec}}$ is the number density of extracellular ions i_{ec} of valence $z_{i_{ec}}$.

Rearranging of Eqs. 6a and 6b gives

$$\Delta n_{v,ic}(x) = \Delta n_{v,ic,0} \exp\left(-\frac{|x - x_{m,ic}|}{\ell_{Debye,ic}}\right) = \frac{n_{s,ic}}{\ell_{Debye,ic}} \exp\left(-\frac{|x - x_{m,ic}|}{\ell_{Debye,ic}}\right), \tag{8a}$$

$$\Delta n_{v,ec}(x) = \Delta n_{v,ec,0} \exp\left(-\frac{|x - x_{m,ec}|}{\ell_{Debye,ec}}\right) = \frac{n_{s,ec}}{\ell_{Debye,ec}} \exp\left(-\frac{|x - x_{m,ec}|}{\ell_{Debye,ec}}\right) = -\frac{n_{s,ic}}{\ell_{Debye,ec}} \exp\left(-\frac{|x - x_{m,ec}|}{\ell_{Debye,ec}}\right). \tag{8b}$$

In Fig. 3 the excess volume charge number density Δn_v versus the transverse cell position x is displayed. $x < x_{m,ic} = -5$ nm belongs to the intracellular space, and $x > x_{m,ec} = 0$ nm belongs to the extracellular space, The position inside the membrane is $x_{m,ic} < x < x_{m,ec}$. d_m is the cell membrane thickness. The parameters used in Fig. 3 belong to a membrane thickness $d_m = x_{m,ec} - x_{m,ic} = 5$ nm, a resting potential of U_{RP} = -60 mV where the intracellular surface charge number density is $n_{s,ic} = -7.3 \times 10^{11}$ cm^{-2} and $n_{s,ec} = 7.3 \times 10^{11}$ cm^{-2} (Fig. 2), and Debye lengths of $\ell_{Debye,ic} = \ell_{Debye,ec} = 1$ nm.

2.4.2. *Static membrane potential behavior*

The plasma (extracellular) concentration and cytoplasmic (intracellular) concentration of various ions (Na^+, K^+, Ca^{2+}, Mg^{2+}, Cl^-) is different, established by ATP-dependent ion pumps in the membrane [37]. The intracellular and extracellular neutrality is warranted by counterions. In ion-selective semipermeable membranes (cell membranes), ion transport through the semipermeable membrane towards concentration equilibration occurs by diffusion and it is counteracted by transmembrane electrical potential buildup.

The free enthalpy ΔG_{diff} of diffusion-controlled ion transport of a membrane selectively permeable only for ion of sort A is given by [19, 35,38]

$$\Delta G_{diff} = N_A k_B T \ln\left(\frac{c_{A_{ic}}}{c_{A_{ec}}}\right), \tag{9}$$

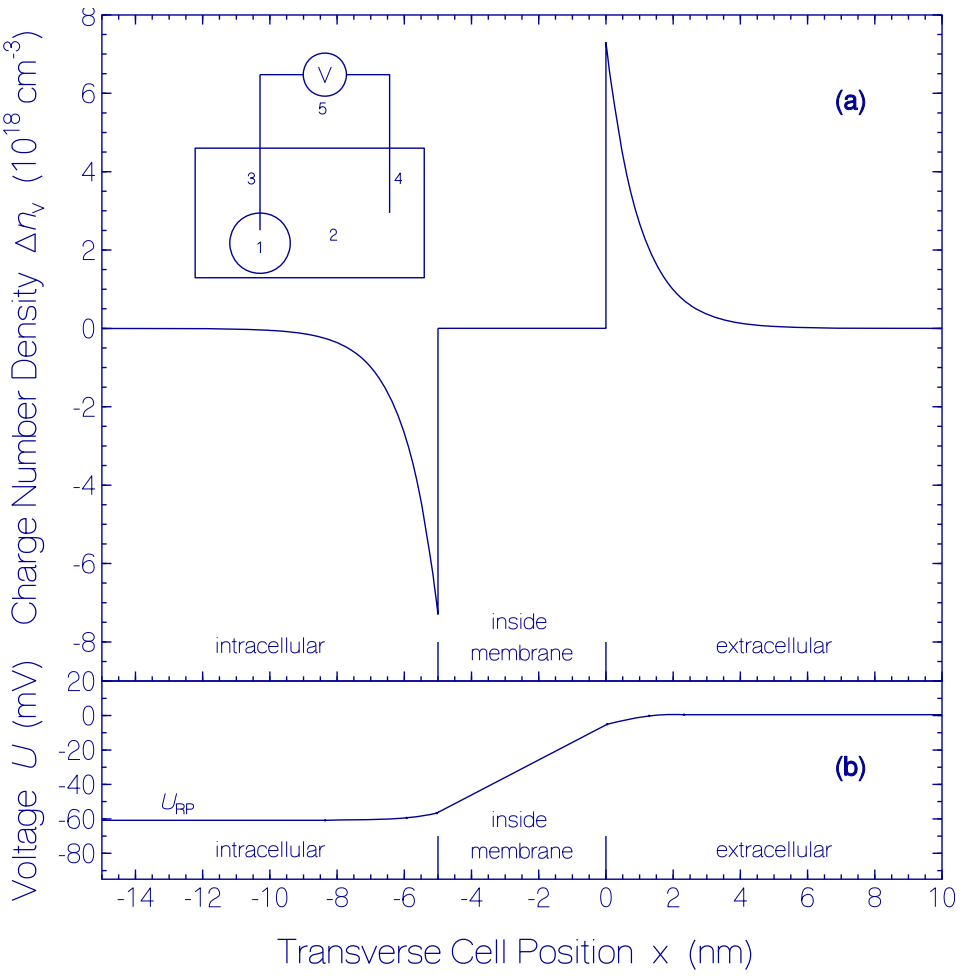

Fig. 3. **(a)** Excess charge number density Δn_v across transverse cell position at membrane resting potential of U_{RP} = -60 mV corresponding to intracellular surface charge number density of $n_{s,ic}$ = -7.3 × 10^{11} cm^{-2} (see Fig. 2). Debye lengths of $\ell_{Debye,ic} = \ell_{Debye,ec}$ = 1 nm are assumed. A membrane thickness of d_m = 5 nm is used. **(b)** Electrical potential versus transvers cell position for situation of (a). A schematic experimental arrangement for transmembrane membrane potential U_m measurement is included in (a). The abbreviations used there are: 1: cell, 2: bath, 3: glass microelectrode (recording electrode), 4: reference electrode, 5: microvoltmeter.

where N_A is the Avogadro constant, k_B is the Boltzmann constant, T is the temperature, $c_{A_{ic}}$ is the intracellular concentration of ion A, and $c_{A_{ec}}$ is the extracellular concentration of ion A.

The free enthalpy ΔG_{charge} of charge-controlled ion transport is given by [19]

$$\Delta G_{charge} = z_{ion} N_A e U_m, \tag{10}$$

where z_{ion} is the valence of the ion A (positive for cations and negative for anions).

The total free enthalpy is [19]

$$\Delta G_{total} = \Delta G_{diff} + \Delta G_{charge} = N_A k_B T \ln\left(\frac{c_{A_{ic}}}{c_{A_{ec}}}\right) + z_{ion} N_A e U_m. \tag{11}$$

Equilibration exists for $\Delta G_{total} = 0$ giving the Nernst equation (Eq. 12) for the membrane voltage (internal electrical potential – external electrical potential) [38]

$$U_m = -\frac{k_B T}{z_{ion} e} \ln\left(\frac{c_{A_{ic}}}{c_{A_{ec}}}\right). \tag{12}$$

Application of Eq. 12 to the typical intracellular and extracellular ion concentrations of Na^+, K^+, Ca^{2+}, Mg^{2+}, and Cl^- in mammalian cells listed in Table 1 at a temperature of T = 310 K (37°C) gives the membrane equilibrium voltages $U_m = U_{Nernst}$ included in Table 1 [27].

The real thermodynamic membrane potential caused by the presence of various monovalent and divalent ions of different intracellular and extracellular concentrations and different ion permeabilities through the membrane is given by the constant field equation given in [39].

For only monovalent ions the constant field equation given in [39] reduces to the Goldman-Hodgkin-Katz equation [25,40,41] which reads

$$U_m = \frac{k_B T}{e} \ln\left(\frac{\sum_i P_{ka,i} c_{ka,ec,i} + \sum_j P_{an,j} c_{an,ic,j}}{\sum_i P_{ka,i} c_{ka,ic,i} + \sum_j P_{an,j} c_{an,ec,j}}\right), \tag{13}$$

where $P_{ka,i}$ is the permeability coefficient (selectivity) of cation i through the membrane, $P_{an,j}$ is the permeability coefficient of anion j through the membrane, $c_{ka,ec,i}$ and $c_{ka,ic,i}$ are the extracellular and intracellular concentrations of cation i, and $c_{an,ec,j}$ and $c_{an,ic,j}$ are the extracellular and intracellular concentrations of anion j.

Considering only Na^+, K^+, and Cl^- Eq. 13 reduces to

$$U_m = \frac{k_B T}{e} \ln\left(\frac{P_{Na^+} c_{Na^+,ec} + P_{K^+} c_{K^+,ec} + P_{Cl^-} c_{Cl^-,ic}}{P_{Na^+} c_{Na^+,ic} + P_{K^+} c_{K^+,ic} + P_{Cl^-} c_{Cl^-,ec}}\right). \tag{14}$$

For a single ion species, the constant field equation given in [39], and the Goldman-Hodgkin-Katz equation of form Eq. 13 and Eq. 14 reduce to the Nernst equation Eq. 12.

2.5. Dynamic membrane potential characteristics

The membrane reacts to extracellular and intracellular changes with

membrane voltage changes [20,21]. The behavior is different for excitable cells and non-excitable cells. In excitable cells, if a stimulus rises the membrane voltage above a threshold value, then a nonlinear membrane voltage pulse formation occurs (spike formation, action potential generation); if the stimulus causes a membrane voltage change below the action potential threshold, then the membrane voltage responses linearly (graded potential formation). In non-excitable cells, the membrane voltage response is proportional to intracellular and extracellular reactions.

2.5.1. Membrane potential spiking of excitable cells (action potential)

In excitable cells an action potential is generated when a stimulus changes the membrane voltage from the resting potential, U_{RP}, up to a threshold value, the activation threshold potential, U_{AT} [25]. Then a membrane voltage pulse (action potential) is formed. In neurons, voltage rise above U_{AT} activates the integral membrane protein voltage-gated Na^+ ion channels causing Na^+ influx (membrane conductivity for Na^+) with membrane voltage increase to positive values (depolarization) on a sub-millisecond to millisecond timescale (strong rise of permeability coefficient P_{Na^+} for $U_m \geq U_{AT}$). The Na^+ influx comes to an end due to Na^+ inactivation (steep decrease of permeability coefficient P_{Na^+}) ending the membrane voltage rise (peak of action potential U_{APP}). The rising membrane voltage begins to activates the integral membrane protein voltage-gated K^+ ion channels causing a delayed K^+ efflux (membrane conductivity for K^+, strong rise of permeability coefficient P_{K^+}) leading to a membrane voltage decrease (repolarization) below the resting membrane voltage U_{RP} (hyperpolarization, see Figures 20-33 in [19]). If no further stimulus occurs, then the membrane voltage recovers to the resting membrane voltage by the action of an ATP-driven sodium and potassium-based ion pump (Na^+/K^+-ATPase). A further or ongoing stimulus causes the generation of another action potential. During the action potential development continued stimulation cannot influence the dynamics (refractory period). Neurons encode and transmit information via action potentials [42,43]. Action potentials are initiated in the axon and the dendrites [9, 42]. Dendrites integrate synaptic inputs [9,44] to trigger action potentials, and dendrites carry back-propagating action potentials to synapses [9,42,44–46]. In cardiac muscle cells, additionally voltage-gated Ca^{2+} channels are involved elongating the spike duration [47].

In Fig. 4a a typical membrane voltage pulse development (action potential) in a neuron is shown for a short pulse above-threshold stimulus (shorter than refractory period, solid curve) and for a longer pulse above-threshold stimulus (longer than refractory period, dashed curve). The applied stimuli are depicted in Fig. 4c (for details see [48]).

2.5.2. Membrane potential development of non-excitable cells (graded potential)

In the membranes of non-excitable cells, no or not sufficient voltage-

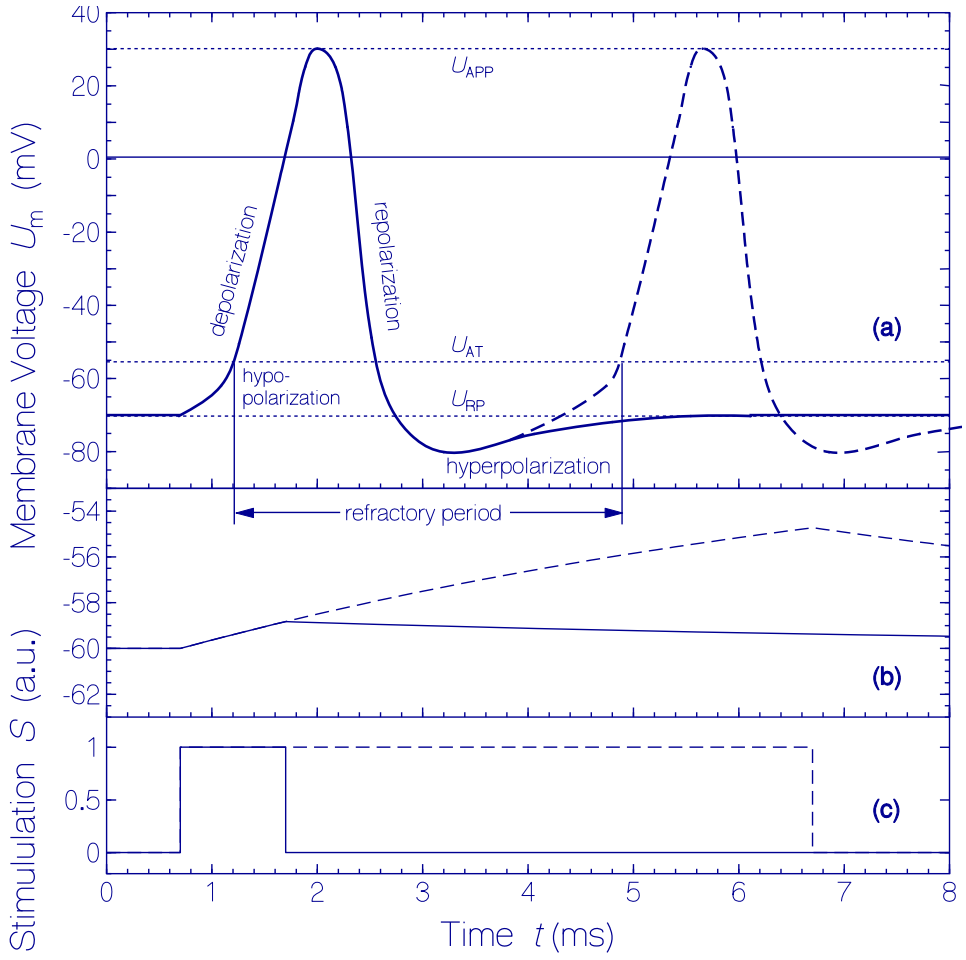

Fig. 4. Typical membrane voltage responses of an excitable cell **(a)** and of a non-excitable cell **(b)** to cellular stimulations **(c)**. The situation is shown for a short stimulation pulse (shorter than action potential duration, solid curves) and a longer stimulation pulse (longer than refractory period, dashed curves). U_{RP}: resting potential. U_{AT}: activation threshold potential. U_{APP}: activation peak potential. Hypopolarization = rise of membrane potential between resting potential and activation threshold potential. Depolarization = rise of action potential. Repolarization = decrease of action potential. Hyperpolarization = undershoot of action potential below the resting potential.

gated Na^+ and K^+ ion channels are present to cause nonlinear-response spike formation (cell firing). The membrane voltage response to stimuli is governed by the cell's compliment of ion channels and ion pumps. Ca^{2+} ion channels and Cl^- ion channels with slow dynamics may be involved hindering spiky behavior and causing linear voltage response. External action modulations have influence on the resting membrane potential modulation and vice versa [49–54]. The membrane potential is involved in regulation of cellular mechano-transduction [49], the cancer progression [50,51], regulation of cell proliferation and differentiation [53,54] and wound healing [55].

In Fig. 4b a typical membrane voltage development (graded potential, resting membrane potential modulation) in a non-excitable cell is shown for pulse stimuli depicted in Fig. 4c.

2.6. Classical membrane potential studies (classical electrophysical techniques)

The classical resting membrane potential measurement is carried out with a special voltmeter that is electrically connected to the interior of the investigated cell via a glass microelectrode and to the extracellular environment (bath) with an reference electrode [56] (see https://www.physiologyweb.com/lecture_notes/resting_membrane_potential/resting_membrane_potential.html). In Fig. 3a a schematic experimental setup for resting membrane potential measurement is included (works like whole-cell patch).

Electrophysical patch-clamp methods have been developed [57–59]. There the recording glass microelectrode is attached to the cell membrane (Giga-Ohm seal, inside the tip area are single membrane bound ion channels located, cell-attached method) or the microelectrode disrupts the membrane leading to different configurations (inside-out patch recording, outside-out patch recording, whole-cell recording) [60,61]. The patch-clamp methods are used to study i) the dynamics of membrane currents generated by ion passage through ion channels in the cell membrane (*voltage clamp method*, fixed voltages are applied and resulting currents are measured) [60–63] and ii) the dynamics of membrane potential development due to current inputs (*current clamp method*, fixed currents are applied and resulting voltages are measured like graded hyperpolarization potentials, graded hypopolarization potentials, or action potentials) [63–65].

Multi-electrode array (MEA) technologies have been developed for neuroscience and cardiology to stimulate action potential at subcellular, cellular and multi-cellular level [66,67]. Planar electrode devices record extracellular field potentials [67]. The recording of intracellular action potentials of multiple cells was achieved with nanopillars on the electrodes which penetrate the cell membrane and act as intracellular electrodes [68–70].

Bioimpedance spectroscopy (electrical impedance spectroscopy, dielectric spectroscopy applied to biology) is used to determine the specific membrane capacitance and the cytoplasm conductivity of individual cells or cell suspensions [71–73]. Thereby the dielectric permittivity and conductivity are derived from impedance measurements in an electrical field frequency range from dc to 10^5 Hz [74,75].

3. Electric field dependent effects acting in optical membrane voltage sensing

For sensing the electrical membrane potential of cells, voltage sensitive probes are located extracellular and/or intracellular, attached to the cell membranes, or entered into the cell membranes [29]. Genetic targeting and tagging of the voltage probes to specified cell membranes is applied [76].

The probes are voltage sensitive dyes [77–79], voltage sensitive nanoparticles [80], and genetically encoded voltage indicators (GEVIs) [81,82].

Voltage domain based GEVIs consist of four-segment (S1-S4) transmembrane voltage sensing domains (VSDs) based on phosphatases [83] or voltage-gated ion channels [84–86] coupled to fluorescent proteins. The membrane potential causes conformational changes on the transmembrane segment S4 which causes changes in the fluorescence behavior of the adjacent single fluorescent protein or fluorescent protein pair [15].

Microbial rhodopsin based GEVIs change their retinal protonation stage between neutral retinal Schiff base (RSB) and protonated retinal Schiff base (PRSB) depending on the membrane polarization state [87]. In stand-alone rhodopsin (opsin-only) based GEVIs the different absorption and emission spectra of RSB and PRSB are probed [87]. In rhodopsin-fluorescent protein based GEVIs fluorescent proteins are fused to the microbial rhodopsins. The changed fluorescent protein emission due the changes of the Förster-type resonant energy transfer (FRET) between fluorescent protein and rhodopsin is probed [88]. In chemigenetic microbial rhodopsin based GEVIs a protein tag domain binds a fluorescent synthetic dye to rhodopsin and the voltage dependent FRET behavior is monitored [89].

The voltage sensitivity of the probes may result from

i) electric field dependent polar particle effects,
ii) electric field dependent donor-acceptor effects,
iii) electric field dependent protonation-deprotonation of retinal in genetically encoded microbial rhodopsin light-driven proton pumps, and
iv) electric field dependent helix displacement in voltage sensitive domains of genetically encoded voltage-gated ion channels and phosphatases.

These various electric field dependent effects influencing the optical response are discussed in the following.

3.1. Electric field dependent polar particle effects

3.1.1. Redistribution of ionic dyes (slow dyes)

Ionic dyes, which are permeable through membrane pores, accumulate according to the membrane potential intracellular or extracellular following the Nernstian diffusion-controlled ion transport (for reviews see [29,77,90]). Cell hyperpolarization will cause increased intracellular cationic dye concentration, while cell depolarization will decrease intracellular cationic dye concentration. The opposite is true for anionic dyes. The dye diffusion through the cell membrane is a slow process. Therefore, the dye concentration change follows slowly any membrane potential change. One speaks of slow dye membrane potential probes (response time in the second range). The membrane potential is deduced from modified absorption and emission behavior of the dyes in the intracellular cytosolic space or extracellular plasma space. It occurs intracellular dye dimerization and aggregation in the case of increased intracellular concentration and dye binding to cytosolic macromolecules (change in absorption and emission spectra, fluorescence lifetimes, and quantum yields). The situation is schematically illustrated in Fig. 5 for intracellular cationic dye dimerization/ monomerization under intracellular negative/ positive charged conditions. As cationic dyes have been applied carbocyanines and rhodamines, as anionic dyes have been used oxonols [29,77,90].

3.1.2. Molecular Stark effect of electrochromic dyes (fast dyes)

Polar molecules with different electronic dipole moments in the ground-state and the excited-state cause different electric field dependent shifts of ground-state and excited-state potential energy levels (Stark effect like shifts [91–93]). It shows up in shifts of absorption and emission spectra caused by solvent polarity (solvatochromism) [94] and membrane polarization (electrochromism) [6,7,77,95,96]. One speaks of potentiometric dyes or electrochromic dyes and also 'charge-shift' probes because of different electronic charge distribution in the ground-state and excited-state [7]. The photoexcitation of electrochromic dyes causes excited-state intramolecular charge transfer

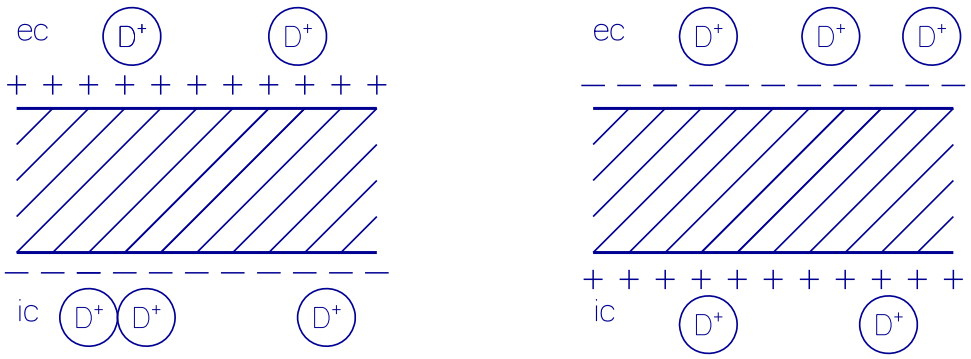

Fig. 5. Schematic illustration of membrane potential influence on cytosolic cationic slow dye dimerization. ec: extracellular, ic: intracellular, D^+: cationic dye.

(photoexcitation from ground-state to locally excited state (LE) followed by excited state charge redistribution to relaxed excited charge transfer state (CT)) [97–99].

The electric field dependent S_0 ground state level energy W_{S_0} is given by

$$W_{S_0} = W_{S_0}(0) - \vec{p}_{S_0}\vec{E}, \tag{15a}$$

and the electric field dependent S_1 exited state level energy W_{S_1} is given by

$$W_{S_1} = W_{S_1}(0) - \vec{p}_{S_1}\vec{E}. \tag{15b}$$

The absorption and emission determining energy level difference $\Delta W_{S_1-S_0}$ is

$$\Delta W_{S_1-S_0} = W_{S_1} - W_{S_0} = W_{S_1}(0) - W_{S_0}(0) - \left(\vec{p}_{S_1} - \vec{p}_{S_0}\right)\vec{E}. \tag{15c}$$

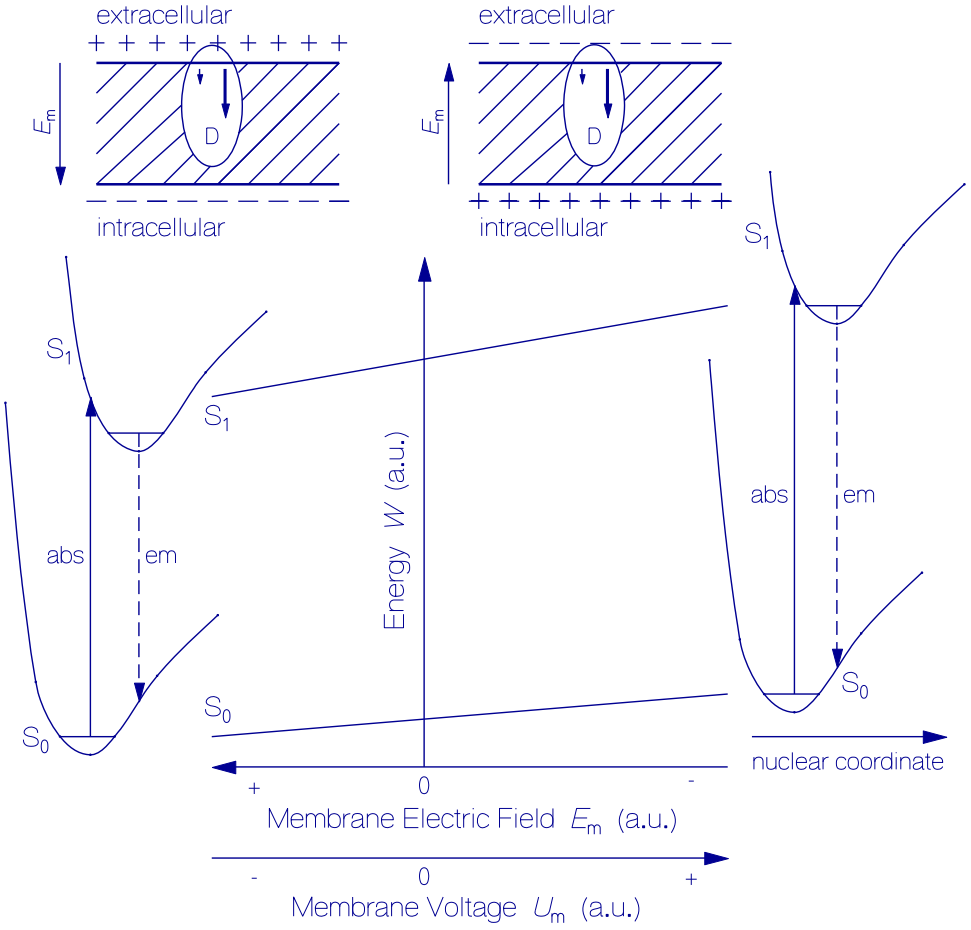

Fig. 6. Schematic dependence of S_0 and S_1 level energies W_{S_0} and W_{S_1} of an electrochromic dye, transverse fixed inside the membrane, on intramembrane electric field strength E_m or membrane voltage U_m. Dye potential energy curve diagrams versus nuclear coordinate are included for left-hand-side and right-hand-side E_m and U_m situations. S_0-S_1 absorption *abs* and S_1-S_0 fluorescence emission *em* are indicated. The electrochromic dye (D) positioned in the membrane is illustrated (for left side intracellular membrane side is negatively charged, for right side intracellular membrane side is positively charged). The short small arrow represents the ground-state dipole moment $\vec{p}_{S_0}$, the thick long arrow represents the excited-state dipole moment $\vec{p}_{S_1}$.The $W(E_m)$ diagram is shown for $\vec{E}_m \| \vec{p}_{S_0} \| \vec{p}_{S_1}$ for negative U_m, and $\vec{E}_m \uparrow\downarrow \left(\vec{p}_{S_0} \| \vec{p}_{S_1}\right)$ for positive U_m.

$\vec{p}_{S_0}$ is the electric dipole moment of the molecule in the S_0 ground-state, $\vec{p}_{S_1}$ is the electric dipole moment of the molecule in the S_1 excited-state, and $\vec{E}$ is the electrical field strength.

In Fig. 6 the electric field dependence of the S_0 and S_1 energy levels and the corresponding absorption and emission spectral shifts due to molecular Stark effect are illustrated (additional effects of real fast dyes as reorientation of the dye molecule as a whole inside the membrane are not included [29]). The dye is assumed to consist of hydrophilic end group to anchor at the extracellular membrane leaflet, a hydrophobic ionic chromophore inside the membrane and a lipophilic tail that stabilizes the dye inside the membrane and orients the dye transverse to the membrane [100].

3.1.3. *Quantum-confined Stark effect of semiconductor nanoparticles*

Semiconductor nanoparticles (having quantum well band structure) behave similar to organic dyes [101,102] (in dyes: absorption and emission between S_0 ground-state and S_1 first excited state, in semiconductor nanoparticles: absorption and emission between valence band and conduction band). The occurring quantum-confined Stark effect (QCSE) in semiconductor nanoparticle bioconjugates (nanoparticles covered with biocompatible ligands), especially nanorod bioconjugates, make them candidates for membrane voltage sensing [80,103–108]. Best performance was found for type-II ZnSe/CdS seeded nanorods [104] (nomenclature: type-I A/B nanoparticles: due to photoexcitation electron in conduction band and hole in valence band are located both either in A or B; type II nanoparticles: hole is located in A and electron is located in B or *vice versa*). In an electrical field, the conduction bands and valence bands are tilted along the direction of the electrical field, electrons and holes are more localized and their energy difference is field modified resulting in electric field dependent absorption/emission spectral shifts (QCSE). The operation principle is schematically illustrated in Fig. 7.

3.2. *Electrical field dependent donor-acceptor effects*

For energy-transfer donor-acceptor pairs, an applied electrical field may influence the efficiency of photoinduced Förster-type resonant energy transfer (FRET) [97,109] and thereby affect the efficiency of fluorescence emission. For electron-transfer donor-acceptor pairs, an applied electrical field may influence the efficiency of photoinduced electron-transfer (PeT) [97,110–112] and affect the efficiency of fluorescence emission. In the same way for proton-transfer, an applied electrical field may modify the efficiency of photoinduced excited-state intramolecular proton transfer (ESIPT) and show up in a change of fluorescence behavior [97,113]. In fluorescent proteins with protonated neutral form /deprotonated anionic form equilibration, electric field dependent ground-state proton transfer takes place which changes the absorption spectrum and the fluorescence emission [114].

3.2.1. *Electric field dependent Förster-type resonant energy transfer (FRET)*

The applied electrical field may spatially separate or bring together the energy-transfer donor-acceptor pair and thereby influence the fluorescence behavior of the donor-acceptor pair. In this case one speaks of electro-spatial Förster-type resonant energy transfer (esFRET) [79, 115–120]. For a polar (electrochromic) energy-transfer donor-acceptor pair the applied electrical field may worsen or improved the energetic

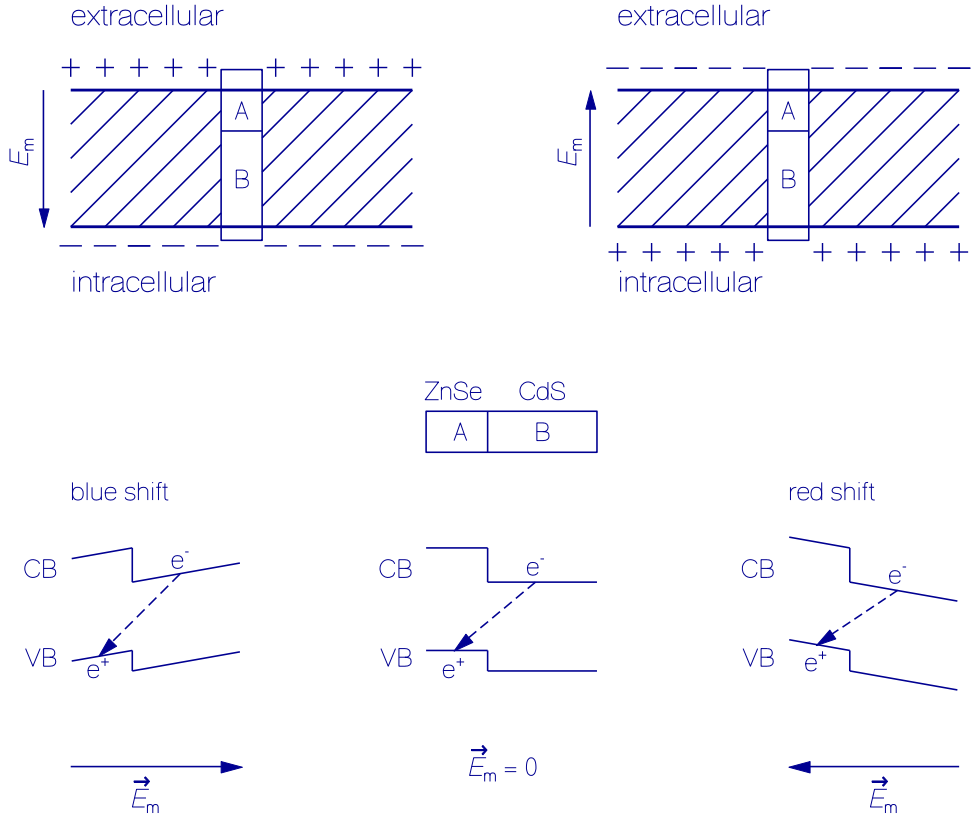

Fig. 7. Schematic illustration of ZnSe/CdS nanorod bioconjugate in cell membrane (A = ZnSe, bandgap energy 2.70 eV; B = CdS, bandgap energy = 2.42 eV). Top part: intracellular negative charged (left side) and positive charged (right side) cell membrane with embedded nanorod. Bottom part: Illustration of electric field strength dependent quantum well conduction band and valence band tilting (quantum-confined Stark effect QCSE) with accompanied absorption/emission spectral shifts [103,104]. Left side: situation for intracellular negative charged membrane (blue shift of absorption and emission compared to uncharged membrane). Middle part: situation for uncharged membrane. Right side: situation for intracellular positive charged membrane (red shift of absorption and emission compared to uncharged membrane). VB: valence band. CB: conduction band. e^+: hole (missing electron) in valence band. e^-: electron in conduction band. Dashed arrows: photon emission due to conduction band electron recovery to valence band hole.

resonance condition for donor to acceptor energy transfer and thereby influence the fluorescence behavior of the donor acceptor pair. For this situation one speaks of electrochromic Förster-type resonant energy transfer (ecFRET). An electric field dependent reorientation of an energy-transfer donor-acceptor pair changes the energy transfer efficiency and influences the fluorescence behavior. In this case one may speak of an electro-orientational Förster-type resonant energy transfer (eoFRET).

In Förster-type resonant energy transfer [109] the coulombic (dipolar) interaction between energy donor and energy acceptor transfers the excited donor electron in the LUMO-level (lowest unoccupied molecular orbital) down to its HOMO-level (highest occupied molecular orbital) and thereby transfers an electron from the HOMO-level of the acceptor to its LUMO-level. In the process the transition energy, ΔW, is conserved, i.e. $W_D(\mathrm{LUMO}) - W_D(\mathrm{HOMO}) = W_A(\mathrm{LUMO}) - W_A(\mathrm{HOMO})$, and only singlet-singlet transfer is allowed, i.e. $S_1(D)+S_0(A) \rightarrow S_0(D)+S_1(A)$ (no singlet–triplet spin-flip).

The rate of Förster-type energy transfer, k_{FT}, is given by [109,120,121]

$$k_{FT} = k_{F,0,D}\left(\frac{R_0}{R_d}\right)^6, \tag{16}$$

where $k_{F,0,D} = \tau_{F,0,D}^{-1}$ is the rate of S_1-S_0 relaxation of the donor in the absence of the acceptor ($\tau_{F,0,D}$ is the corresponding fluorescence lifetime), R_0 is the critical Förster distance where $k_{FT} = k_{F,0,D}$, and R_d is the (transition dipole center to center) distance between the donor and acceptor. R_0 is given by the relation [97,109,120,121]

$$R_0^6 = \frac{9\kappa^2}{128\pi^5 n^4}\int E_{F,0,D}(\lambda)\sigma_{a,A}(\lambda)\lambda^4 d\lambda, \tag{17}$$

where n is the average refractive index in the overlap region of acceptor absorption and donor emission, $E_{F,0,D}(\lambda)$ is the fluorescence quantum distribution of the donor in the absence of an acceptor (fluorescence quantum yield $\phi_{F,0,D} = \int E_{F,0,D}(\lambda)d\lambda$), and $\sigma_{a,A}(\lambda)$ is the absorption cross-section of the acceptor at wavelength λ. The orientation factor κ is determined by the orientation of the transition dipole moments of the interacting molecules D and A according to [109,120]

$$\kappa = \cos(\varphi_{DA}) - 3\cos(\varphi_D)\cos(\varphi_A), \tag{18}$$

where φ_D and φ_A are the angles of the donor and acceptor transition dipole moments to the connection line between donor and acceptor, and φ_{DA} is the mutual angle between the transition dipole moments. κ^2 may vary between 0 and 4. For a statistical isotropic orientation of the transition dipole moments it is $\overline{\kappa}^2 = 2/3$ [109].

3.2.1.1. Electro-spatial Förster-type resonant energy transfer (esFRET). An energy donor dye is anchored at the extracellular membrane side, and a movable anionic acceptor dye is inside the membrane (situation considered here, or *vice versa*). For intracellular negative charged membrane (negative membrane potential) the anionic acceptor dye moves to the donor dye and FRET from the donor dye to the acceptor dye occurs. For intracellular positive charged membrane (positive membrane potential) the anionic acceptor dye moves away from the donor dye to the intracellular membrane side and the donor- acceptor energy transfer diminishes. The method was applied in [97,115–117,122,123] for studying membrane potentials. It is illustrated in Fig. 8.

3.2.1.2. Electrochromic Förster-type resonant energy transfer (ecFRET). An energy donor molecule is anchored at the extracellular membrane side, and an electrochromic acceptor molecule is fixed inside the membrane near the extracellular side (similar situation for intracellular membrane positioning). The electrochromic molecule inside the

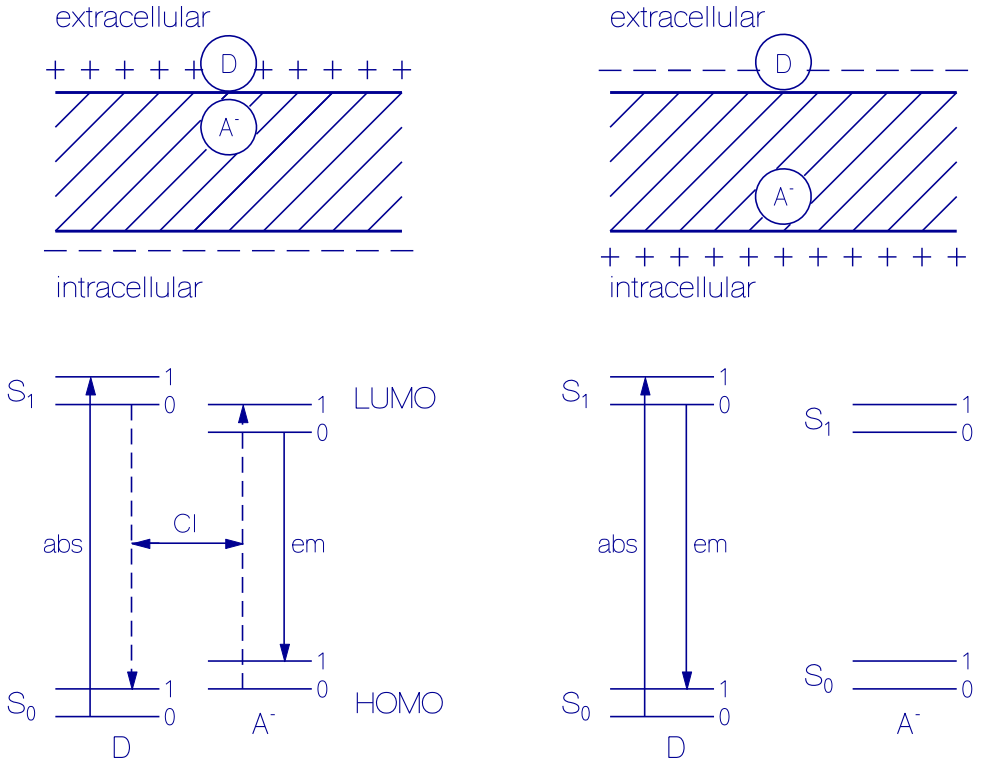

Fig. 8. Illustration of electric field dependent approaching/distancing of Förster-type resonant energy transfer molecules (electro-spatial FRET, esFRET). Top part: donor (D) and acceptor (A^-) molecule positioning for intracellular negative (left) and positive charged (right) membrane. Bottom part: S_0 and S_1 energy level system for donor molecule D and acceptor anion A^-. Left side, nearby positioning of D and A^- with strong Förster-type energy transfer. Right side, separate positioning of D and A^- with negligible Förster-type energy transfer. 0 and 1 indicate vibrational levels. abs: S_0-S_1 light absorption. em: S_1-S_0 fluorescence emission. CI: Coulombic interaction. HOMO: highest occupied molecular orbital. LUMO: lowest unoccupied molecular orbital.

membrane shifts its S_0 and S_1 energy levels with the intramembrane electrical field caused by the membrane potential thereby changing the efficiency of resonant Förster-type energy transfer and accompanying fluorescence behavior. This behavior is illustrated in Fig. 9.

Small donor-acceptor dye molecule based ecFRET membrane voltage probing has not been reported thus far, but it is applied in genetically encoded archaerhodopsin-fluorescent protein membrane voltage sensors in a somewhat different way (see below Section 4.6.2.) [124].

3.2.1.3. Electro-orientational Förster-type resonant energy transfer (eoFRET). The rate of Förster-type energy transfer depends on the orientation of the transition dipoles of the interacting donor and acceptor molecules (see Eqs. 16-18). This dependence was applied to explain the functioning of a voltage-sensitive fluorescent protein (VSFP1) consisting of a voltage sensitive domain of a potassium channel and a pair of fluorescent proteins, CFP and YFP [125,126] (see section 4.3.5).

3.2.2. Electric field dependent photoinduced electron transfer (PeT)

In photoinduced electron transfer (PeT), after photoexcitation an electron passes from an electron donor molecule D to an electron acceptor molecule A [127–129]. After the photoinduced electron transfer, the donor-acceptor pair recovers to the original ground-state situation by charge recombination (REC) [121,130]. One distinguishes between oxidative photoinduced electron transfer and reductive photoinduced electron transfer [97,121]. In the case of oxidative photoinduced electron transfer, the photoexcited electron in the donor S_1 state ($LUMO_D$) is transferred to the energetically lower lying acceptor S_1 state ($LUMO_A$) [97,121] (oxidation of photoexcited unit). In the case of reductive photoinduced electron transfer, the acceptor molecule is photoexcited and the empty place in the acceptor S_0 state ($HOMO_A$) is filled by electron transfer from the energetically higher lying donor S_0 state ($HOMO_D$) [97,121] (reduction of photoexcited unit). The situations of photoinduced oxidative electron transfer (PeT_o) and photoinduced reductive electron transfer (PeT_r) are illustrated in Fig. 10a.

The mechanism of photoinduced electron transfer is described theoretically by the Marcus theory [110–112,129,131–135]. In a classical description the rate of electron transfer k_{PeT} is given by the Arrhenius-type Eyring equation [136–138]

$$k_{PeT} = \kappa \frac{k_B T}{h} \exp\left(-\frac{E_a}{k_B T}\right), \tag{19}$$

where κ is the so-called electronic transmission factor (κ ≈ 1 for adiabatic electron transfer, κ << 1 for diabatic electron transfer), k_B is the Boltzmann constant, T is the temperature (in K), h is the Planck constant, and E_a is the activation energy of barrier crossing between electron donor and electron acceptor. The term k_BT/h is the attempt frequency $\nu_{attempt}$ of barrier crossing ($h\nu_{attempt} = k_BT$, see [19] page 476). The situation is illustrated in Fig. 10b for different donor and acceptor energy level positions.

In a quantum mechanical perturbation theoretical description the rate of photoinduced electron transfer is obtained applying Fermi's golden rule [135,139]

$$k_{PeT} = \frac{2\pi}{\hbar} V_R^2 FC, \tag{20}$$

where $\hbar = h/(2\pi)$ is the reduced Planck constant, V_R^2 is the donor-acceptor coupling constant (square of wavefunction overlap integral, V_R, of donor and acceptor state at donor-acceptor edge-to edge distance R, V_R^2 decreases exponentially with distance R), and FC is the Franck-Condon weighted density of states (equations for V_R and FC are found

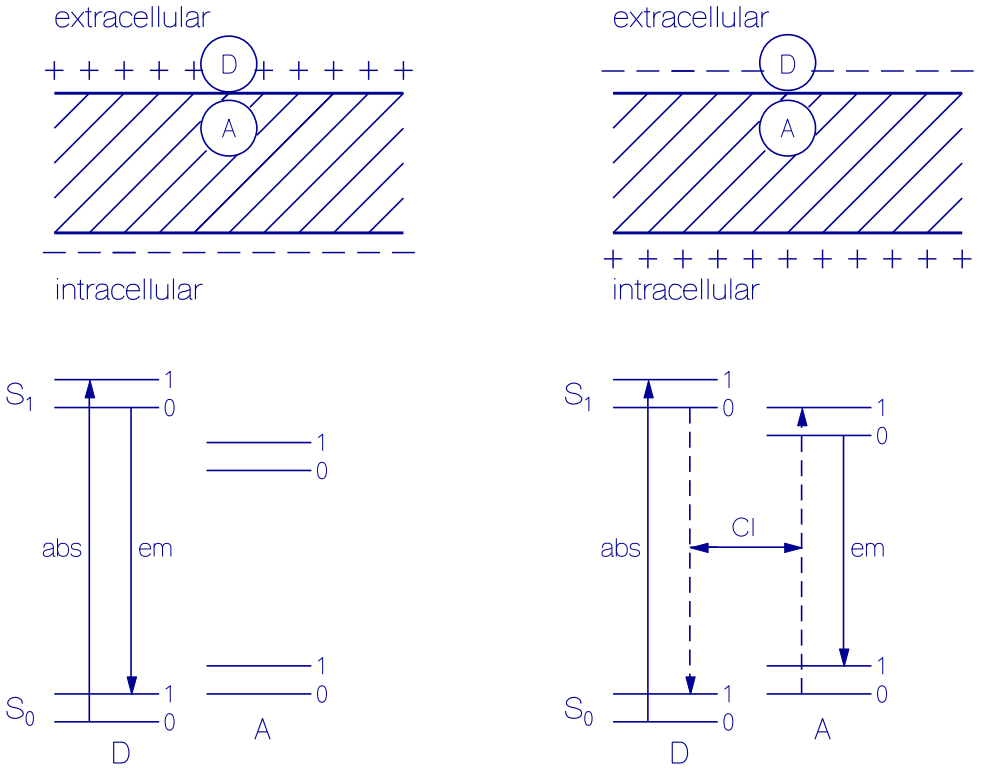

Fig. 9. Illustration of electric field dependent energy level shifting for enabling Förster-type resonant energy transfer between donor and acceptor molecule (electrochromic FRET, ecFRET). Top part: donor (D) and acceptor (A) molecule positioned at the same place for intracellular negative (left) and positive charged (right) membrane. Bottom part: for left side S_0 and S_1 energy level system for donor molecule D and acceptor molecule are not in optimum energetic position for efficient FRET ($\lambda_{em,max}(D) \neq \lambda_{abs,max}(A)$); for right side S_0 and S_1 energy level system for donor molecule D and acceptor molecule A are in optimum energetic position for efficient FRET ($\lambda_{em,max}(D) = \lambda_{abs,max}(A)$). 0 and 1 indicate vibrational levels. abs: S_0-S_1 light absorption. em: S_1-S_0 fluorescence emission. CI: Coulombic interaction.

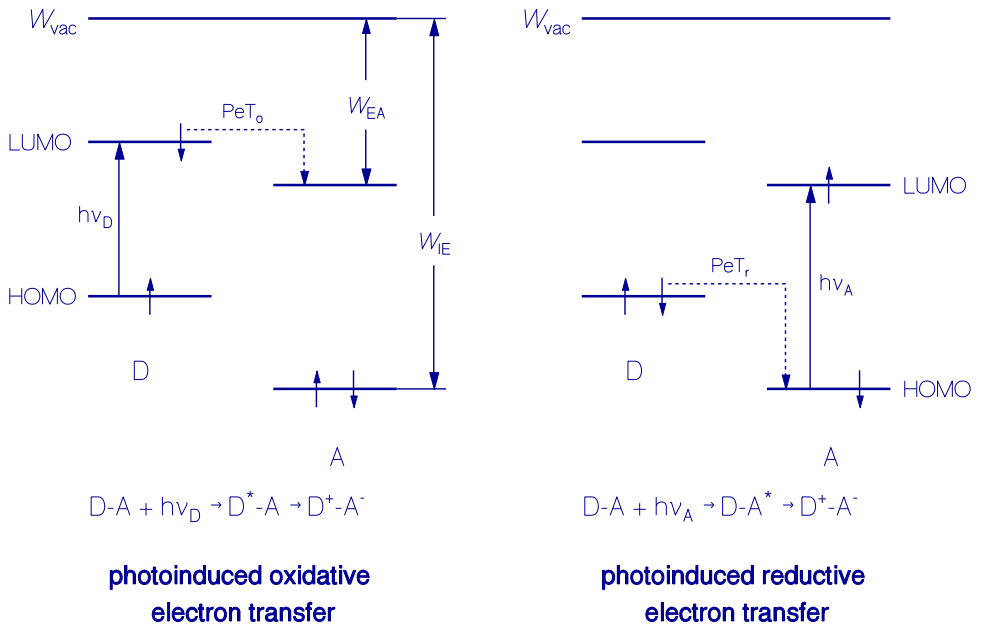

Fig. 10a. Illustration of photoinduced oxidative electron transfer (PeT_o) and photoinduced reductive electron transfer (PeT_r). W_{vac}: vacuum level (beginning of vacuum continuum). W_{IE}: ionization energy. W_{EA}: electron affinity. HOMO: highest occupied molecular orbital. LUMO: lowest unoccupied molecular orbital. $h\nu_D$: donor excitation photon energy. $h\nu_A$: acceptor excitation photon energy.

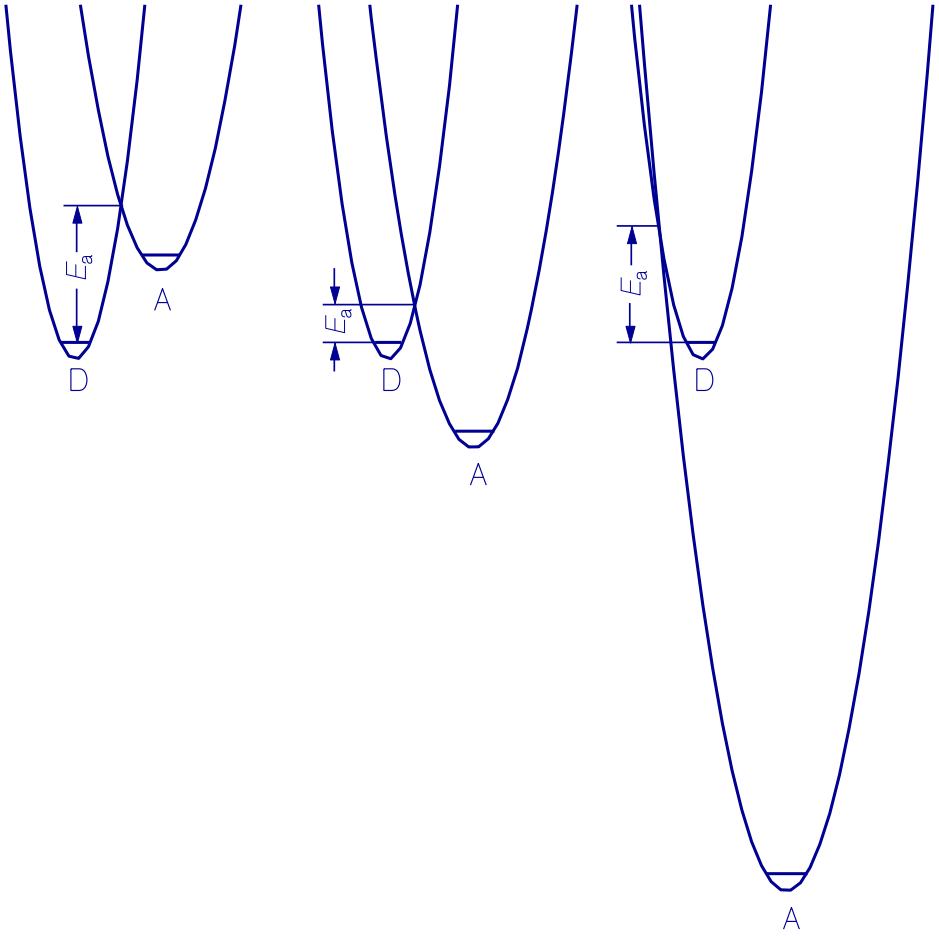

Fig. 10b. Potential energy curves (parabola) for electron donor D and electron acceptor A situations. Left part: donor energy level is below acceptor energy level $W_D < W_A$, normal Marcus-region. Middle part: donor energy level is above acceptor energy level $W_D > W_A$, normal Marcus-region. Right part: donor energy level is considerably above acceptor energy level $W_D >> W_A$, inverse Marcus-region. E_a: activation energy.

in the literature [110–112,127,130–135,139]) .

The electron transfer requires an overlap of the donor electronic wavefunction with the acceptor electronic wavefunction needing direct contact of the donor and acceptor molecules [121,135]. In through-bond electron transfer the molecular bridge (wire) between donor and acceptor mediates the electron transport [139,140]. Stiff conjugated double bond wires allow long-distance electron transport from donor to acceptor [141,142].

In electric field dependent photoinduced-electron transfer membrane voltage sensors, a hydrophilic dye D (absorbing and emitting in the visible spectral range) is coupled via a lipophilic conjugated double bond bridge (wire) to an aniline molecule A (absorbing and emitting in the near ultraviolet spectral range). The hydrophilic fluorophore is located at the extracellular membrane leaflet, the lipophilic conjugated molecular wire and the aniline molecule are located in the membrane interior and experience intramembrane electrical field strength. The ionization energy (ionization potential) $W_{IE,D}$ of the dye D is smaller than the ionization energy $W_{IE,A}$ of aniline A (for example W_{IE}(rhodamine 6G at aqueous solution surface) = 5.6 eV [143], W_{IE}(aniline in gas phase) = 7.72 eV [144]). This energy leveling is the situation of oxidative photoinduced electron transfer (photoexcited dye is electron donor, unexcited aniline is electron acceptor). The electric field dependent photoinduced electron-transfer situation applied in membrane voltage determination is illustrated in Fig. 10c. The intramembrane electric field shifts the aniline LUMO energy level and thereby changes the activation energy E_a (Eq. 19) or the Franck-Condon weighted density of states factor *FC* (Eq. 20) of electron transfer efficiency (variation of rate constant for electron transfer versus standard free energy of the reaction according to the Marcus theory [110–112,129,132–134,139,145]). The intramembrane field in the intracellular negative charged membrane shifts the S_1 energy level of the aniline molecule in the membrane below the S_1 energy level of the fluorophore at the extracellular membrane side allowing through-bond oxidative photoinduced electron transfer [97,139–141] from the fluorophore (acting as electron donor) to the first excited state of aniline (acting as electron acceptor).

Various photoinduced electron transfer (PeT) based membrane voltage indicators consisting of fluorophore-wire-aniline donor-acceptor pairs have been applied [118,119,122,142,144–149]. Voltage controls fluorescence quenching by shifting the aniline energy level relative to the fluorophore, gating electron transfer along the molecular wire. Genetically targetable PeT-based membrane voltage indicators with a membrane-anchored enzyme have been developed [150–152].

3.2.3. *Electric field dependent photoinduced excited-state intramolecular proton transfer (ESIPT)*

Probes with proton donor – proton acceptor capability may process proton transfer in applied electric fields [113]. Ground-state proton-transfer (GSPT) and excited-state proton transfer (ESPT) require a H-bond coupling of a proton donor moiety and a proton acceptor moiety. A proper applied electric field may modify the donor-acceptor equilibration conditions leading to proton transfer reactions. Excited-state intramolecular proton transfer (ESIPT) was used for fast ratiometric measurement of cellular transmembrane potential [153]. For this purpose, tautomeric dyes based on the 3-hydroxychromone fluorophore were applied [153].

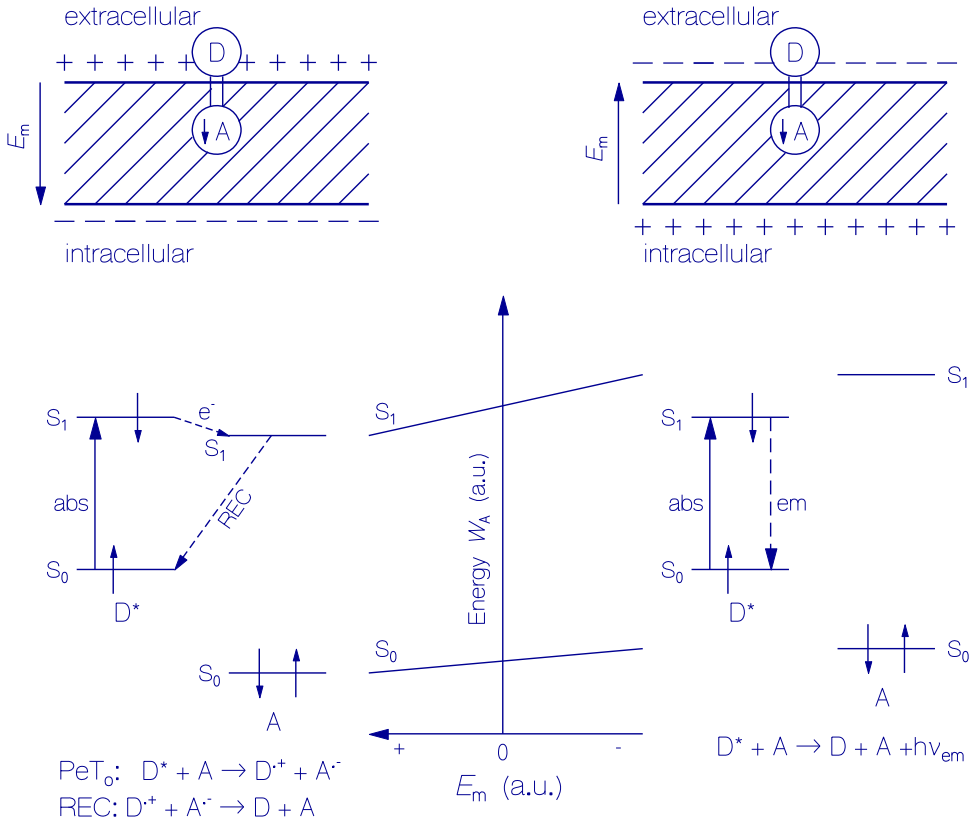

Fig. 10c. Illustration of electric field dependent photoinduced oxidative electron transfer (PeT$_o$). Top part: donor (D) and acceptor (A) molecule connected with conjugated double bond bridge (wire) positioned at the same place for intracellular negative (left) and positive charged (right) membrane. Direction of membrane electrical field $\vec{E}_m$ and direction of acceptor dipole moment (↓) are indicated. Bottom part, left side: LUMO (S_1 energy level) of donor molecule is above LUMO (S_1 energy level) of acceptor molecule allowing excited-state electron transfer from donor to acceptor after photoexcitation of the donor thereby hindering donor fluorescence emission (smaller activation energy E_a of barrier crossing, larger Franck-Condon weighted density of states factor *FC* for electron transfer). Bottom part, right side: LUMO of acceptor molecule is above LUMO of donor molecule hindering excited-state electron transfer from the donor to acceptor after photoexcitation of the donor thereby allowing donor fluorescence emission (larger E_a of Eq. 19, smaller *FC* of Eq. 20). REC: charge recombination.

The applied electric field modifies the excited state tautomeric equilibrium between the initial normal excited state (N*) and a tautomeric state (T*) produced via an excited state intramolecular proton transfer (ESIPT) [29,153]. Compared to the intracellular negative charged membrane, the N* fluorescence emission decreases and the T* fluorescence emission increases for the intracellular positive charged membrane. The operation principle is displayed in Fig. 11.

3.2.4. *Electric field dependent ground-state intramolecular proton transfer*

Some fluorescent proteins like wild-type green fluorescent protein from *Aequorea victoria* (wt AvGFP) exist in an equilibrium mixture of neutral form and anionic form (e.g. neutral form of wt AvGFP with tyrosine 66 (Y 66) has its absorption maximum at 397 nm, anionic form of wt AvGFP with tyrosinate 66 (Y^- 66) has its absorption maximum at 475 nm [114,154,155]). The equilibrium of protonated neutral form and deprotonated anionic form seems to be influenced by the electrical field strength allowing membrane potential reporting [156,157].

3.3. *Electric field dependent ground-state intermolecular proton transfer in genetically encoded transmembrane opsins*

Electric field dependent ground-state intermolecular proton transfer occurs between an adjacent acidic amino acid (Asp, D) and the retinal Schiff base chromophore in rhodopsin-based genetically encoded voltage indicators (GEVIs) [124,158–160]. One distinguishes between negative-going rhodopsin-based GEVIs (H^+ pathway between retinal and extracellular membrane face is blocked by mutation) [87,158] and positive going rhodopsin-based GEVIs (H^+ pathway between retinal and intracellular membrane face is blocked by mutation) [161].

3.3.1. *Negative-going rhodopsin-based GEVIs*

The outward H^+ pumping mechanism of the used light-driven outward proton pumping microbial rhodopsins is blocked at the retinal to extracellular membrane pathway by mutating the proton accepting aspartic acid adjacent to retinal by an asparagine (D-N) mutation [87,158]. The intracellular membrane to retinal pathway is unchanged, the proton donating aspartic acid is present there.

Under intracellular negative conditions protonated retinal Schiff base (PRSB) gives up its proton to the negative charged intracellular membrane leaflet (e^-) via an aspartic acid between PRSB and intracellular membrane leaflet according to

$$PRSB + Asp^- + e^- \rightarrow RSB + AspH + e^- \rightarrow RSB + Asp^- + H^+e^-. \quad (21)$$

Under intracellular positive conditions neutral retinal Schiff base (RSB) takes up a proton from the positive charged intracellular membrane leaflet (H^+) via the same aspartic acid according to

$$RSB + Asp^- + H^+ \rightarrow RSB + AspH \rightarrow PRSB + Asp^-. \quad (22)$$

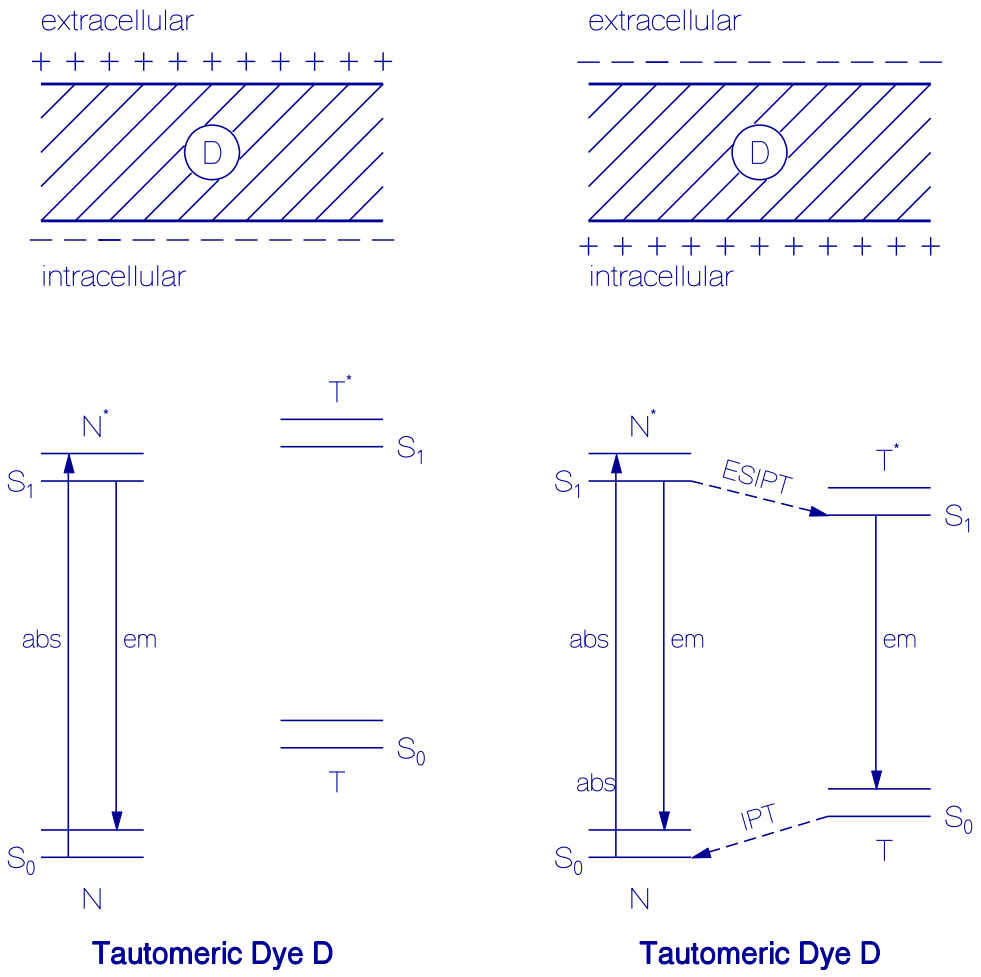

Fig. 11. Schematic illustration of electric field dependent photoinduced excited state intramolecular proton transfer (ESIPT). Top part: intracellular negative charged membrane (left) and intracellular positive charged membrane (right) with intramembrane containing tautomeric dye D. Bottom part: Under intracellular negative conditions (left side), ESIPT is energetically hindered causing dominant fluorescence emission from photoexcited normal N dye. Under intracellular positive conditions (right side), ESIPT from N* to T* is energetically possible and fluorescence emission from T* to T takes place. In the ground state occurs T → N ground-state intramolecular proton transfer from the tautomeric T state to the original normal N state.

Therefore, under intracellular negative conditions, the retinal Schiff base chromophore is dominantly present in neutral form (RSB) which absorbs in the near ultraviolet to violet spectral region [162,163]. While under intracellular positive conditions, the retinal Schiff base is dominantly present in protonated form (PRSB) absorbing in the green to yellow spectral region [162,163]. The operation principle is displayed in the top part of Fig. 12, and the bottom part of Fig. 12 shows the absorption and emission behavior of PRSB and RSB.

3.3.2. *Positive-going rhodopsin-based GEVIs*

The outward H^+ pumping mechanism of the used light-driven outward proton pumping microbial rhodopsin is blocked at the intracellular membrane to retinal pathway by mutating the proton donating aspartic acid between intracellular membrane leaflet and retinal by an asparagine (D-N) mutation [161]. At the retinal to extracellular membrane pathway the proton accepting aspartic acid near the retinal is retained and the proton releasing glutamic acid is changed to valine (E-V mutation) [161].

Under intracellular negative conditions RSB takes up a proton from the positive extracellular membrane leaflet (H^+) via the blocked proton release and the aspartic acid proton acceptor near the retinal according to

$$RSB + Asp^- + Val + H^+ \rightarrow RSB + AspH + Val \rightarrow PRSB + Asp^- + Val. \quad (23)$$

Under intracellular positive conditions PRSB gives up its proton to the negative charged extracellular membrane leaflet (e^-) via the same aspartic acid proton acceptor and the (E-V) mutant according to

$$PRSB + Asp^- + Val + e^- \rightarrow RSB + AspH + Val + e^- \rightarrow RSB + Asp^- + Val + H^+e^-. \quad (24)$$

Therefore, under intracellular negative conditions the retinal Schiff base chromophore is dominantly present in protonated form (PRSB) which absorbs in the green to yellow spectral region [162,163]. While under intracellular positive conditions, the retinal Schiff base is dominantly present in neutral form (RSB) absorbing in the near ultraviolet to violet spectral region [162,163]. The operation principle is displayed in the middle part of Fig. 12. The bottom part of Fig. 12 shows S_0- S_1 energy level schemes of RSB and PRSB.

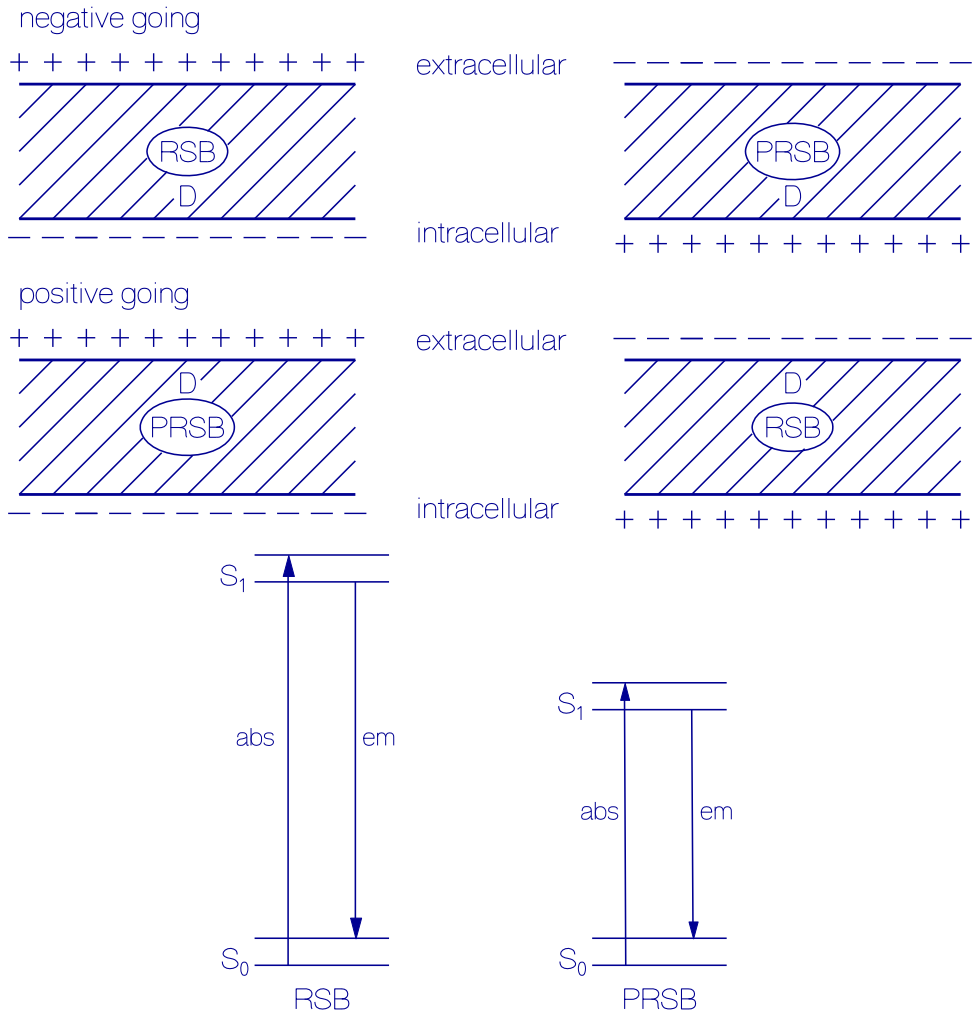

Fig. 12. Schematic illustration of electric field dependent intermolecular ground-state proton transfer (GSPT) in rhodopsin-based genetically encoded voltage indicators (GEVIs). Top part: negative going rhodopsin-based GEVI (H^+ transfer to extracellular membrane leaflet is blocked, and H^+ transfer to intracellular membrane via Asp (D) is open). Left side: intracellular negative charged membrane containing transmembrane rhodopsin with dominant neutral retinal Schiff base chromophore (RSB). Right side: intracellular positive charged membrane containing transmembrane rhodopsin with dominant protonated retinal Schiff base chromophore (PRSB). Middle part: positive going rhodopsin-based GEVI (H^+ transfer to intracellular membrane leaflet is blocked, and H^+ transfer to extracellular membrane leaflet via Asp (D) is open). Left side: intracellular negative charged membrane containing dominantly protonated retinal Schiff base chromophore (PRSB). Right side: intracellular positive charged membrane containing dominantly neutral retinal Schiff base chromophore (RSB). Bottom part: S_0-S_1 energy level schemes of RSB and PRSB. RSB has its first absorption band in the violet/near UV spectral range, and PRSB has its first absorption band in the green/yellow spectral range.

3.4. Electric field induced helix displacement in voltage sensitive domains of genetically encoded voltage-gated ion channels and phosphatases

Voltage-gated ion channels are transmembrane proteins that form an ion channeling pore and contain a four-segment voltage sensitive domain VSD (S1-S4) which regulates the ion transport through the pore according to the membrane potential [164–166]. Positively charged residues in the S4 segment respond to changes in the membrane potential, causing S4 to move inward (down state) at negative voltages and outward (up state) at positive voltages [167,168]. In genetically encoded voltage-gated ion channels, fluorescent proteins are fused to the ion channels, whose fluorescence is influenced by the membrane potential causing ion channel restructuring [84–86,169].

Voltage sensitive phosphatases (VSPs) (also named voltage sensor-containing phosphatases) have a four-segment transmembrane domain VSD (S1-S4) like the voltage-gated ion channels which regulate the phosphatase activity in a voltage sensitive manner [170–174]. They are a protein family found in many species including humans, mice, zebrafish, frogs, and sea squirt [175]. Strong membrane voltage sensitivity was found in the tunicate (sea squirt) *Ciona intestinalis* phosphatase (Ci-VSP) [176] and in the chicken *Gallus gallus* phosphatase (Gg-VSP) [177]. Their four-segment voltage sensitive domains (VSDs) were genetically engineered and fused with fluorescent proteins to fabricate genetically encoded voltage indicators (GEVIs) (based on Ci-VSP: [178–181], based on Gg-VSP: [167,177,182–187]). The membrane voltage induced S4 segment displacement modifies the fluorescent protein emission behavior.

Three types of phosphatase-based GEVIs have been developed:

i) A single fluorescent protein (FP) [176,177,188] or a circular-permuted fluorescent protein (cpFP) [189–191] was fused to the VSD. Voltage-induced conformational changes in the VSD influence the FP chromophore environment leading to changes in the FP fluorescence behavior [154,189–195].
ii) Two adjacent VSDs, each with a special fused FP (S4-FP linker length optimized), form an FP dimer under depolarization conditions and thereby reduce their fluorescence emission [196–202].
iii) A pair of matched FPs was fused to the VSD, and the FRET efficiency depended on the membrane potential [167,179,181].

They are described in the following.

3.4.1. Single fluorescent protein or circular-permuted fluorescent protein fused to voltage sensitive domain

The environmental charge situation may influence the chromophore spectroscopic behavior in the fluorescent protein (FP) [203]. The N and C termini of circular-permuted fluorescent proteins (cpFPs) are in close proximity to the chromophore in the fluorescent protein making their fluorescence behavior sensitive to the environmental situation. In voltage-gated phosphatase-based GEVIs with fused FPs or cpFPs, a membrane potential induced S4 position shift affects the FP chromophore environment. It deforms the β-barrel structure of the FP acting on the chromophore which may change its absorption and fluorescence behavior [194,195,204,205]. A schematic illustration of a possible modulation of the fluorescent protein emission due to VSD response to the actual membrane potential is shown in Fig. 13a [177].

3.4.2. Single FP fused to voltage sensitive domain of VSP-based mosaic GEVI

The mutated pH sensitive fluorescent protein (pHluorin) [154,203] with negative charge on the outside of the β-can, superecliptic pHluorin A227D (short names SE(A227D) or SEP), tends to dimerize in positive charged environment. SE(A227D) was fused to the VSD of VSP-based mosaic GEVIs at the intracellular membrane site. Under depolarization conditions, the SEPs of adjacent VSDs alter their relative orientation and position tending to dimerize and thereby reduce their fluorescence emission [196–201]. Also, when dTomato FP was fused to S4 of the VSD of VSP-based mosaic GEVIs with proper linker length, the FPs of adjacent VSDs tend to dimerize under depolarization conditions [202]. The operation principle is schematically illustrated in Fig. 13b for the case of SE(A227D) fused to VSD.

3.4.3. Matched fluorescent protein pair fused to voltage sensitive domain

In a VSP-based GEVI with a matched FP pair fused to the VSD, an electric field induced S4 segment displacement causes a spatial approaching or separation of the FP pair with accompanying increased or reduced FRET. In the case of using a bioluminescent protein (BP) and fluorescent protein (FP) pair, the electric field induced S4 segment displacement changes the distance between BP and FP, thereby modifying the bioluminescent resonant energy transfer (BRET) from BP to FP and modifies the fluorescence emission of FP [206,207]. The situation is illustrated in Fig. 13c.

4. Voltage sensitive probes

Voltage sensitive probes respond to the membrane potential. They may be standalone systems reacting to the membrane potential with their intrinsic absorption/emission behavior. They may be coupled systems consisting of a membrane voltage sensing entity and an accompanied signaling/reporting (absorbing/fluorescing/quenching) entity. The probes may be arbitrarily intercalated/attached to arbitrary membranes/membrane localizations, or they may be specifically targeted to specific membrane types/localized membrane positions.

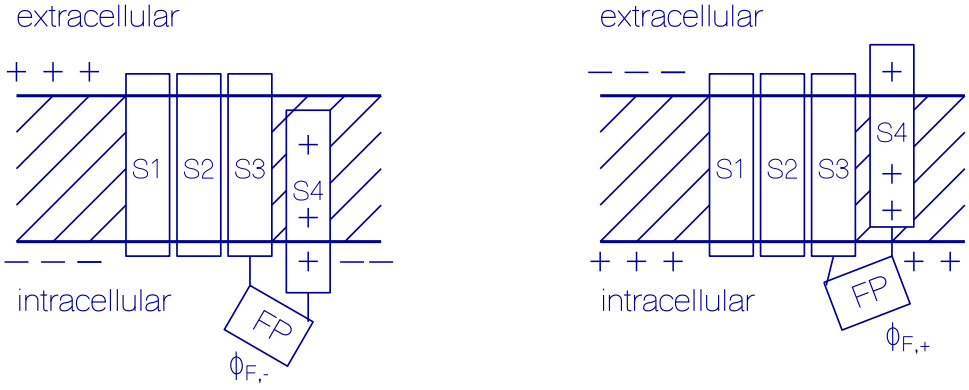

Fig. 13a. Schematic illustration of mechanism of voltage-sensing with VSD and fused FP or cpFP. Left side: intracellular negative charged membrane with down positioned voltage sensitive segment S4. The corresponding fluorescence quantum yield of fused fluorescent protein is $\phi_{F,-}$. Right side: intracellular positive charged membrane with up positioned voltage sensitive domain S4. The fluorescence quantum yield of the fused fluorescent protein is changed to $\phi_{F,+}$.

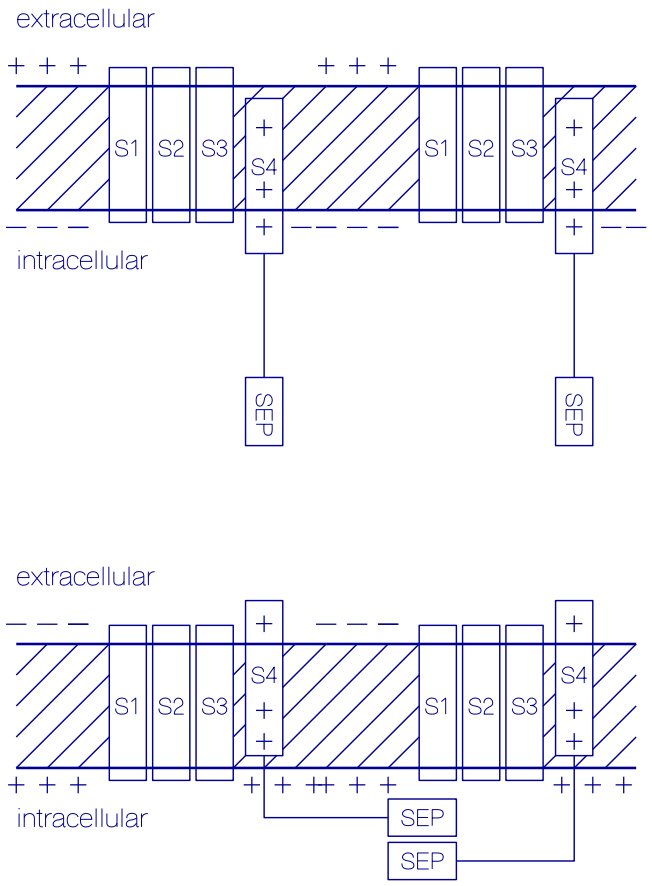

Fig. 13b. Schematic illustration of mechanism of voltage-sensing VSP-based mosaic GEVIs with fused superecliptic pHluorin A227D [196–201]. Top part: intracellular negative charged membrane. The SEP fluorescent proteins fused to segments S4 of the VSDs are present in fluorescent monomeric form. Bottom part: intracellular positive charged membrane. Neighboring SEP fluorescent proteins fused to segments S4 of the VSDs arrange to non-fluorescent dimers.

Voltage sensitive dye probes are described in [7,29,77,79,100,119,186,208–214]. Genetically encoded voltage indicators (GEVIs) based on voltage sensitive domains (VSDs) of voltage-gated ion channels or voltage sensitive phosphatases (VSPs) are reviewed in [13,15,83,197,215–218]. GEVIs based on microbial rhodopsin probes are reviewed in [13,82,197,214–218].

Important parameters of the applied voltage probes are their photostability, biological toxicity, targeting, solubility, mobility, temporal response, absorption cross-section, fluorescence quantum yield, signal to noise ratio, electric field dependence of signal strength. The fractional signal change of probes with membrane voltage change is expressed as $\Delta S/S$, where ΔS is the signal change due to 100 mV of voltage rise (typical action potential height) and S is the signal before voltage change (typically the signal at the resting potential). The signal in most cases is fluorescence (then S = F), sometimes absorption (S = A), a ratio (S = R), or another parameter. Data characterizing the probes are reported in the original papers. The temporal response time, $\tau_{resp} \approx \Delta t_{AP,probe} - \Delta t_{AP,true}$, where $\Delta t_{AP,probe}$ is the temporal halfwidth of the measured probe signal of the action potential and $\Delta t_{AP,true}$ is the true temporal halfwidth of the action potential, gives the broadening of the measured action potential compared to the true action potential. If the response time is longer than the time separation between sequent action potentials, then individual action potentials cannot be resolved.

4.1. *Voltage-sensitive dye probes*

Voltage sensitive dyes are reviewed in [29,77,118,119,186,211,219,220]. They may be grouped in intramembrane positioned electrochromic voltage-sensitive organic dyes with fast response to voltage changes [7,29,100,119,211,221,222], membrane permeable ionic organic dyes responding to membrane surface charge (slow dyes) [29,77,90], intramembrane mobile dyes in combination with extracellular membrane fixed fluorescent dyes for Förster-type resonant energy transfer [79,115–117], and electron donor acceptor pairs for membrane voltage probing via photoinduced electron transfer [142,148].

4.1.1. *Membrane permeable dyes (Nernstian dyes, slow dyes)*

Some ionic dyes are membrane permeable and their preferential intracellular membrane localization or extracellular membrane localization follows the Nernstian concentation distribution law. Under intracellular negative charged membrane conditions (negative membrane potential) cationic membrane permeable dyes concentrate intracellular and accumulate at the intracellular membrane leaflet, while anionic membrane permeable dyes concentrate extracellular and accumulate at the extracellular membrane leaflet. Under intracellular positive charged membrane conditions the situation is *vice versa*. The Nernstian equilibrium formation takes some time (greater than seconds). Therefore, one speaks of slow (responding) dyes.

Various Nernstian dyes have been applied belonging to cationic cyanines, cationic rhodamines, and anionic oxonols [29,77,90,223–227]. Permeability-controllable potentiometric fluorescent carbazole dyes were developed bearing different lengths of alkyl chains [228]. As examples, the structural formulae of the cyanine dye 3,3'-dipropylthiadicarbocyanine iodide $DiSC_3(5)$, the rhodamine dye tetramethylrhodamine methyl ester (TMRM), and the oxonol dye bis-(3-propyl-5-oxoisoxazol-4-yl) pentamethine oxonol (Oxonol VI) are shown in Fig. 14 [29,90].

4.1.2. *Membrane mobile dyes*

Membrane mobile lipophilic dyes are applied in membrane voltage sensitive probes based on electro-spatial Förster-type resonant energy transfer (esFRET, see Fig. 8). At the extracellular membrane site, a fluorescent dye is located acting as energy donor, and in the membrane a charged mobile dye is used as energy acceptor. The mobile dye chooses its position according to the membrane potential either at the extracellular membrane leaflet near the energy donor causing efficient FRET or at the intracellular membrane leaflet hindering FRET.

As lipophilic intramembrane mobile molecules were used alkylthiobarbiturate-polymethine oxonol dyes $DiSBAC_n(m)$ (n = 4, 6, 10 number of methylene and methyl units in alkyl groups, m = 3, 5 number of methine units in polymethine), [79,115,116,230], and butyl barbiturate-trimethine oxonol $DiBAC_4(3)$ [186] with sub-millisecond response time. Especially the non-fluorescent hydrophobic anion dipicrylamine (DPA^-) [117,223,231–234] with 100 µs response time is applied. The structural formulae of $DisBAC_4(5)$ and DPA^- are shown in Fig. 15.

4.1.3. *Intramembrane positioned electrochromic voltage-sensitive dyes (fast dyes)*

A group of dyes applicable for voltage sensing are polar dyes with rather different electric dipole moments in the S_0 ground-state and the first S_1 excited-state. They are called voltage-sensitive dyes, potentiometric dyes, or electrochromic dyes. They are also labeled as 'charge-shift' probes [7,95,96]. Amphiphilic dyes are used with the lipophilic part binding to the cell membrane interior and the hydrophilic part being at the cell membrane exterior [237]. Either membrane potential dependent absorption spectra changes or fluorescence spectra changes are measured. *Potentiometric Probes* develops and supplies voltage-sensitive dyes for academic and pharmaceutical industry researchers (https://potentiometricprobes.com). Voltage sensitive dyes have been specialized to brain and cardiac electrophysiology [10,209,238–243].

As an example, in Fig. 16 the structural formulae are shown of the

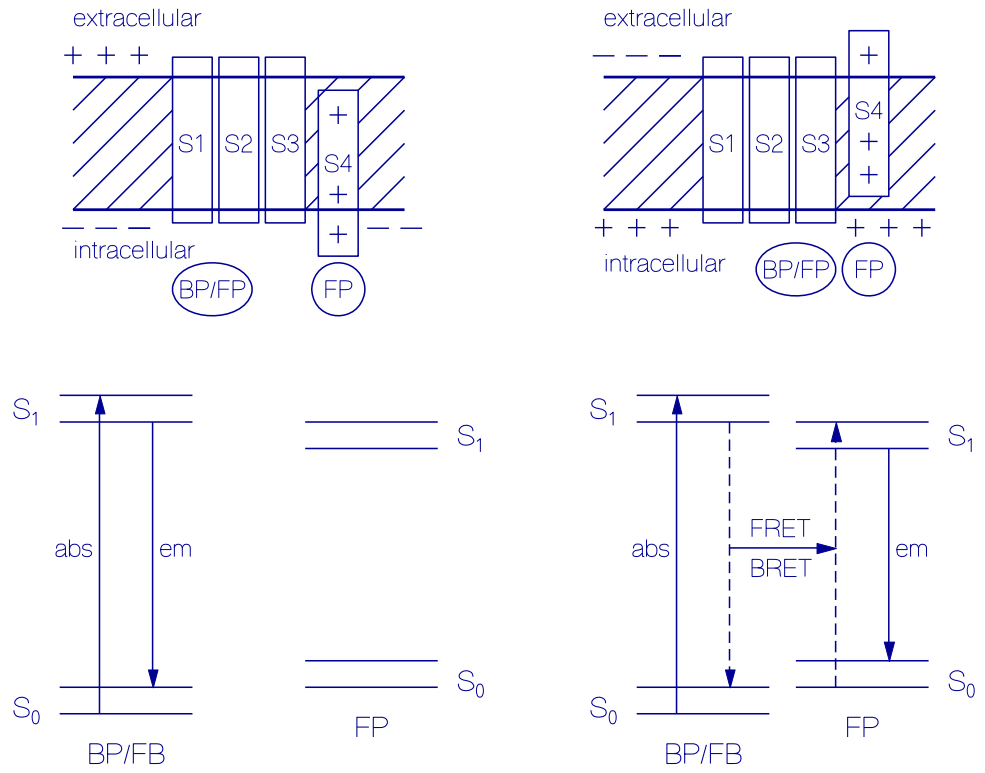

Fig. 13c. Schematic illustration of voltage-sensing with a fused matched fluorescent protein pair or matched bioluminescent protein/fluorescent protein pair evolving distance dependent FRET or BRET due to VSD restructuring. Top part, left side: intracellular negative charged membrane with down positioned voltage sensitive segment S4. Top part, right side: intracellular positive charged membrane with up positioned voltage sensitive segment S4. Bottom part, left side: Under intracellular negative conditions, FP/FP pair or BP/FP pair is separated with negligible FRET/BRET efficiency. Bottom part, right side: Under intracellular positive conditions, FP/FP pair or BP/FP pair is near together with strong FRET/BRET efficiency and acceptor FP fluorescence emission.

popular naphthyl styryl pyridinium dye 4-(2-(6-(dibutylamino)-2-naphthalenyl) ethenyl)-1-(3-sulfopropyl)-pyridinium, known as di-4-ANEPPS, in the ground-state and first excited state [96]. Like di-4-ANEPPS, the potentiometric dye di-8-ANEPPS is used [244,245] (there dibutylamino group is replaced by dioctylamino group). This dye is more lipophilic due to the longer methylene chain and therefore is better retained in the leaflet of the cell plasma membrane [244–246]. Di-4-ANEPPS is more prone to internalization (accumulation in the cell interior).

4.1.4. Electron donor acceptor pairs for membrane voltage probing via photoinduced electron transfer (PeT)

Organic dye PeT based membrane voltage probes are molecule complexes (dyads) consisting of a hydrophilic fluorophore, a lipophilic conjugated double-bond bridge (wire) and an aniline moiety. The applied fluorophores include rhodamines [151,222,247–249], fluoresceins [142,148,150,152,250,251], carbofluoresceins [147], indocyanine green [226,227] and carborhodoamines [252]. As an example, the chemical structure of a fluorescein-bridge-aniline complex named VoltageFluor dye VF2.1(OMe).H [148] is shown in Fig. 17. The fluorescein fluorophore acts as electron donor and aniline as electron acceptor in the photoinduced electron transfer (see Section 3.2.2). For VF2.1(OMe).H the response time is $\tau_{resp} < 150$ µs and the fractional fluorescence change is $\Delta F/F = 48$ % [148].

4.2. Voltage sensitive semiconductor nanoparticle probes

Semiconductor quantum dots (QDs, spherical) and quantum rods (QRs, cylindrical shaped) behave like organic dyes [101]. They generally have a semiconductor core, a semiconductor shell, and a biocompatible coating for intramembrane localization or extramembrane localization [102,253]. Examples are CdSe/ZnS and CdS/ZnSe QDs and QRs.

In intramembrane application the quantum-confined Stark effect is exploited (see Section 3.1.3). Small shifts in absorption spectra and emission spectra, or emission lifetime changes are measured [80, 104–106].

Extramembrane localized fluorescent nanoparticles were used with intramembrane mobile dipicrylamine anion (DPA^-) in FRET-based membrane voltage probing [254]. Membrane-anchored upconversion nanoparticles (UCNPs) together with intramembrane DPA^- were applied as FRET based near-infrared voltage sensors in real-time imaging of neuronal activities in mice and zebrafish [116]. Polystyrene beads loaded with dyes spectrally suitable for FRET interaction with DPA were used for optical probing of local membrane potentials [234].

CdSe/ZnS quantum dot-peptide-fullerene bioconjugates were developed and applied for *in vitro* and *in vivo* visualization of cellular membrane potential based on electric field influenced photoinduced oxidative electron transfer between quantum dot and fullerene [255, 256]. The quantum dot was anchored at the extracellular membrane and a peptide with an attached C_{60} fullerene was in the membrane inside. Under intracellular negative charged conditions the photoinduced electron transfer was reduced (higher activation energy, Eq. 19; smaller Franck-Condon weighted density of states factor, Eq. 20) and the quantum dot fluorescence efficiency increased. Under intracellular positive charged conditions the efficiency of the photoinduced electron transfer was increased (smaller activation energy, larger Franck-Condon weighted density of states factor) and the quantum dot fluorescence was reduced.

4.3. Fluorescent proteins for membrane voltage probing

Fluorescent proteins (FPs) are widely used tools for cellular imaging [257]. They are the fluorescent signal reporters in connection with

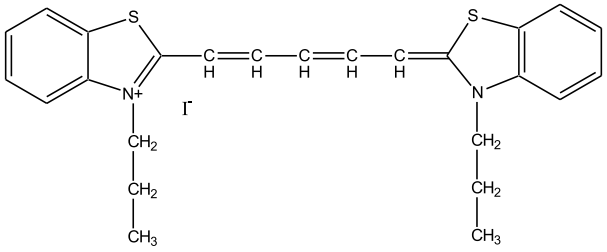

$DiSC_3(5)$

3,3'-dipropylthiadicarbocyanine iodide ($\lambda_{a,max}$ = 651 nm, $\lambda_{F,max}$ = 675 nm in methanol [229])

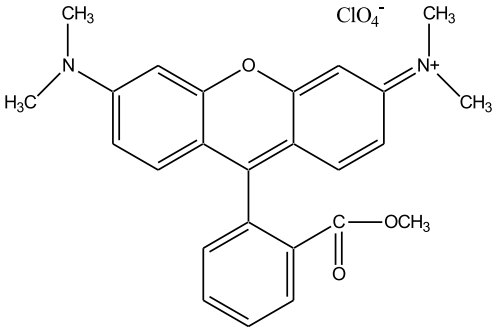

TMRM

Tetramethylrhodamine methyl ester ($\lambda_{a,max}$ = 549 nm, $\lambda_{F,max}$ = 573 nm in methanol [229])

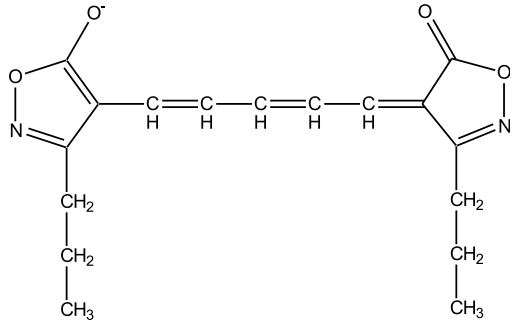

Oxonol VI

Bis-(3-propyl-5- oxoisoxazol-4-yl) pentamethine oxonol ($\lambda_{a,max}$ = 599 nm, $\lambda_{F,max}$ = 634 nm in mehanol [229])

Fig. 14. Structural formulae of the amphiphilic membrane permeable dyes 3,3'-dipropylthiadicarbocyanine iodide $DiSC_3(5)$ [90], tetramethylrhodamine methyl ester (TMRM) [76], and bis-(3-propyl-5-oxoisoxazol-4-yl) pentamethine oxonol (Oxonol VI) [90]. Nomenclature for $DiSC_3(5)$: Sub-index 3 counts the methylene and methyl units in the alkyl groups. In parentheses (5) counts the number of methine units of the polymethine chain. Listed parameters are taken from [229].

membrane voltage sensitive probes. The signal reporter mechanisms are either Förster-type resonant energy transfer (FRET) [13,15,81,82,215,217,258–260], environmental influence of chromophore fluorescence situation [13,115,156,157,206–215], or change of fluorescent protein monomerization/dimerization situation [196,197,199–202].

All FPs are capable of FRET if an appropriate resonant energy transfer donor or acceptor is adjacent to the FP.

In cpFPs the N and C termini are in close proximity to the chromophore of the fluorescent protein influencing the chromophore fluorescence behavior due to the environmental membrane negative/positive charge situation [189–191,193]. Electric field dependent chromophore influence may also occur in normal FPs [176–178]. pH sensitive mutants of green fluorescent protein (named pHluorin) change their excitation wavelength dependent fluorescence emission in a pH dependent manner [261]. The mutation may lead to ratiometric pHluorins (bimodal fluorescence behavior) or ecliptic pHluorins (fluorescence diminishes at low pH). The superecliptic pHluorin A227D mutant tends to dimerize under membrane depolarization conditions with accompanying fluorescence reduction [196–201]. Also, the basic orange fluorescent protein, dTomato, derived from *Discosma* sp. shows an electric field dependent

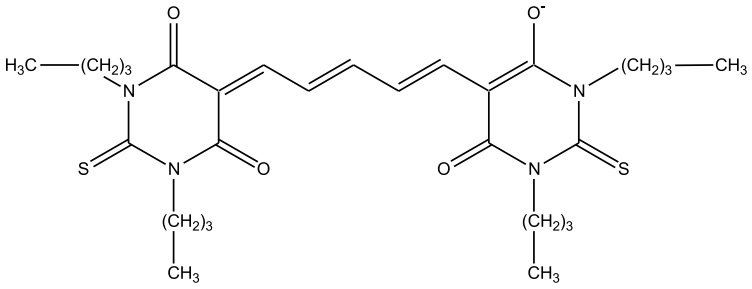

DiSBAC$_4$(5)

Bis-(1,3-dibutyl-2-thiobarbiturate)-pentamethine oxonol ($\lambda_{a,max}$ = 638 nm, $\lambda_{F,max}$ = 663 nm, in ethanol [116])

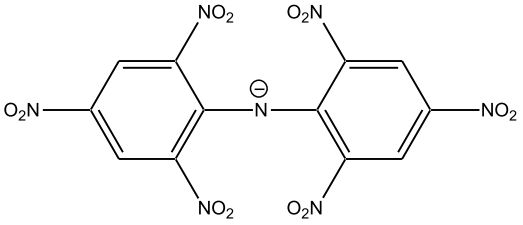

DPA$^-$

Dipicrylamine anion ($\lambda_{a,max}$(ethanol) = 412 nm [195], $\lambda_{a,max}$(acetonitrile) = 420 nm [235])

Fig. 15. Structural formulae of lipophilic anionic dye bis-(1,3-dibutyl-2-thiobarbiturate)-pentamethine oxonol (DiSBAC$_4$(5)) [116] and dipicrylamine anion (DPA$^-$) [236]. For DiSBAC$_4$(5): sub-index 4 counts the methylene and methyl units in the alkyl groups, (5) counts the number of methine units of the polymethine chain. Listed parameters are taken from [116,195,235].

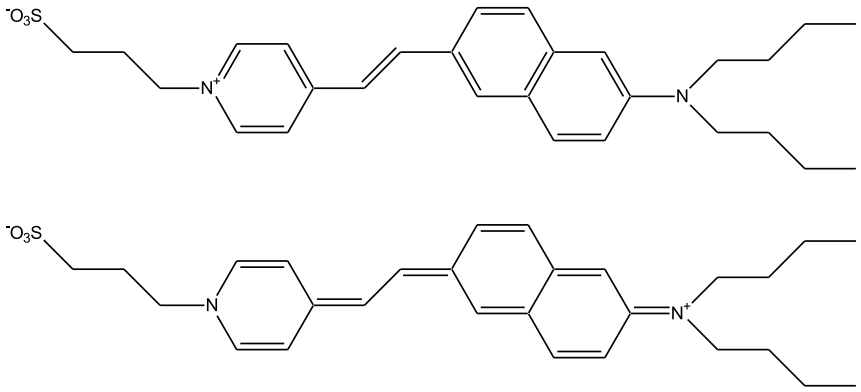

di-4-ANEPPS in ground-state

di-4-ANEPPS in first excited-state

Fig. 16. Di-4-ANEPPS in ground-state (top part) and first excited-state (bottom part). Structural formulae are taken from [96]. ($\lambda_{a,max}$ = 500 nm, $\lambda_{F,max}$ = 725 nm, in ethanol, from Potentiometric Probes). The sulfopropyl group is located at the extracellular membrane leaflet, the naphthyl-styryl pyridinium chromophore is located in the membrane interior adjacent to the membrane leaflet, the dibutyl group is aligned parallel to the intramembrane lipid hydrocarbon tails.

dimerization behavior [202].

Mostly the mechanism of Förster-type resonant energy transfer (FRET) is applied [13,15,81,82,215,217,258–260]. The FP is selected according to the spectral requirements (wavelength region of absorption and emission, overlap of donor fluorescence spectrum and acceptor absorption spectrum, efficiency of energy transfer, fluorescence quantum yield of energy acceptor).

The voltage sensitive probes are: i) membrane mobile molecules [117,262], ii) transmembrane genetically encoded mutated microbial rhodopsins with retinal chromophore [12,88,124,242,243,263], iii) voltage sensitive domains based on voltage sensitive phosphatase like *Ciona intestinalis* (Ci-VSP) [179–181,188,189,193,264–271], *Gallus gallus* [167,187,272–274], and others [200,202,275], iv) voltage sensitive domains of voltage-gated ion channels [84–86,276], and v) chimeric ion channels and phosphatases [277,278].

4.3.1. FRET-based fluorescent proteins in connection with intramembrane mobile molecules

An intracellular membrane anchored FP (farnesylated enhanced green fluorescent protein eGFP-F) was used with intramembrane negatively charged molecule dipicrylamine (DPA$^-$) for FRET based membrane voltage determination [117,262]. This hybrid voltage sensor is named hVOS [117]. Its characteristic parameters are response time τ_{resp} ≈ 500 µs and fractional fluorescence change $\Delta F/F$ = 5-34 %. Under

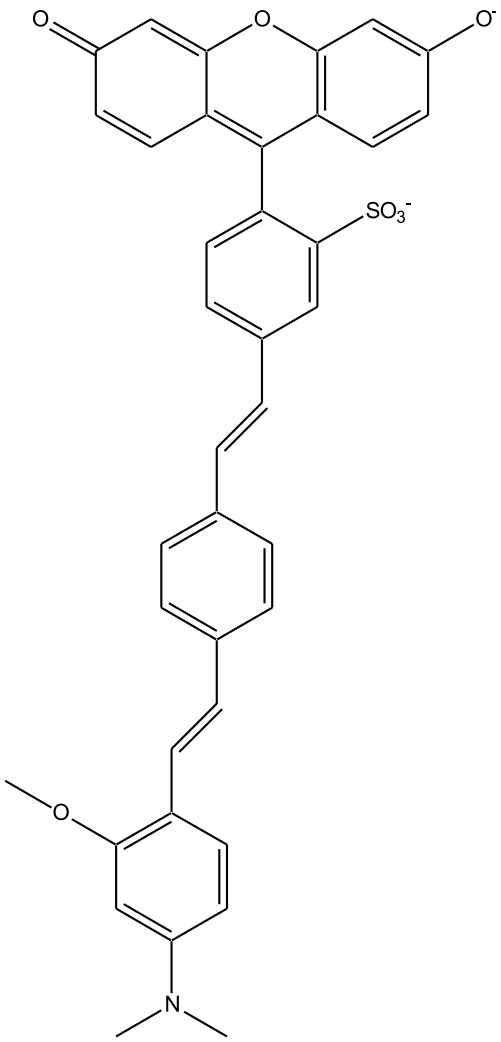

Fig. 17. Structural formula of the sulfofluorescein based VoltageFluor dye VF2.1(OMe).H (taken from [148]).

intracellular negative charged membrane conditions, DPA^- is located at the extracellular membrane side (weak FRET interaction) and eGFP-F is strongly fluorescent. Under intracellular positive charged membrane conditions, DPA^- is located at the intracellular membrane side near to eGFP-F (strong FRET interaction) and its fluorescence emission is quenched.

4.3.2. FRET-based fluorescent proteins probe protonation state of retinal in transmembrane microbial rhodopsins

An appropriate fluorescent protein is intracellularly fused to a microbial rhodopsin-derived voltage sensor in the cell membrane [88,117,124,242,243,263]. The membrane voltage influences the neutral retinal Schiff base (RSB) /protonated retinal Schiff base (PRSB) equilibration, and the FP interacts with PRSB via FRET (see Section 3.3).

Various negative-going FRET based genetically encoded fluorescent protein/rhodopsin voltage indicators have been realized:

Ace-mNeon [263] (Ace = *Acetabularia acetabulum* rhodopsin, mNeon = mNeonGreen fluorescent protein), $\tau_{resp} \approx 1$ ms, $\Delta F/F \approx$ -10 %;
Ace-mScarlet [243], $\tau_{resp} \approx 2$ ms, $\Delta F/F \approx$ -8 %;
VARNAM (voltage-activated red neuronal activity monitor, a fusion of Ace with mRuby3) [242], $\tau_{resp} \approx 1$ ms, $\Delta F/F \approx$ -13 %;
Mac-mOrange2 and *Mac-mCitrine* (Mac = rhodopsin blue-green light-activated proton pump from fungus *Leptosphaeria maculans*) [88], $\tau_{resp} \approx 3$ ms, $\Delta F/F \approx$ -12 %;
QuasAr2-FP, FP = eGFP, Citrine, mOrange, or mRuby2 (QuasAr = Quality superior to Arch, an Archaerhodopsin 3 mutant from *Halorubrum sodomense*) [124], $\tau_{resp} \approx$ 4-7 ms, $\Delta F/F \approx$ -(8-13) %;
paQuasAr3-Citrine (paQuasAr3 = photoactivated QuasAr3) [12], $\tau_{resp} < 1$ ms, $\Delta F/F \approx$ -40 %;
QuasAr6a-Citrine ($\tau_{resp} \approx 1.8$ ms, $\Delta F/F \approx$ -73 %) and *QuasAr6b-Citrine* ($\tau_{resp} \approx 0.8$ ms, $\Delta F/F \approx$ -24 %) [279].

Positive-going FRET based genetically encoded fluorescent protein/rhodopsin voltage indicators have been realized with similar response time and fractional fluorescence change as their negative-going counterparts [161].

4.3.3. Fluorescent proteins report status of voltage sensitive domain from voltage sensitive phosphatase of Ciona intestinalis (Ci-VSP)

The voltage sensitive domain VSD (S1-S4) from the voltage-sensitive phosphatase of the sea squirt *Ciona intestinalis* (Ci-VSP) responds to the electrical potential of the membrane. Especially the position of the positive charged strand S4 is influenced by the membrane voltage and modifies the fluorescence behavior of the fluorescent protein(s) fused to the Ci-VSP-based GEVI [13,81,82,217]. Fluorescent protein FRET based VSDs have two spectrally adjusted fluorescent proteins fused to the voltage sensitive domain (S1-S4) which change their distance with the membrane voltage (restructuring of S1-S4 strands) and thereby change the FRET efficiency [179,181,264–268]. VSDs of Ci-VSP-based GEVIs with a fused single fluorescent protein or a circular permuted fluorescent

protein imply a change of the FP fluorescence efficiency due to the electric field VSD restructuring acting on the β-barrel structure with subsequent chromophore environment modification [180,188,189,193,269–271]. VSDs from Ci-VSP based mosaic GEVIs with single fused superecliptic pHluorin A227D mutants with negative charge on the outside of the β-can imply membrane voltage dependent fluorescent protein monomerization/dimerization with accompanying fluorescence modulation [196–201]. Also, VSDs from Ci-VSP based mosaic GEVIs with single fused dTomato show membrane voltage dependent fluorescent protein monomerization/dimerization [202].

4.3.3.1. Two fluorescent proteins fused to VSD of Ci-VSP. Several GEVIs based on membrane voltage dependent FRET efficiency between two FPs fused to the VSD of Ci-VSP have been realized (mechanism explained in Section 3.4.3):

VSFP2.3: fusion of the FPs mCerulean and Cirtrine in tandem to VSD (S1-S4) of Ci-VSP, $\tau_{resp} \approx 100$ ms, fluorescence ratio $\Delta R/R \approx 10$ %, (VSFP = genetically encoded voltage sensitive fluorescent protein) [176,265];
VSFP CR: the FPs Clover and mRuby2 are fused to VSD of Ci-VSP [265], $\tau_{resp} \approx 50$ ms, fluorescence ratio $\Delta R/R \approx 12$ %;
Mermaid: the FPs mUKG and mKOκ from corals are fused to S4 of VSD of Ci-VSP, $\tau_{resp} \approx 20$ ms, fluorescence ratio $\Delta R/R \approx 40$ % (Mermaid = membrane-potential reporter made of ascidian and dual coral fluorescent proteins) [181];
Mermaid2: two FPs fused to S1 and S4 of VSD of Ci-VSP, several versions of FPs are used (mUKG + mKOκ, CFP + YFP, CFP_W66G + YFP, CFP + YFP_Y66G), $\tau_{resp} \approx 5$ ms, fluorescence ratio $\Delta R/R \approx 60$-100 % [266];
VSFP butterfly: the FPs mCitrine and mKate2 are fused to S1 and S4 of VSD of Ci-VSP, $\tau_{resp} \approx 10$ ms, fluorescence ratio $\Delta R/R \approx 22$ % [267];
Nabi: FPs mUKG and mKO (Nabi1) or Clover and mRuby2 (Nabi2) are fused to S1 and S4 of VSD of Ci-VSP, $\tau_{resp} = 2$-6 ms, fluorescence ratio $\Delta R/R \leq 11$ % (Nabi is name of butterfly in Korean) [268].

4.3.3.2. One FP or cpFP fused to S4 of VSD of Ci-VSP. Several Ci-VSP based GEVIs have been developed using FPs or cpFPs intracellularly fused to the S4 strand of the VSD. Their membrane voltage sensitivity is based on voltage dependent VSD restructuring influencing the β-barrel structure of the FP affecting the chromophore fluorescence behavior.

Examples are:

FlicR1: cpmApple is fused to S4 (FlicR = fluorescent indicator for voltage imaging red), $\tau_{resp} \approx 3$ ms, $\Delta F/F \approx 3$ % [193];
VSFP3.1: CFP is fused to S4, $\tau_{resp} \approx 3$ ms, $\Delta F/F \approx 10$ % [176,259];
VSFP3(x): various red fluorescent proteins (Cerulean, Citrine, mOrange2, TagRFP, mKate2) are fused to S4 of VSD of Ci-VSP [188].

4.3.3.3. One FP fused to S4 of VSD of Ci-VSP with dimerization tendency. Ci-VSP based mosaic GEVIs with single fused superecliptic pHluorin mutants have been developed which tend to FP dimerization under depolarization conditions [196–201] (see Section 3.4.2). Besides the dimerization tendency, the VSD restructuring acts on the β-barrel structure of the fused superecliptic pHluorin mutants which influence the chromophore environment and fluorescence behavior [195].

Examples are:

ArcLight: superecliptic pHluorin with mutation A227D is fused to S4 of VSD of Ci-VSP, $\tau_{resp} \geq 10$ ms, $|\Delta F/F| \leq 35$ % [180,271,275];
Bongwoori: voltage indictor like ArcLight with modified linker, $\tau_{resp} \approx 10$ ms, $|\Delta F/F| \leq 20$ % (Bongwoori is Korean name of mountaintop) [270,280];
Marina: ArcLight with D389A H390A Y442V mutations in superecliptic pHluorin fluorescent protein (polarity of fractional fluorescence change is inverted), $\tau_{resp} \approx 30$ ms, $\Delta F/F \approx 30$ % [281,282];
Ulla: ArcLight derived GEVI with superecliptic pHluorin mutation T204E/F223D (polarity of fractional fluorescence change is inverted), fast response, $\Delta F/F \geq 25$ % [195] (Ulla = ascend in Korean)
Ilmol: FP dTomato is fused to S4 of VSD of Ci-VSP. Two adjacent VSDs, each with a single dTomato act together tending to form dTomato dimer under depolarization conditions, $\tau_{resp} \approx 5$ ms, $|\Delta F/F| \approx 4$ % [202] (Ilmol = sunset in Korean).

4.3.3.4. Chimeric voltage sensitive domains with potassium ion channel Kv3.1 part in Ci-VSP. The voltage sensitive domain (VSD) of Ci-VSP was modified by partial replacement of parts of VSD with parts from potassium ion channel Kv3.1.

Examples are,

chimeric VSFP butterflies: two FPs (CFP and YFP, or YFP and RFP) are fused to the chimeric VSD [277,278], $\tau_{resp} \approx 23$ ms, $\Delta F/F \approx 4$ % [269];
VSD-FR189-188: cpFusionRed permutant at breaking point 189-188 was fused to S1 and S4 of the chimeric VSD [269] (spatial separation mechanism of non-covalently bound parts of the split FP was applied), $\tau_{resp} \approx 27$ ms, $\Delta F/F \approx 2$ %;
nirButterfly: The FPs miRFP670 and miRFP720 were fused to the chimeric VSD [283,284], $\tau_{resp} \approx 2.2$ ms, $\Delta F/F \approx 16$ %.

4.3.4. Fluorescent proteins report status of voltage sensitive domain from voltage sensitive phosphatase of chicken Gallus gallus (Gg-VSP)

Extracellular single FPs were fused to the S1-S4 voltage sensitive domain (VSD) of the voltage sensitive phosphatase of chicken *Gallus gallus*.

Examples are:

ASAP1: cpGFP is fused to S4 of Gg-VSP (ASAP = accelerated sensor of action potential) [187], $\tau_{resp} \approx 2$ ms, $|\Delta F/F| \approx 20$ %;
ASAP2s: ASAP1 with mutation R415Q in S4 which perturbs the chromophore behavior of cpGFP resulting in changes of the fluorescence emission [272], $\tau_{resp} \approx 5$ ms, $|\Delta F/F| \approx 40$ %.;
ASAP3: Improved ASAP variant found by library-based mutagenesis screening [182], $\tau_{resp} \approx 12$ ms, $|\Delta F/F| \approx 50$ %;
ASAP4: Various mutations of ASAP2 with positive going voltage response, similar response time and higher fractional fluorescence change, e.g. $\Delta F/F = 180$ % for ASAP4b [285];
ASAP5: ASAP3 145A,149K,412V,413I,414R, has higher gain and faster onset time constant than ASAP3 [45];
SpikeyGi and *SpikeyGi2*: mutated ASAP3 variants [286], $\tau_{resp} \approx 2$ ms, $|\Delta F/F| \approx 18.7$ % for SpikeyGi and $|\Delta F/F| \approx 57.5$ % for SpikeyGi2;
JEDI-1P: cpGFP is fused to VSD of Gg-VSP and used for 1-photon microscopy (JEDI = jellyfish-derived electricity-reporting designer indicator) [287], $\tau_{resp} \approx 1.6$ ms, $|\Delta F/F| \approx 55$ %;
JEDI-2P: FP cyOFP1 is fused to VSD of Gg-VSP for 2-photon microscopy [274], $\tau_{resp} \approx 35$ ms, $|\Delta F/F| \approx 50$ %.

4.3.5. Fluorescent proteins integrated in voltage-gated ion channels for membrane voltage reporting

Like voltage-gated phosphatases, voltage-gated ion channels contain a four-segment voltage sensitive domain VSD (S1-S4) which regulates the ion transport through the pore according to the membrane potential [164–166]. Genetically encoded membrane voltage indicators have been developed by fusing fluorescent proteins as reporters to the voltage-gated ion channels [277]. Potassium ion channels [86], sodium ion channels [85], and proton ion channels [86] have been used.

A modified green fluorescent protein (GFP) was fused into the Shaker K^+ channel at the strand S6 so that voltage-dependent rearrangements in

the K^+ channel induced changes in the fluorescence of GFP [84]. It was called *Flash* for fluorescent Shaker. A voltage-sensitive fluorescent protein (named VSFP1) consisting of a voltage sensing domain of Kv2.1 channel and a fluorescent protein pair, CFP and YFP, was designed to record membrane potential dynamics (fluorescent protein pair fused to S4 of Kv2.1, rotational movement of S4 caused change of FRET efficiency due to reorientation of fluorescent proteins, eoFRET) [125,126].

A sodium channel fluorescent protein-based membrane voltage activity reporting construct (named *SPARC*) was developed consisting of GFP intracellularly inserted between S6 of part II and S1 of part III of the sodium ion channel tetramer [85,276]. Rapid changes of the membrane potential modulated the fluorescence of the inserted GFP.

A voltage-gated proton channel from Chinese liver fluke *Clonorchis sinenis* with fluorescent proteins mKate2 and superecliptic pHluorin A227D allowed to optically monitor the membrane potential [86]. The system was named Pado (Pado = wave in Korean).

4.4. Voltage-gated ion channels

The membrane voltage of voltage-gated ion channels regulate and trigger their channel permeability and activity [164,169]. The Na^+ and Ca^{2+} channels consist of a single-polypeptide chain that comprises four repeats (I, II, III, IV) each consisting of six membrane-spanning segments (S1-S6) of which S1-S4 comprise the voltage sensing domain (VSD) and S5-S6 form the pore [164]. K^+ channels consist of four noncovalent subunits forming a tetramer, each subunit (S1-S6) is composed of a voltage sensing domain (S1-S4) and a pore part (S5-S6). The inner part of the tetramer forms the ion channel (four S5-S6 segments) and the outer part forms the voltage sensitive part (four S1-S4 segments) [164]. The H^+ channel is a dimer of two S1-S4 regions (without S5-S6 pore) held together by coiled-coil interactions in the C-terminal domain, in which each monomer has its own proton conduction pathway [288].

The S4 segment in each VSD contains three to eight repeated three-residue motifs of a positive amino acid (mostly arginine R, sometimes lysine K) followed by two hydrophobic amino acid residues. These positive amino acids are sensitive to the electric field in the membrane, so that S4 moves towards the intracellular or extracellular space upon intracellular negative or positive charged membrane conditions, respectively (sliding helix or helical screw model [228,290]) [164,173,288–296].

The membrane voltage determination is achieved by fusing an appropriate fluorescent protein to the voltage-gated channel which responds to the membrane voltage dependent structural change of the voltage sensing domain S1-S4 (see Section 4.3.5).

4.5. Voltage sensitive phosphatases

A phosphatase is an enzyme that uses water to cleave a phosphoric acid monoester into a phosphate ion and an alcohol [297,298]. Voltage sensitive phosphatases (VSPs) consist of a transmembrane voltage sensing domain (VSD) of four transmembrane strands (S1-S4) connected to a cytoplasmic phosphatase region that dephosphorylates phosphoinositides (PIPs) in the membrane in case of membrane depolarization [174,179,299–301]. VSPs are found in many species including humans, mice, zebrafish, frogs, chicken, and sea squirt [275].

The voltage-sensitive phosphatase Gg-VSP in chick embryonic tissues and in the adult cerebellum of chicken *Gallus gallus domesticus* plays a role in embryonic cell process outgrowth and is involved in the differentiation of Purkinje neurons [30,302].

4.6. Microbial rhodopsins

Microbial rhodopsin based genetically encoded voltage indicators (GEVIs) have been reviewed in [13,15,81,82,160,217,258,260,294,302–304].

Microbial rhodopsins consist of an opsin protein and a covalently bound retinal chromophore [273,306]. The opsin apoprotein is built up of seven transmembrane α-helices (TM1-TM7) with N-terminus located extracellular and C-terminus located intracellular. The retinal is attached by a Schiff base linkage to the ε-amino group of a lysine side chain in the middle of TM7 (retinal + lysine → retinal Schiff base + H_2O). In the dark-adapted form, retinal is present in all-*trans* configuration. Photoexcitation causes isomerization to the 13-*cis* conformation. Microbial rhodopsins have been identified from archaea, bacteria, eukaryotic microorganisms and viruses with a variety of distinct functions (pumps, channels, regulators, sensors) [307,308].

The structural formulae of all-*trans* retinal, all-*trans* protonated retinal Schiff base (all-*trans* PRSB), 13-*cis* protonated retinal Schiff base (13-*cis* PRSB), all-*trans* retinal Schiff base (all-*trans* RSB), and 13-*cis* retinal Schiff base (13-*cis* RSB) are shown in Fig. 18.

Microbial rhodopsin light-driven outward proton pumps transfer intracellular H^+ to the extracellular side in a photocycle. This photocycle is initiated by photoexcitation of all-*trans* ground-state protonated retinal Schiff base ($PRSB_t$) to a local excited state ($PRSB_t$*), followed by excited-state 13-*cis* isomerization ($PRSB_c$), then protein restructuring leading to H^+ transfer to the extracellular side and $PRSB_c$ deprotonation to neutral retinal Schiff base RSB_c. It follows further restructuring with a re-protonation of the isomerized RSB_c from the intracellular side to $PRSB_c$. Then it follows re-isomerization to all-*trans* $PRSB_t$ and ground-state restoration to the original dark-adapted situation [273,305,306,309,310].

This microbial rhodopsin light-driven outward proton pump photocycle scheme is shown in Fig. 19 (following [306]).

The most studied microbial rhodopsin light-driven outward proton pump is bacteriorhodopsin (BR) from halophilic archaea *Halobacterium salinarum* [311,312]. Important microbial rhodopsin outward proton pumps, whose mutants find important application as membrane voltage indicators, are: proteorhodopsin from an uncultivated γ-proteobacterium occurring in marine bacterioplankton [313–315], archaerhodopsin 3 (Arch, also abbreviated Arch 3 or Arch3) from *Halorubrum sodomense* [87,316–319], Mac rhodopsin from fungal pathogen *Leptosphaeria maculans* [88], and *Acetabularia* rhodopsin I and II proton pumps from marine alga *Acetabularia acetabulum* [320,321].

Microbial rhodopsin-based GEVIs are mutated microbial rhodopsin light-driven outward proton pumps where the proton pumping is blocked by replacing an acidic amino acid (Asp, D) involved in the light-driven outward proton transfer with a neutral amino acid (Asn, N) [87,124,158]. They exhibit a membrane voltage sensitivity because their PRSB - RSB equilibrium depends on the membrane potential [87,124,158,322]. Generally, the proton pathway from retinal to the extracellular membrane leaflet is blocked by D-N mutation of the proton acceptor from the protonated retinal Schiff base leading to negative-going rhodopsin -based GEVIs (see Section 3.3.1). In a recent paper [161], the proton pathway from the intracellular membrane leaflet to the retinal was blocked by D-N mutation of the proton donator to the retinal Schiff base leading to positive-going rhodopsin-based GEVIs (see Section 3.3.2).

A photocycle scheme for protonated retinal Schiff base in intracellular positive charged membranes of negative-going rhodopsin-based GEVIs, or intracellular negative charged membranes in positive-going rhodopsin-based GEVIs, is shown in Fig. 20 [323–325].

In the primary cycle, the protonated retinal Schiff base in its thermally stable original dark-adapted S_0 ground-state ($PRSB_t$) is photoexcited to its locally excited state ($PRSB_t$*) in the S_1 potential energy surface. From there the S_1 state isomerization begins along a torsional reaction coordinate via the stationary point SP (dominant fluorescence emission position), the funnel state Fu with S_1-S_0 internal conversion to the S_0 transition state. From there occurs either return to the original ground state ($PRSB_t$) or further torsion towards the ground-state photoisomer $PRSB_c$. This state is thermally unstable and recovers slowly back to the original configuration by ground-state back-isomerization.

Continued light exposure excites the formed photoisomer $PRSB_c$ in a

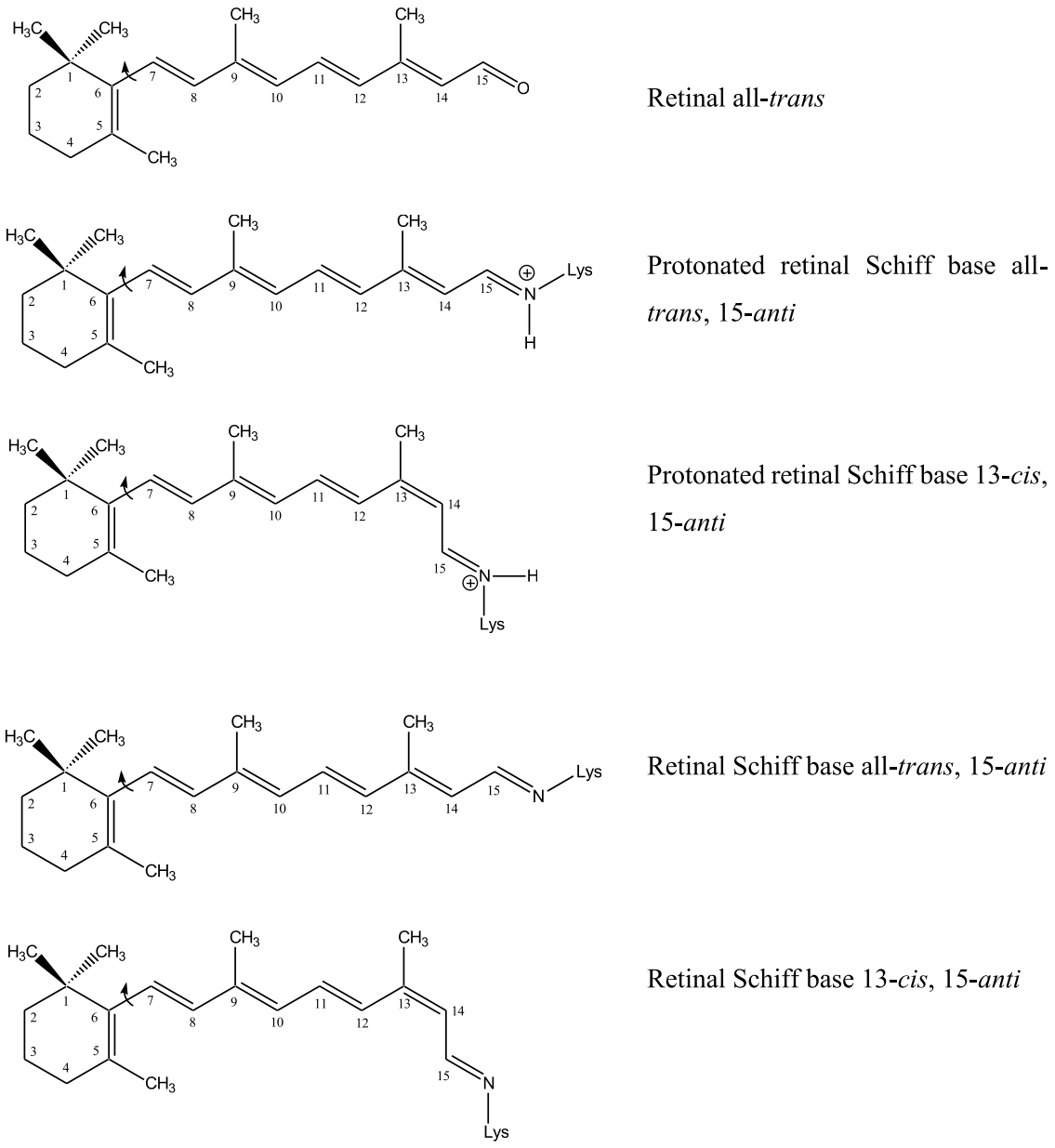

Fig. 18. Structural formulae of all-*trans* retinal, all-*trans* protonated retinal Schiff base (all-*trans* PRSB), 13-*cis* PRSB, all-*trans* retinal Schiff base (all-*trans* RSB), and 13-*cis* RSB (see [18]).

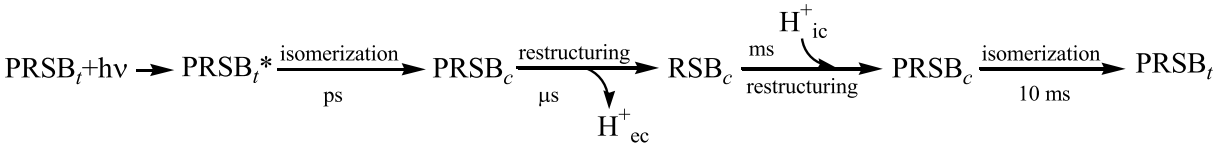

Fig. 19. Photocycle scheme of a rhodopsin light-driven proton pump. PRSB$_t$: ground-state all-*trans* protonated retinal Schiff base. PRSB$_t$*: excited-state all-*trans* protonated retinal Schiff base. PRSB$_c$: photoisomerized ground-state 13-*cis* protonated retinal Schiff base. RSB$_c$: ground-state 13-*cis* retinal Schiff base. H^+_{ec}: proton released to extracellular space. H^+_{ic}: proton taken up from intracellular space. Approximate durations of the processes are indicated (ps, μs, ms, 10 ms).

secondary photocycle with photoisomerization of PRSB$_c$ to PRSB$_t$. Under continued light exposure this primary and secondary photocycling occurs repeatedly. The exact dynamics depends on the excitation light intensity, excitation light duration, and excitation light frequency [326] (PRSB$_t$ and PRSB$_c$ have different S_0-S_1 transition frequencies and fluorescence behavior [323–325]).

4.6.1. Stand-alone rhodopsin (opsin-only) GEVIs

The fluorescence quantum yield of microbial rhodopsin based GEVIs is rather low. It is determined by the photoisomerization dynamics. It was increased by directed mutations which slow down the photoisomerization process along the excited-state torsional reaction coordinate via a stationary point SP [159,305,323–325,327,328]. The mutations resulted in a wide variety of Arch based GEVIs [11,87,

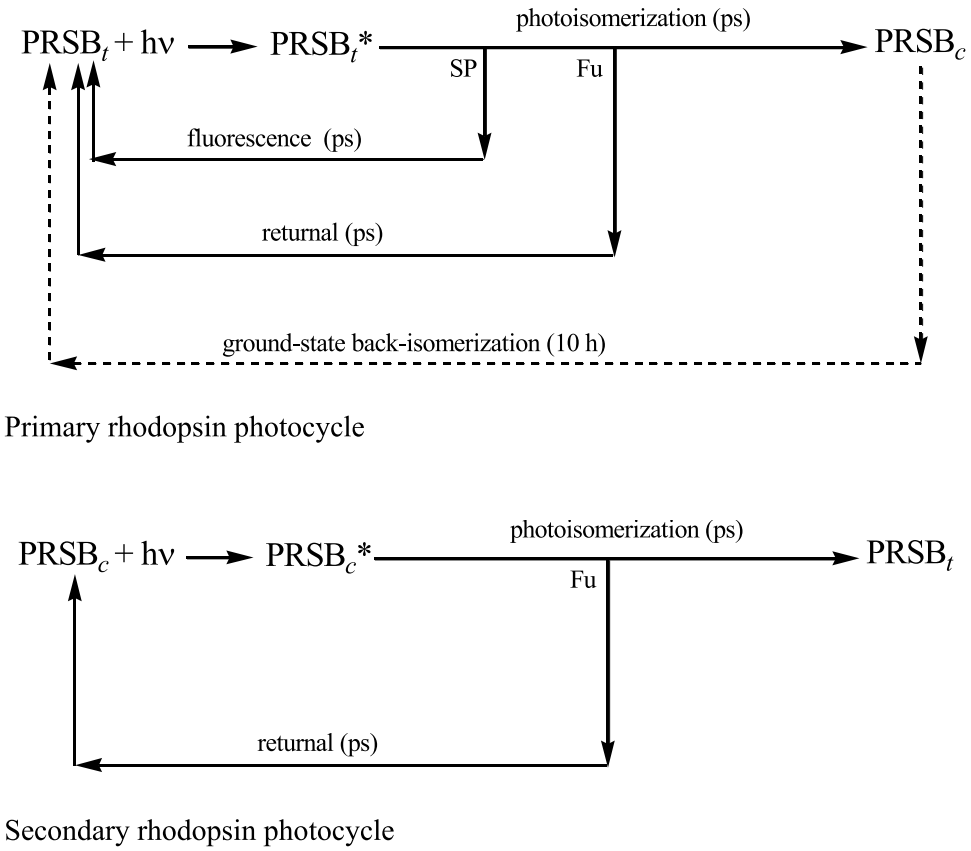

Fig. 20. Photocycles schemes of protonated retinal Schiff base in rhodopsin-based GEVIs. Top part: primary PRSB photocycle of dark-adapted sample. Bottom part: secondary PRSB photocycle of photoisomerized PRSB generated in primary photoexcitation process. PRSB: ground-state protonated retinal Schiff base. PRSP*: excited-state protonated retinal Schiff base. SP: stationary point on S_1 state potential energy surface (from there dominant fluorescence emission). Fu: funnel state (there S_1-S_0 internal conversion to S_0 transition state with forward reaction to photoisomer and backward reaction to original conformation). In schemes is assumed: PRSB$_t$ = thermal stable original (dark-adapted) isomer. PRSB$_c$: in primary photocycle generated photoisomer which thermally recovers back to PRSB$_t$ by thermal ground-state isomerization.

329–338]. Some obtained fluorescence quantum yields ϕ_F are:

wt Arch 3: $\phi_F = 1.1 \times 10^{-4}$ [336,339],
Arch 3 D95N: $\phi_F = 4 \times 10^{-4}$ [87],
Proteorhodopsin D97N: $\phi_F = 1 \times 10^{-3}$ [158],
QuasAr1: $\phi_F = 6.5 \times 10^{-3}$ [163],
Arch 5: $\phi_F = 8.7 \times 10^{-3}$ [336],
Arch 3 D95E/T99C/P196S/T215A: $\phi_F = 9.7 \times 10^{-3}$ [338],
Archon2: $\phi_F = 1.05 \times 10^{-2}$ [340],
Arch 7: $\phi_F = 1.2 \times 10^{-2}$ [336].

Modification of retinal to 3-methylamino-16-nor-1,2,3,4-didehydroretinal in the Arch mutants QuasAr1 and QuasAr2 led to red-shifted membrane voltage sensors [341].

4.6.2. *Fluorescent protein-rhodopsin based GEVIs*

To overcome the moderate PRSB fluorescence efficiency of the wide variety of Arch-mutant GEVIs, they were fused with appropriate fluorescent proteins capable of FRET energy transfer from fluorescent protein to PRSB [124,332,333,342–345]. They are negative-going GEVIs, i.e. the retinal to extracellular membrane H^+ pathway is blocked (see Section 3.3.1). Under hyperpolarizing conditions, the retinal Schiff base is present in neutral near UV absorbing form (RSB) without FRET interaction, and the blue/green absorbing FPs are efficiently fluorescing in the green/yellow spectral region. Under depolarizing conditions, the retinal Schiff base is present in protonated form (PRSB) absorbing in the green/yellow spectral region quenching the FP emission by FRET energy transfer from FP to weakly emitting PRSB [124].

The Arch-FP based GEVIs have been extended to other FRET based mutated rhodopsin light-driven proton pump – fluorescent protein GEVIs [88,263].

To them belong the negative-going GEVIs:

Mac GEVIs (rhodopsin from *Leptosphaeria maculans*, proton pump inactivated mutants): MacN = Mac D139N, MacQ = Mac D139Q, FPs: mCitrine and mOrange2 [87]
Ace GEVIs (rhodopsin from *Acetabularia acetabulum*): Ace1Q-mNeongreen and Ace2N-nNeonGreen [263], VARNAM = Ace-mRuby3 [217], and Ace2N-mScarlet [243].

Also, positive-going GEVIs, were realized, There the intracellular membrane to retinal H^+ pathway was blocked (see Section 3.3.2). They include Ace2 with mNeonGreen and Ace2 with mRuby3 [161].

4.6.3. *Chemogenetic dye-rhodopsin based GEVIs*

Instead of fluorescent proteins, organic dyes tagged to rhodopsin Ace have been developed for membrane voltage detection employing FRET between intracellular dye and retinal. One speaks of chemogenetic GEVIs or hybrid protein – small molecule GEVIs [89,346,347].

Examples of negative-going chemogenetic GEVIs are:

FlareFRET: fluorophore-ligation-assisted rhodopsin eFRETs like Ace-L1-Cy3 called Flare1 [347],
Voltron: Ace2N-HaloTag-Janelia Fluor (JF) dye [89],
Voltron2: Voltron A122D [348],

HVI-Cy3 and *HVI-Cy5*: Ace2N-cyanine dye hybrid voltage indicators [346].

Examples of positive-going chemogenetic GEVIs, named *Positron* voltage indicators are [161]:

Ace2 with HaloTag containing dye JF_{525},
Ace2 with HaloTag containing dye JF_{585},
Ace1 with HaloTag containing dye JF_{525}, and
Mac with HaloTag containing dye JF_{525}.

4.7. All-optical electrophysiology

In all-optical electrophysiology the cell membranes are stimulated by optogenetic activation, and the induced membrane potential dynamics are probed with voltage sensitive optical probes [11,349–354]. For optogenetic activation mostly channelrhodopsin 2 [355] is genetically encoded in the cell membrane of interest.

5. Conclusions

Biological cells and cellular compartments are surrounded by membranes and the membrane potential steers the cellular functioning. The membrane potential probing is essential for understanding cellular processes, especially for neurons and cardiac cells.

In this paper membrane potential fundaments were developed. The classical electrophysiology was described. Then the electric field dependent probe effects, acting in optical membrane voltage probes, were described. The developed probes, utilizing voltage sensitive dyes, nanoparticles, fluorescent proteins, voltage-gated ion channels, voltage-gated phosphatases, and microbial rhodopsins, were discussed. Table 2 gives an overview of applied membrane voltage probes concerning their

Table 2
Overview of applied membrane voltage probes.

Probe	Localization	Mechanism	Response time τ_{resp}	Signal	Fractional signal change $\lvert\Delta S\rvert/S$	References
Dyes						
Ionic dye (slow dye)	Intracellular and extracellular	Nernstian diffusion through membrane	> 1 s	Absorption or fluorescence	≈ 100 % [29]	[29,77,90]
Electrochromic dye (fast dye)	Intramembrane at extramembrane leaflet	Molecular Stark effect	≈ 1 ns	Absorption or fluorescence	2-10 % [29]	[6,7,29,78,91,92,95,96]
Energy donor-acceptor pair	Part at extramembrane leaflet, other part mobile in membrane	esFRET,	0.4-10 s [79]	FRET fluorescence	< 10 % [79]	[79,115,116]
			< 0.4 ms [116]		> 50 % [116]	
Electron donor-acceptor pair (fluorophore-wire-aniline)	Fluorophore at membrane leaflet, aniline in membrane	PeT_o	< 1 ms [142]	PeT quenches fluorescence emission	≈ 50 % [142]	[142,147–152]
Tautomeric dye	Intramembrane	ESIPT	< 1 ms	Emission from normal or tautomeric state. Two-band ratiometric response	≈ 15 %	[153]
Nanparticles						
Semiconductor nanorod bioconjugate	Intramembrane	QCSE	< 3.5 ms [104]	Absorption/emission spectral shift	< 69 % [104]	[80,104–108]
Lanthanide upconversion nanoparticle + DPA	UCNP at extramembrane leaflet, DPA mobile in membrane	esFRET	≈ 20 ms	FRET fluorescenc	< 10 %	[122]
Fluorescent proteins						
FP + DPA	FP: membrane leaflet DPA^-: intramembrane mobile	esFRET	≈ 0.5 ms [117]	FRET fluorescence	≤ 34 % [117]	[117,231,262]
Phosphatase based GEVIs						
Ci-VSD + FP(s)	Transmembrane VSD and intracellular FP(s)	Displacement of segment S4 of VSD	≤ 10 ms	Emission of FP is modified by S4 position	≤ 50 %	[157,176,188,192,202,264–268,270,271,281–283]
Gg-VSD + FP	Transmembrane VSD and extracellular FP	Displacement of segments S3, S4 of VSD	≤ 20 ms	Emission of FP is modified by S3 and S4 position	≤ 50 %	[167,182,187,272,274,287]
Rhodopsin based GEVIs						
Arch derivative + FP	Transmembrane rhodopsin + intracellular FP	ecFRET	4-7ms [124]	FRET fluorescence	8-13 % [124]	[12,124,279,280,343]
Ace + FP	Transmembrane rhodopsin + intracellular FP	ecFRET	≈ 3 ms [242]	FRET fluorescence	5-12 % [242]	[242,243,263]
Mac + FP	Transmembrane rhodopsin + intracellular FP	ecFRET	≈ 5 ms	FRET fluorescence	≈ 20 %	[88]
Ace + tagged dye	Transmembrane rhodopsin + tag with synthetic dye	ecFRET	< 1 ms [89]	FRET fluorescence	≈ 23 % [89]	[89,161,346–348]
Mac + tagged dye (positive going)	Transmembrane rhodopsin + tag with synthetic dye	ecFRET	< 50 ms	FRET fluorescence	≈ 3 %	[161]
Arch derived, stand-alone	Transmembrane, outward H^+ pumping pathway is blocked	GSIPT	< 1 ms	PRSB fluorescence	> 100 %	[11,87,158,317]

Abbreviations: Ace = rhodopsin from *Acetabularia acetabulum*. Arch = archaerhodopsin from *Halorubrum sodomense*. Ci-VSP = *Ciona intestinalis* voltage-sensitive phosphatase. DPA = dipicrylamine. ESIPT = photoinduced excited-state intramolecular proton transfer. ecFRET = electrochromic FRET. esFRET = electro-spatial FRET. FRET = Förster-type resonant energy transfer. FP = fluorescent protein. GEVI =genetically encoded voltage indicator. Gg-VSP = *Gallus gallus* voltage sensitive phosphatase. GSIPT = ground-state intermolecular proton transfer. Mac = rhodopsin from *Leptosphaeria maculans*. PeT = photoinduced electron transfer. PeT_o = photoinduced oxidative electron transfer. PRSB = protonated retinal Schiff base. ΔS/S = (change of signal strength due to 100 mV depolarization)/(signal strength at resting potential). UCNP = upconversion nanoparticle. VSD = voltage sensitive domain.

localization, mechanism, response time and fractional signal change.

The genetically encoded voltage indicators enable probing functional neural circuits [198,349,356–358] and cardiac tissue [359] at high spatiotemporal resolution. The research field is very active, optimizing the voltage indicators to the voltage imaging tasks in cell cultures and in live animals. One-photon and two-photon excitation techniques as well as various microscopic and deep-tissue imaging methods are applied [360,361].

Further physical phenomena are exploited towards label-free membrane voltage sensing [362,363] like mechanical deformation followed by plasmonic imaging [364] or atomic force microscopy [365], light scattering detection [366], crossed-polarizer birefringence measurement [367], optical magnetic detection [368], low -coherence interferometric microscopy [369,370], hyperspectral stimulated Raman scattering [371–373], second harmonic generation [374], field-dependent optical absorption in a graphene film [375], electrochromic optical recording of spontaneous neuroelectric activities with polystyrene sulfonate (PEDOT:PSS) thin films [376,377], and all-optical trionic biological voltage sensing with monolayer MoS_2 semiconductors [378].

Data availability

No data was used for the research described in the article.

Dedication

The paper is dedicated to my wife Gisela Penzkofer, née Loebe, 1934-2024.

CRediT authorship contribution statement

Alfons Penzkofer: Writing – original draft, Validation, Supervision, Project administration, Methodology, Investigation, Conceptualization.

Declaration of competing interest

The author declares that he has no known competing financial interests or personal relationships that could have appeared to influence the work reported in this paper.

Acknowledgements

The author thanks Prof. F. J. Gießibl, University of Regensburg, for his kind hospitality. He is indebted to Prof. P. Hegemann, Humboldt University to Berlin for introduction into the field of photobiology and collegial cooperation.

References

[1] C. Anamourlis, The cell membrane, South. Afr. J. Anaesth. Analg. 26 (6 Suppl. 3) (2020) S1–S7. https://orcid.org/0000-0001-5509-2473.
[2] G.R. Dubyak, Ion homeostasis, channels, and transporters: an update on cellular mechanisms, Adv. Physiol. Educ. 28 (2004) 143–154, https://doi.org/10.1152/advan.00046.2004.
[3] J. Rettinger, S. Schwarz, J. Schwarz, Electrophysiology. Basics, Methods, Modern Approaches and Applications, 2nd ed., Springer Nature Switzerland AG, 2022.
[4] L. Fenno, O. Yizhar, K. Deisseroth, The development and application of optogenetics, Annu. Rev. Neurosci. 34 (2011) 389–412, https://doi.org/10.1146/annurev-neuro-061010-113817.
[5] K.D. Piatkevich, E.S. Boyden, Optogenetic control of neural activity: the biophysics of microbial rhodopsins in neuroscience, Quarterly Reviews of Biophysics 57 (2024) e1, https://doi.org/10.1017/s0033583523000033.
[6] L.B. Cohen, B.M. Salzberg, Optical measurement of membrane potential, Rev. Physiol. Biochem. Pharmacol. 83 (1978) 35–88, https://doi.org/10.1007/3-540-08907-1_2.
[7] L.M. Loew, Design and characterization of electrochromic membrane probes, J. Biochem. Biophys. Methods 6 (1982) 243–260, https://doi.org/10.1016/0165-022X(82)90047-1.
[8] M. Zochowski, M. Wachowiak, C.X. Falk, L.B. Cohen, Y.W. Lam, S. Antic, D. Zecevic, Imaging membrane potential with votage-sensitive dyes, Biological Bulletin 198 (2000) 1–21.
[9] M. Djurisic, S. Antic, W.R. Chen, D. Zecevic, Voltage imaging from dendrites of mitral cells: EPSP attenuation an spike trigger zones, J. Neurosci. 24 (2004) 6703–6714, https://doi.org/10.1523/jneurosci.0307-04-2004.
[10] W.-L. Zhou, P. Yan, J.P. Wuskell, L.M. Loew, S.D. Antic, Intracellular long-wavelength dyes for studying the dynamics of action potentials in axons and thin dendrites, J. Neurosci. Meth. 164 (2007) 225–239, https://doi.org/10.1016/j.jneumeth.2007.05.002.
[11] D.R. Hochbaum, Y. Zhao, S.L. Farhi, N. Klapoetke, C.A. Werley, V. Kapoor, P. Zou, J.M. Kralj, D. Maclaurin, N. Smedemark-Margulies, J.L. Saulnier, G.L. Boulting, C. Straub, Y.K. Cho, M. Melkonian, G.K. Wong, D.J. Harrison, V.N. Murthy, B. L. Sabatini, E.S. Boyden, R.E. Campbell, A.E. Cohen, All-optical electrophysiology in mammalian neurons using engineered microbial rhodopsins, Nat. Methods 11 (2014) 825–833, https://doi.org/10.1038/nmeth.3000.
[12] Y. Adam, J.J. Kim, S. Lou, Y. Zhao, M.E. Xie, D. Brinks, H. Wu, M.A. Mostajo-Radji, S. Kheifets, V. Parot, S. Chettih, K.J. Williams, B. Gmeiner, S.L. Farhi, L. Madisen, E.K. Buchanan, I. Kinsella, D. Zhou, L. Paninski, C.D. Harvey, H. Zeng, P. Arlotta, R.E. Campbell, A.E. Cohen, Voltage imaging and optogenetics reveal behavior-dependent changes in hippocampal dynamics, Nature 569 (2019) 413–417, https://doi.org/10.1038/s41586-019-1166-7.
[13] T. Knöpfel, C. Song, Optical voltage imaging in neurons: moving from technology development to practical tool, Nat. Rev. Neurosci. 20 (2019) 719–727, https://doi.org/10.1038/s41583-019-0231-4.
[14] M. Mank, O. Griesbeck, Genetically encoded calcium indicators, Chem. Rev. 108 (2008) 1550–1564, https://doi.org/10.1021/cr078213v.
[15] M. Sakamoto, T. Yokoyama, Probing neuronal activity with genetically encoded calcium and voltage fluorescent indicators, Neurosci. Res. (2024), https://doi.org/10.1016/j.neures.2024.06.004. S0168-0102(24)00076-2.
[16] H. Dana, Y. Sun, B. Mohar, B.K. Hulse, A.M. Kerlin, J.P. Hasseman, G. Tsegaye, A. Tsang, A. Wong, R. Patel, J.J. Macklin, Y. Chen, A. Konnerth, V. Jayaraman, L. L. Looger, E.R. Schreiter, K. Svoboda, D.S. Kim, High-performance calcium sensors for imaging activity in neuronal populations and microcompartments, Nat. Methods 16 (2019) 649–657, https://doi.org/10.1038/s41592-019-0435-6.
[17] Y. Zhang, L.L. Looger, Fast and sensitive GCaMP calcium indicators for neuronal imaging, J. Physiol. 602 (8) (2024) 1595–1604, https://doi.org/10.1113/P283832.
[18] A. Penzkofer, P. Hegemann, S. Kateriya, Organic dyes in optogenetics, in: F. J. Duarte (Ed.), Organic Lasers and Organic Photonics, 2nd ed., IOP Publishing, Bristol, 2024, 13-1–13-197.
[19] D. Voet, J.G. Voet, Biochemistry, 3rd ed., John Wiley & Sons, 2004. Chap. 20.
[20] B. Hille, Ion Channels of Excitable Membranes, 3rd ed., Sinauer, Sunderland, Massachusetts, USA, 2001, pp. 1–22.
[21] J.E. Hall, A.C. Guyton, Textbook of Medical Physiology, 12th ed., Elsevier Saunders, Philadelphia, USA, 2011, pp. 45–98. Unit II, Chapters 4-8.
[22] Kwang Suk Park, Humans and Electricity. Understanding Body Electricity and Applications, Springer Nature Switzerland AG, 2023.
[23] G. Picci, S. Marchesan, C. Caltagirone, Ion channels and transporters as therapeutic agents: from biomolecules to supramolecular medical chemistry, Biomedicines 10 (2022) 885, https://doi.org/10.3390/biomedicines10040885.
[24] J. Kulbacka, A. Choromańskaz, J. Rossowska, J. Weżgowiec, J. Saczko, M-P. Rols, Cell membrane transport mechanisms: ion channels and electrical properties of cell membranes, Adv. Anat. Embryol. Cell Biol. 227 (2017) 39–58, https://doi.org/10.1007/978-3-319-56895-9_3.
[25] A.L. Hodgkin, A.F. Huxley, A quantitative description of membrane current and its application to conduction and excitation in nerve, J. Physiol. 117 (1952) 500–544, https://doi.org/10.1113/jphysiol.1952.sp004764.
[26] I. Skaliora, M. Mavroidis, E. Kouvelas, Basis of cell excitability and cardiac conduction system, in: D.V. Cokkinos (Ed.), Introduction to Translational Cardiovascular Research, Springer International Publishing, Switzerland, 2015, pp. 31–47.
[27] O.S. Andersen, Cellular electrolyte metabolism, in: R.H. Kretsinger, V.N. Uversky, E.A Permyakov (Eds.), Encyclopedia of Metalloproteins, Springer, New York, NY, 2013, pp. 580–587, https://doi.org/10.1007/978-1-4614-1533-6_223.
[28] E. Gross, R.S. Bedlack, L.M. Loew, Dual-wavelength ratiometric fluorescence measurement of the membrane dipole potential, Biophys. J. 67 (1994) 208–216, https://doi.org/10.1016/S0006-3495(94)80471-0.
[29] R.J. Clarke, Electric field sensitive dyes, in: A.P. Demckenko (Ed.), Advanced Fluorescence Reporters in Chemistry and Biology I: Fundamentals and Molecular Design, Springer, Berlin Heidelberg, 2010, pp. 331–344.
[30] L. Wang, Measurements and implications of the membrane dipole potential, Annu. Rev. Biochem. 81 (2012) 615–635, https://doi.org/10.1146/annurev-biochem-070110-123033.
[31] P. Sarkar, A. Chattopadhyay, Membrane dipole potential: an emergent approach to explore membrane organization and function, J. Phys. Chem. B 126 (2022) 4415–4430, https://doi.org/10.1021/acs.jpcb.2c02476.
[32] B. Lev, I. Vorobyov, R.J. Clarke, T.W. Allen, The membrane dipole potential and the roles of interface water and lipid hydrocarbon chains, J. Phys. Chem. B 128 (2024) 9482–9499, https://doi.org/10.1021/acs.jpcb.4c04469.
[33] C. Brosseau, E. Sabri, Resistor-capacitor modeling of cell membrane: a multiphysics analysis, J. Appl. Phys. 129 (2021) 011101, https://doi.org/10.1063/5.0033608.
[34] D. Halliday, J. Walker, R. Resnick, Fundamentals of Physics Extended, 10th ed., John Wiley & Sons, Hoboken, USA, 2024.

[35] D.A. McQuarrie, Statistical Mechanics, Harper-Collins, New York, 1976. Chap. 15.
[36] P. Debye, E. Hückel, Zur Theorie der Elektrolyte, Physik Z 24 (1923) 185–206.
[37] E. Racker, Structure and function of ATP-driven ion pumps, Trends in Biochemical Sciences 1 (1976) 244–247.
[38] A.-S. Feiner, A.J. McEvoy, The Nernst equation, J. Chem. Educ. 71 (1994) 493–494, https://doi.org/10.1021/ed071p493.
[39] S.G. Spangler, Expansion of the constant field equation to include both divalent and monovalent ions, Alabama J. Med. Sci. 9 (1972) 218–223. PMID: 5045041.
[40] D.E. Goldman, Potential, impedance, and rectification in membranes, J. Gen. Physiol. 27 (1943) 37–60, https://doi.org/10.1085/jgp.27.1.37.
[41] A.L. Hodgkin, B. Katz, The effect of sodium ions on the electrical activity of giant axon of the squid, J. Physiol. 108 (1949) 37–77, https://doi.org/10.1113/jphysiol.1949.sp004310.
[42] G. Stuart, N. Spruston, B. Sakmann, M. Häusser, Action potential initiation and backpropagation in neurons of the mammalian CNS, Trends Neurosci. 20 (1997) 125–131, https://doi.org/10.1016/s0166-2236(96)10075-8.
[43] B.P. Bean, The action potential in mammalian central neurons, Nat. Rev. Neurosci. 8 (2007) 451–465, https://doi.org/10.1038/nrn2148.
[44] G. Stuart, J. Schiller, B. Sackmann, Action potential initiation and propagation in rat neocortial pyramidal neurons, J. Physiol. 505 (3) (1997) 617–632.
[45] Y.A. Hao, S. Lee, R.H. Roth, S. Natale, L. Gomez, J. Taxidis, P.S. O'Neill, V. Villette, J. Bradley, Z. Wang, D. Jiang, G. Zhang, M. Sheng, D. Lu, E. Boyden, I. Delvendahl, P. Golshani, M. Wernig, D.E. Feldman, N. Ji, J. Ding, T.C. Südhof, T.R. Clandinin, M.Z. Lin, A fast and responsive voltage indicator with enhanced sensitivity for unitary synaptic events, Neuron 112 (2024) 3680–3696, https://doi.org/10.1016/j.neuron.2024.08.019.
[46] B.H. Lee, P. Park, X. Wu, J.D. Wong-Campos, J. Xu, M. Xiong, Y. Qi, Y-C. Huang, D.G. Itkis, S.E. Plutkis, L.D. Lavis, A.E. Cohen, Fast dendritic excitations primarily mediate back-propagation in CA1 pyramidal neurons during behavior, bioRxiv preprint (2026) doi: https://doi.org/10.64898/2026.01.03.696606.
[47] A. Varró, J. Tomek, N. Nagy, L. László, E. Passini, B. Rodriguez, I. Baczkó, Cardiac transmembrane ion channels and action potentials: cellular physiology and arrhythmogenic behavior, Physiol. Rev. 101 (2021) 1083–1176, https://doi.org/10.1152/physrev.00024.2019.
[48] Jana Vasković, Action potential: definition, steps, phases | Kenhub. https://www.kenhub.com, 2023.
[49] A. Mukherjee, Y. Huang, J. Elgeti, S. Oh, J.G. Abreu, L. Ammar, A.R. Neliat, J. Schüttler, D-D. Su, C. Dupre, N.C. Benites, X. Liu, L. Peshkin, M. Barboiu, H. Stocker, M.W. Kirschner, M. Basan, Membrane potential mediates the cellular response to mechanical pressure, Cell 189 (2026) 143–160, https://doi.org/10.1016/j.cell.2025.11.004.
[50] L.A. Kadir, M. Stacey, R. Barrett-Jolley, Emerging roles of the membrane potential: action beyond the action potential, Front. Physiol. 9 (2018) 1661, https://doi.org/10.3389/fphys.2018.01661.
[51] M. Yang, W.J. Brackenbury, Membrane potential and cancer progression, Front. Physiol. 4 (2013) 185, https://doi.org/10.3389/fphys.2013.00185.
[52] L. Kaestner, X. Wang, L. Hertz, I. Bernhardt, Voltage-activated ion channels in non-excitable cells – a viewpoint regarding their physiological justification, Front. Physiol. 9 (2018) 450, https://doi.org/10.3389/fphys.2018.00450.
[53] E. Sempou, V. Kostiuk, J. Zhu, M.C. Guerra, L. Tyan, W. Hwang, E. Camacho-Aguilar, M.J. Caplan, D. Zenisek, A. Warmflash, N.D.L. Owens, M.K. Khokha, Membrane potential drives the exit from pluripotency and cell fate commitment via calcium and mTOR, Nat. Comm. 13 (2022) 6681, https://doi.org/10.1038/s41467-022-34363-w.
[54] S. Sundelacruz, M. Levin, D.L. Kaplan, Role of membrane potential in the regulation of cell proliferation and differentiation, Stem Cell Rev. Rep. 5 (2009) 231–246, https://doi.org/10.1007/s12015-009-9080-2.
[55] S. Chifflet, J.A. Hernández, S. Grasso, A possible role for membrane depolarization in epithelial wound healing, Am. J. Cell Physiol. 288 (2005) C1420–C1430, https://doi.org/10.1152/ajpcell.00259.2004.
[56] J.R. Lazzari-Dean, A.M.M. Gest, E.W. Miller, Measuring absolute membrane potential across space and time, Annu. Rev. Biophys. 50 (2021) 447–468, https://doi.org/10.1146/annurev-biophys-062920-063555.
[57] D. Lovisolo, Patch clamp: the first four decades of a technique that revolutionized electrophysiology and beyond, Rev. Physiol. Biochem. Pharmacol. 186 (2023) 1–28, https://doi.org/10.1007/112_2022_71.
[58] A. Noguchi, Y. Ikegaya, N. Matsumoto, *In vivo* whole-cell patch-clamp methods: recent technical progress and future perspectives, Sensors 21 (2021) e1448, https://doi.org/10.3390/s21041448.
[59] B. Sakmann, E. Neher, Patch clamp techniques for studying ionic channels in excitable cells, Annu. Rev. Physiol. 46 (1984) 455–472, https://doi.org/10.1146/annurev.ph.46.030184.002323.
[60] O.P. Hamill, A. Marty, E. Neher, B. Sakmann, F.J. Sigworth, Improved patch-clamp technique for high-resolution current recoding from cells and cell-free membrane patches, Pflugers Arch 391 (1981) 85–100, https://doi.org/10.1007/BF00656997.
[61] B.G. Kornreich, The patch clamp technique: principles and technical considerations, J. Vet. Cardiol. 9 (2007) 25–37, https://doi.org/10.1016/j.jvc.2007.02.001.
[62] E. Neher, B. Sakmann, Single channel currents recorded from membrane of denervated frog muscle fibers, Nature 260 (1976) 799–802, https://doi.org/10.1038/260799a0.
[63] M.R. Ghovanloo, S. Tyagi, P. Zhao, E. Kiziltug, M. Estacion, S.D. Dip-Hajj, S. G. Waxman, High-throughput combined voltage-clamp/current-clamp analysis of freshly isolated neurons, Cell Rep. Methods 3 (2023) e100385, https://doi.org/10.1016/j.crmeth.2022.100385.
[64] S. Stoelzle, A. Obergrussberger, A. Brüggemann, C. Haarmann, M. George, R. Kettenhofen, N. Fertig, State-of-the-art automated patch clamp devices: heat activation, action potentials, and high throughput in ion channel screening, Front. Pharmacol. 2 (2011) 76, https://doi.org/10.3389/fphar.2011.00076.
[65] E. Nagaecva, I. Zubarev, E.R. Korpi, Electrophysiological properties of neurons: current-clamp recordings in mouse brain slices and firing-pattern analysis, Bio-Protocol 11 (2021) e4061, https://doi.org/10.21769/BioProtoc.4061.
[66] M.E. Spira, A. Hai, Multi-electrode array technologies for neuroscience and cardiology, Nature Nanotechnology 8 (2013) 83–94, https://doi.org/10.1038/nnano.2012.265.
[67] J. Miller, M. Ballini, P. Livi, Y. Chen, M. Radivojevic, A. Shadmani, V. Viswam, I. L. Jones, M. Fiscella, R. Diggelmann, A. Stettler, U. Frey, D.J. Bakkum, A. Hierlermann, High-resolution CMOS MEA platform to study neurons at subcellular, cellular, and network levels, Lab Chip 15 (2015) 2767–2780, https://doi.org/10.1039/c5lc00133a.
[68] M. Dipalo, H. Amin, L. Lovato, F. Moia, V. Caprettini, G.C. Messina, F. Tantussi, L. Berdondini, F. De Angelis, Intracellular and extracellular recording of spontaneous action potentials in mammalian neurons and cardiac cells with 3D plasmonic nanoelectrodes, Nano Lett. 17 (2017) 3932–3939, https://doi.org/10.1021/acs.nanolett.7b01523.
[69] M. Dipalo, S.K. Rastogi, L. Matino, R. Garg, J. Bliley, G. Iachetta, G. Melle, R. Shrestha, S. Shen, F. Santoro, A.W. Feinberg, A. Barbaglia, T. Cohen-Karni, F. De Angelis, Intracellular action potential recordings from cardiomyocytes by ultrafast pulsed laser irradiation of fuzzy graphene microelectrodes, Sci. Adv. 7 (2021) eabd5175, https://doi.org/10.1126/sciadv.abd5175.
[70] X. Xu, Z. Liu, J. Liu, C. Yao, X. Chen, X. Huang, S. Huang, P. Shi, M. Li, L. Wang, Y. Tao, H. Chen, X. Xie, Multi-sized microelectrode array coupled with micro-electroporation for effective recording of intracellular action potential, Microsystems & Nanoengineering 11 (2025) 85, https://doi.org/10.1038/s41378-025-00887-6.
[71] D.D. Stupin, E.A. Kuzina, A.A. Abelit, A.K. Emelyanov, D.M. Nikolaev, M. N. Ryazantsev, S.V. Koniakhin, M.V. Dubina, Bioimpedance spectroscopy: basics and applications, ACS Biomater. Sci. Eng. 7 (2021) 1962–1986, https://doi.org/10.1021/acsbiomaterials.0c01570.
[72] Y. Xu, X. Xie, Y. Duan, L. Wang, Z. Cheng, J. Cheng, A review of impedance measurements of whole cells, Biosens. Bioelectron. 77 (2016) 824–836, https://doi.org/10.1016/j.bios.2015.10.027.
[73] D.D. Stupin, E.A. Kuzina, A.A. Abelit, A.K. Emelyanov, D.M. Nikolaev, M. N. Ryazantsev, S.V. Koniakhin, M.V. Dubina, Bioimpedance spectroscopy: basics and applications, ACS Biomater. Sci. Eng. 7 (2021) 1962–1986, https://doi.org/10.1021/acsbiomaterials.0c01570.
[74] C. Bot, C. Prodan, Probing the membrane potential of living cells by dielectric spectroscopy, Eur. Biophys. J. 38 (2009) 1049–1059, https://doi.org/10.1007/s00249-009-0507-0.
[75] E. Gheorghiu, The dielectric behavior of suspensions of spherical cells: a unitary approach, J. Phys. A: Math. Gen. 27 (1994) 3883–3893, https://doi.org/10.1088/0305-4470/27/11/035.
[76] D. Ng, P. Fromherz, Genetic targeting of a voltage-sensitive dye by enzymatic activation of phosphonooxymethyl-ammonium derivative, ACS Chem. Biol. 6 (2011) 444–451, https://doi.org/10.1021/cb100312d.
[77] A.S. Waggoner, Dye indicators of membrane potential, Annu. Rev. Biophys. Bioeng. 8 (1979) 47–68, https://doi.org/10.1146/annurev.bb.08.060179.000403.
[78] S. Chemla, F. Chavane, Voltage-sensitive dye imaging: technique review and models, J. Physiol. – Paris 104 (2010) 40–50, https://doi.org/10.1016/j.jphysparis.2009.11.009.
[79] T.W. Cacciatore, P.D. Brodfuehrer, J.E. González, T. Jiang, S.R. Adams, R. Y. Tsien, W.B. Kristan Jr., D. Kleinfeld, Identification of neural circuits by imaging coherent electrical activity with FRET-based dyes, Neuron 23 (1999) 449–459, https://doi.org/10.1016/s0896-6273(00)80799-0.
[80] J.D. Marshall, M.J. Schnitzer, Optical strategies for sensing neuronal voltage using quantum dots and other semiconductor nanocrystals, ACS Nano 7 (2013) 4601–4609, https://doi.org/10.1021/nn401410k.
[81] T.A. Haider, T. Knöpfel, Voltage-sensitive fluorescent proteins for optical electrophysiology, in: L. Guo (Ed.), Neural Interface Engineering, Springer Nature Switzerland AG, 2000, pp. 383–407.
[82] I. Mollinedo-Gajate, C. Song, T. Knöpfel, Genetically encoded voltage indicators, Adv. Exp. Med. Biol. 1293 (2021) 209–224, https://doi.org/10.1007/978-981-15-8763-4_12.
[83] Y. Murata, H. Iwasaki, M. Sasaki, K. Inaba, Y. Okamura, Phosphoinositide phosphatase activity coupled to an intrinsic voltage sensor, Nature 435 (2005), https://doi.org/10.1038/nature03650, 1293-1243.
[84] M.S. Siegel, E.Y. Isacoff, A genetically encoded optical probe of membrane voltage, Neuron 19 (1997) 735–741, https://doi.org/10.1016/S0896-6273(00)80955-1.
[85] K. Ataka, V.A. Pieribone, A genetically targetable fluorescent probe of channel gating with rapid kinetics, Biophys. J. 82 (2002) 509–516, https://doi.org/10.1016/S0006-3495(02)75415-5.
[86] B.E. Kang, B.J. Baker, Pado, a fluorescent protein with proton channel activity can optically monitor membrane potential, intracellular pH, and map gap junctions, Sci. Rep. 6 (2016) 23865, https://doi.org/10.1038/srep23865.
[87] J.M. Kralj, A.D. Douglass, D.R. Hochbaum, D. Maclaurin, A.E. Cohen, Optical recording of action potentials in mammalian neurons using a microbial rhodopsin, Nat. Methods 9 (2011) 90–95, https://doi.org/10.1038/nmeth.1782.

[88] Y. Gong, M.J. Wagner, J.Z. Li, M.J. Schnitzer, Imaging neural spiking in brain tissue using FRET-opsin protein voltage sensors, Nat. Comm. 5 (2014) 3674, https://doi.org/10.1038/ncomms4674.
[89] A.S. Abdelfattah, T. Kawashima, A. Singh, O. Novak, H. Liu, Y. Shuai, Y.-C. Huang, L. Campagnola, S.C. Seeman, J. Yu, J. Zheng, J.B. Grimm, R. Patel, J. Friedrich, B.D. Mensh, L. Paninski, J.J. Macklin, G.J. Murphy, K. Podgorski, B.-J. Lin, T.-W. Chen, G.C. Turner, Z. Liu, M. Koyama, K. Svoboda, M.B. Ahrens, L. D. Lavis, E.R. Schreiter, Bright and photostable chemigenetic indicators of extended *in vivo* voltage imaging, Science 365 (2019) 699–704, https://doi.org/10.1126/science.aav6416.
[90] J. Plášek, K. Sigler, Slow fluorescent indicators of membrane potential: a survey of different approaches to probe response analysis, J. Photochem. Photobiol. B: Biol. 33 (1996) 101–124, https://doi.org/10.1016/1011-1344(96)07283-1.
[91] L.M. Loew, G.W. Bonneville, J. Surow, Charge shift optical probes of membrane potential. Theory, Biochem 17 (1978) 4065–4071, https://doi.org/10.1021/bi00612a030.
[92] B. Kuhn, P. Fromherz, Anellated hemicyanine dyes in a neuron membrane: molecular Stark effect and optical voltage recording, J. Phys. Chem. B 107 (2003) 7903–7913, https://doi.org/10.1021/jp0345811.
[93] D. Roy, Z. Shapira, S. Weiss, Membrane potential sensing: material design and method development for single particle optical electrophysiology, J. Chem. Phys. 156 (2022) 084201, https://doi.org/10.1063/5.0076522.
[94] C. Reichardt, T. Welton, Solvents and Solvent Effects in Organic Chemistry, Wiley-VCH, Weinheim, 2011.
[95] E. Fluhler, V.G. Burnham, L.M. Loew, Spectra, membrane binding, and potentiometric responses of new charge shift probes, Biochemistry 24 (1985) 5749–5755, https://doi.org/10.1021/bi00342a010.
[96] L.M. Loew, Potentiometric dyes: imaging electrical activity of cell membranes, Pure & Appl. Chem. 68 (1996) 1405–1409, https://doi.org/10.1351/pac199668071405.
[97] B. Valeur, B. Santos, M. Nuno, Molecular Fluorescence. Principles and Applications, Wiley-VCH, Weinheim, Germany, 2013.
[98] P. Zirak, A. Penzkofer, T. Mathes, P. Hegemann, Photo-dynamics of roseoflavin and riboflavin in aqueous and organic solvents, Chem. Phys. 358 (2009) 111–122, https://doi.org/10.1016/j.chemphys.2008.12.026.
[99] R. Misra, S.P. Bhattacharyya, Intramolecular Charge Transfer: Theory and Applications, Wiley-VCH-Verlag, Weinheim, 2018.
[100] B. Kuhn, C.J. Roome, Primer to voltage imaging with ANNINE dyes and two-photon microscopy, Front. Cell. Neurosci. 13 (2019) 321, https://doi.org/10.3389/fncel.2019.00321.
[101] U. Resch-Genger, M. Grabolle, S. Cavaliere-Jaricot, R. Nitschke, Quantum dots versus organic dyes as fluorescent labels, Nat. Methods 5 (2008) 763–775, https://doi.org/10.1038/nmeth.1248.
[102] N. Hildebrandt, C.M. Spillmann, R. Algar, T. Pons, M.H. Stewart, E. Oh, K. Susumu, S.A. Díaz, J.B. Delehanty, I.L. Medintz, Energy transfer with semiconductor quantum dot bioconjugates: a versatile platform for biosensing, energy harvesting, and other developing applications, Chem. Rev. 117 (2017) 536–711, https://doi.org/10.1021/acs.chemrev.6b00030.
[103] K-W. Park, Z. Deutsch, J. Li, D. Oron, S. Weiss, Single molecule quantum-confined Stark effect measurements of semiconductor nanoparticles at room temperature, ACS Nano 6 (2012) 10013–10023, https://doi.org/10.1021/nn303719m.
[104] Y. Kuo, J. Li, X. Michalet, A. Chizhik, N. Meir, O. Bar-Elli, E. Chan, D. Oron, J. Enderlein, S. Weiss, Characterizing the quantum-confined Stark effect in semiconductor quantum dots and nanorods for single molecule electrophysiology, ACS Photonics 5 (2018) 4788–4800, https://doi.org/10.1021/acsphotonics.8b00617.
[105] K. Park, Y. Kuo, V. Shvadchak, A. Ingargiola, X. Dai, L. Hsiung, W. Kim, H. Zhou, P. Zou, A.J. Levine, J. Li, S. Weiss, Membrane insertion of – and membrane potential sensing by – semiconductor voltage nanosensors: feasibility demonstration, Sci. Adv. 4 (2018) e1601453, https://doi.org/10.1126/sciadv.1601453.
[106] A. Ludwig, P. Serna, L. Morgenstein, G. Yang, O. Bar-Elli, G. Ortiz, E.W. Miller, D. Oron, A. Grupi, S. Weiss, A. Triller, Development of lipid-coated semiconductor nanosensors for recording of membrane potential in neurons, ACS Photonics 7 (2020) 1141–1152, https://doi.org/10.1021/acsphotonics.9b01558.
[107] O.K. Nag, M.E. Muroski, D.A. Hastman, B. Almeida, I.L. Medintz, A.L. Huston, J. B. Delehanty, Nanoparticle-mediated visualization and control of cellular membrane potential: strategies, progress, and remaining issues, ACS Nano 14 (2020) 2659–2677, https://doi.org/10.1021/acsnano.9b10163.
[108] A.L. Efros, J.B. Delehanty, A.L. Huston, I.L. Medintz, M. Barbic, T.D. Harris, Evaluating the potential of using quantum dots for monitoring electrical signals in neurons, Nat. Nanotechnol. 13 (2018) 278–288, https://doi.org/10.1038/s41565-018-0107-1.
[109] Th. Förster, Fluoreszenz organischer Verbindungen, Vandenhoeck und Rupprecht, Göttingen, Germany, 1951.
[110] R.A. Marcus, On the theory of oxidation-reduction reactions involving electron transfer. I, J. Chem. Phys. 24 (1956) 966–978, https://doi.org/10.1063/1.1742723.
[111] N.S. Hush, Adiabatic theory of outer sphere electron-transfer reactions in solution, Trans. Farad. Soc. 57 (1961) 557–580, https://doi.org/10.1039/TF9615700557.
[112] R.A. Marcus, N. Sutin, Electron transfer in chemistry and biology, Biochim. Biophys. Acta 811 (1985) 265–322, https://doi.org/10.1016/0304-4173(85)90014-X.
[113] A.P. Demchenko, Proton transfer reactions: from photochemistry to biochemistry and bioenergetics, BBA Adv. 3 (2023) 100085, https://doi.org/10.1016/j.bbadva.2023.100085.
[114] L.M. Oltrogge, Q. Wang, S.G. Boxer, Ground-state proton transfer kinetics in green fluorescent protein, Biochemistry 53 (2014) 5947–5957, https://doi.org/10.1021/bi500147n.
[115] J.E. González, R.Y. Tsien, Voltage sensing by fluorescence resonance energy transfer in single cells, Biophys. J. 69 (1995) 1272–1280, https://doi.org/10.1016/S0006-3495(95)80029-9.
[116] J.E. González, R.Y. Tsien, Improved indicators of cell membrane potential that use fluorescence resonance energy transfer, Chem. Biol. 4 (1997) 269–277, https://doi.org/10.1016/s1074-5521(97)90070-3.
[117] B. Chanda, R. Blunck, L.C. Faria, F.E. Schweizer, I. Mody, F. Bzanilla, A hybrid approach to measuring electrical activity in genetically specified neurons, Nat. Neurosci. 8 (2005) 1619–1626, https://doi.org/10.1038/nn1558.
[118] E.W. Miller, Small molecule fluorescent voltage indicators for studying membrane potential, Curr. Opin. Chem. Biol. 33 (2016) 74–80, https://doi.org/10.1016/j.cbpa.2016.06.003.
[119] A. Khadria, Tools to measure membrane potential of neurons, Biomed. J. 45 (2022) 749–762, https://doi.org/10.1016/j.bj.2022.05.007.
[120] R. Fleming, Chemical Applications of Ultrafast Spectroscopy, Oxford University Press, New York, 1986.
[121] J. Shirdel, A. Penzkofer, R. Procházka, Z. Shen, J. Daub, Absorption and fluorescence spectroscopic characterization of a phenothiazine-flavin dyad, Chem. Phys. 336 (2007) 1–13, https://doi.org/10.1016/j.chemphys.2007.05.002.
[122] J. Liu, R. Zhang, C. Shang, Y. Zhang, Y. Feng, L. Pan, B. Xu, T. Hyeon, W. Bu, J. Shi, J. Du, Near-infrared voltage nanosensors enable real-time imaging of neuronal activities in mice and zebrafish, J. Am. Chem. Soc. 142 (2020) 7858–7867, https://doi.org/10.1021/jacs.0c01025.
[123] S.E. Ochmann, H. Joshi, E. Büber, H.G. Franquelim, P. Stegemann, B. Saccà, U. F. Keyser, A. Aksimentiev, P. Tinnefeld, DNA origami voltage sensors for transmembrane potentials with single-molecule sensitivity, Nano Lett. 21 (2021) 8634–8641, https://doi.org/10.1021/acs.nanolett.1c02584.
[124] P. Zou, Y. Zhao, A.D. Douglass, D.R. Hochbaum, D. Brinks, C.A. Werley, D. J. Harrison, R.E. Campbell, A.E. Cohen, Bright and fast multicoloured voltage reporters via electrochromic FRET, Nat. Comm. 5 (2014) 4625, https://doi.org/10.1038/ncomms5625.
[125] R. Sakai, V. Repunte-Canonigo, C.D. Raj, T. Knöpfel, Design and characterization of a DNA-encoded, voltage-sensitive fluorescent protein, Eur. J. Neurosci. 13 (2001) 2314–2318.
[126] T. Knöpfel, K. Tomita, R. Shimazaki, R. Sakai, Optical recordings of membrane potential using genetically targeted voltage-sensitive fluorescent proteins, Methods 30 (2003) 42–48, https://doi.org/10.1016/S1046-2023(03)00006-9.
[127] A.M. Kuznetsov, J. Ulstrup, Electron Transfer in Chemistry and Biology: An Introduction to the Theory, Wiley, New York, 1999.
[128] V. Balzani, Electron Transfer in Chemistry, Wiley-VCH, Weinheim, 2001.
[129] B. Röder, Einführung in die molekulare Photobiophysik, B. G. Teubner, Stuttgart, Leipzig, 1999, pp. 92–115.
[130] Y. Hou, X. Zhang, K. Chen, D. Liu, Z. Wang, Q. Liu, J. Zhao, A. Barbon, Charge separation, charge recombination, long-lived charge transfer state formation and intersystem crossing in organic electron donor/acceptor dyads, J. Mater. Chem. C 7 (2019) 12048–12074, https://doi.org/10.1039/C9TC04285G.
[131] R.A. Marcus, Chemical and electrochemical electron-transfer theory, Annu. Rev. Phys. Chem. 15 (1964) 155–196, https://doi.org/10.1146/annurev.pc.15.100164.0801103.
[132] R.A. Marcus, Elektronentransferreaktionen in der Chemie -Theorie und Experiment, Angew. Chem. 105 (1993) 1161–1172, https://doi.org/10.1002/anie.199311113.
[133] J. Jortner, Temperature dependent activation energy for electron transfer between biological molecules, J. Chem. Phys. 64 (1976) 4860–4867, https://doi.org/10.1063/1.432142.
[134] J. Hopfield, Electron transfer between biological molecules by thermally activated tunneling, Proc. Natl. Acad. Sci. U.S.A. 71 (1974) 3640–3644, https://doi.org/10.1073/pnas.71.9.3640.
[135] C.C. Moser, J.M. Keske, K. Warncke, R.S. Farid, P.L. Dutton, Nature of biological electron transfer, Nature 355 (1992) 796–802, https://doi.org/10.1038/355796a0.
[136] K.J. Laidler, The development of the Arrhenius equation, J. Chem. Edu. 61 (1984) 494–498, https://doi.org/10.1021/ed061p494.
[137] M.G. Evans, M. Polanyi, Some applications of the transition state method to the calculation of reaction velocities, especially in solution, Trans. Faraday Soc. 31 (1935) 875–894, https://doi.org/10.1039/TF9353100875.
[138] H. Eyring, The activated complex in chemical reactions, J. Chem. Phys. 3 (1935) 107–115, https://doi.org/10.1063/1.1749604.
[139] N.J. Turro, V. Ramamurthy, J.C. Scaiano, Principles of Molecular Photochemistry. An Introduction, University Science Books, Sausalito, California, 2009.
[140] M. Natali, S. Campagna, F. Scandola, Photoinduced electron transfer across molecular bridges: electron- and hole-transfer superexchange pathways, Chem. Soc. Rev. 43 (2014) 4005–4018, https://doi.org/10.1039/c3cs60463b.
[141] J. Sukegawa, C. Schubert, X. Zhu, H. Tsuji, D.M. Guldi, E. Nakamura, Electron transfer through rigid organic molecular wires enhanced by electronic and electron-vibration coupling, Nat. Chem. 6 (2014) 899–905, https://doi.org/10.1038/nchem.2026.
[142] E.W. Miller, J.Y. Lin, E.P. Frady, P.A. Steinbach, W.B. Kristan Jr., R.Y. Tsien, Optically monitoring voltage in neurons by photo-induced electron transfer

through molecular wires, Proc. Natl. Acad. Sci. U.S.A. 109 (2012) 2114–2119, https://doi.org/10.1073/pnas.1120694109.
[143] K. Seno, T. Ishioka, A. Harata, Y. Hatano, Photoionization of rhodamine dyes adsorbed at the aqueous solution surfaces investigated by synchrotron radiation, Analyt. Sci. 17 (2001) i1177–i1179, https://doi.org/10.14891/analscisp.17icas.0.i1177.0.
[144] Y. Matsumura, K. Iida, H. Sato, Theoretical study on the ionization of aniline in aqueous solutions, Chem. Phys. Lett. 584 (2013) 103–107, https://doi.org/10.1016/j.cplett.2013.08.081.
[145] D. Devault, Quantum mechanical tunnelling in biological systems, Q. Rev. Biophys. 13 (1980) 387–564, https://doi.org/10.1017/s003358350000175x.
[146] A.S. Klymchenko, Fluorescent probe for lipid membranes: from the cell surface to organelles, Acc. Chem. Res. 56 (2023) 1–12, https://doi.org/10.1021/acs.accounts.2c00586.
[147] G. Ortiz, P. Liu, S.H.H. Naing, V.R. Muller, E.W. Miller, Synthesis of sulfonated carbofluoresceins for voltage imaging, J. Am. Chem. Soc. 141 (2019) 6631–6638, https://doi.org/10.1021/jacs.9b01261.
[148] C.R. Woodford, E.P. Frady, R.S. Smith, B. Morey, G. Canzi, S.F. Palida, R. C. Araneda, W.B. Kristan Jr., C.P. Kubiak, E.W. Miller, R.Y. Tsien, Improved PeT molecules for optically sensing voltage in neurons, J. Am. Chem. Soc. 137 (2015) 1817–1824, https://doi.org/10.1021/ja510602z.
[149] S.C. Boggess, S.S. Gandhi, B.A. Siemons, N. Huebsch, K.E. Healy, E.W. Miller, New molecular scaffolds for fluorescent voltage indicators, ACS Chem. Biol. 14 (2019) 390–396, https://doi.org/10.1021/acschembio.8b00978.
[150] V. Grenier, B.R. Daws, P. Liu, E.W. Miller, Spying on neuronal membrane potential with genetically targetable voltage indicators, J. Am. Chem. Soc. 141 (2019) 1349–1358, https://doi.org/10.1021/jacs.8b11997.
[151] P.E. Deal, P. Liu, S.H. Al-Abdullatif, V.R. Muller, K. Shamardani, H. Adesnik, E. W. Miller, Covalently tethered rhodamine voltage reporters for high-speed functional imaging in brain tissue, J. Am. Chem. Soc. 142 (2019) 614–622, https://doi.org/10.1021/jacs.9b12265.
[152] P. Liu, V. Grenier, W. Hong, V.R. Muller, E.W. Miller, Fluorogenic targeting of voltage-sensitive dyes to neurons, J. Am. Chem. Soc. 139 (2017) 17334–17340, https://doi.org/10.1021/jacs.7b07047.
[153] A.S. Klymchenko, H. Stoeckel, T. Takeda, Y. Mély, Fluorescent probe based on intramolecular proton transfer for fast ratiometric measurement of cellular transmembrane potential, J. Phys. Chem. B 110 (2006) 13624–13632, https://doi.org/10.1021/jp062385z.
[154] G.P. Patterson, S.M. Knobel, W.D. Sharif, S.R. Kain, D.W. Piston, Use of the green fluorescent protein and its mutants in quantitative fluorescence microscopy, Biophys. J. 73 (1997) 2782–2790, https://doi.org/10.1016/S0006-3495(97)78307-3.
[155] R. Takeda, E. Tsutsumi, K. Okatsu, S. Fukai, K. Takeda, Structural characterization of green fluorescent protein in the I-state, Scientific Reports 14 (2024) 22832, https://doi.org/10.1038/s41598-024-a73696-y.
[156] T. Nakabayashi, M. Kinjo, N. Ohta, Electric field effects on fluorescence of the green fluorescent protein, Chem. Phys. Lett. 457 (2008) 408–412, https://doi.org/10.1016/j.cplett.2008.04.018.
[157] Y. Yang, S. Fan, J.A. Webb, Y. Ma, J. Guyette, X. Chen, K. Gaus, R.D. Tilley, J. J. Gooding, Electrochemical fluorescence switching of enhanced green fluorescent protein, Biosens. Bioelectron. 237 (2023) 115467, https://doi.org/10.1016/j.bios.2023.115467.
[158] J.M. Kralj, D.R. Hochbaum, A.D. Douglass, A.E. Adam, Electrical spiking in *Escherichia coli* probed with a fluorescent voltage-indicating protein, Science 333 (2011) 345–348, https://doi.org/10.1126/science.1204763.
[159] A. Silapetere, S. Hwang, Y. Hontani, R.G.F. Lahore, J. Balke, F.V. Escobar, M. Tros, P.E. Konold, R. Matis, R. Croce, P.J. Walla, P. Hildebrandt, U. Alexiev, J. T.M. Kennis, H. Sun, T. Utesch, P. Hegemann, QuasAr odyssey: the origin of fluorescence and its voltage sensitivity in microbial rhodopsins, Nat. Comm. 13 (2022) 5501, https://doi.org/10.1038/s41467-022-33084-4.
[160] X.M. Zhang, T. Yokoyama, M. Sakamoto, Imaging voltage with microbial rhodopsin, Front. Mol. Biosci. 8 (2021) 738829, https://doi.org/10.3389/fmolb.2021.738829.
[161] A.S. Abdelfattah, R. Valenti, J. Zheng, A. Wong, GENI Project Team, K. Podgorski, M. Koyama, D.S. Kim, E.R. Schreiter, A general approach to engineer positive-going eFRET voltage indicators, Nat. Comm. 11 (2020) 3444, https://doi.org/10.1038/s41467-020-17322-1.
[162] A. Penzkofer, M. Luck, T. Mathes, P. Hegemann, Bistable retinal Schiff base photodynamics of histidine kinase rhodopsin HKR1 from *Chlamydomonas reinhardtii*, Photochem. Photobiol. 90 (2014) 773–785, https://doi.org/10.1111/php.12246.
[163] A. Penzkofer, A. Silapetere, P. Hegemann, Absorption and emission spectroscopic investigation of the thermal dynamics of the Archaerhodopsin 3 based fluorescent voltage sensor QuasAr1, Int. J. Mol. Sci. 20 (2019) 4086, https://doi.org/10.3390/ijms20174086.
[164] J. Huang, X. Pan, N. Yan, Structural biology and molecular pharmacology of voltage-gated ion channels, Nat. Rev. Mol. Cell Biol. 25 (2024) 904–925, https://doi.org/10.1038/s41580-024-00763-7.
[165] R. Hedrich, Ion channels in plants, Physiol. Rev. 92 (2012) 1777–1811, https://doi.org/10.1152/physrev.00038.2011.
[166] Y. Saimi, S.H. Loukin, X.-L. Zhou, B. Martinac, C. Kung, Ion channels in microbes, Methods Enzymol. 294 (1999) 507–524, https://doi.org/10.1016/s0076-6879(99)94030-2.
[167] P. Rühl, A.G. Nair, N. Gawande, S.N.C.W. Dehiwalage, L. Münster, R. Schönherr, S.H. Heinemann, An ultrasensitive genetically encoded voltage indicator uncovers the electrical activity of non-excitable cells, Adv. Sci. 11 (2024) 2307938, https://doi.org/10.1002/advs.202307938.
[168] F. Bezanilla, Gating currents, J. Gen. Physiol. 150 (2018) 911–932, https://doi.org/10.1085/jgp.201812090.
[169] W.A. Catterall, Ion channel voltage sensors: structure, function, and pathophysiology, Neuron 67 (2010), https://doi.org/10.1016/j.neuron.2010.08.021, 915-298.
[170] R. Shen, Y. Men, B. Roux, E. Perozo, Mechanism of voltage gating in the voltage-sensing phosphatase Ci-VSP, Proc. Natl. Acad. Sci. U.S.A. 119 (2022) e2206649119, https://doi.org/10.1073/pnas.2206649119.
[171] C.A. Villalba-Galea, New insights in the activity of voltage sensitive phosphatases, Cell. Sign. 24 (2012) 1541–1547, https://doi.org/10.1016/j.cellsig.2012.03.013.
[172] S.C. Guo, R. Shen, B. Roux, A.R. Dinner, Dynamics of activation in the voltage-sensing domain of *Ciona intestinalis* phosphatase Ci-VSP, Nat. Comm. 15 (2024) 1408, https://doi.org/10.1038/s41467-024-45514-6.
[173] Q. Li, S. Wanderling, M. Paduch, D. Medovoy, A. Singharoy, R. McGreevy, C. A. Villalba-Galea, R.E. Hulse, B. Roux, K. Schulten, A. Kossiakoff, E. Perozo, Structural mechanism of voltage dependent gating in an isolated voltage-sensing domain, Nat. Struct. Mol. Biol. 21 (2014) 244, https://doi.org/10.1038/nsmb.2768.
[174] B.J. Baker, L. Jin, Z. Han, L.B. Cohen, M. Popovic, J. Platisa, V. Pieribone, Genetically encoded fluorescent voltage sensors using the voltage-sensing domain of *Nematostella* and *Danio* phosphatases exhibit fast kinetics, J. Neurosci. Methods 208 (2012) 190–196, https://doi.org/10.1016/j.jneumeth.2012.05.016.
[175] Y. Okamura, A. Kawanave, T. Kawal, Voltage-sensing phosphatases: biophysics, physiology, and molecular engineering, Physiol. Rev. 98 (2018) 2097–2131, https://doi.org/10.1152/physrev.00056.2017.
[176] A. Lundby, H. Mutoh, D. Dimitrov, W. Akemann, T. Knöpfel, Engineering of a genetically encodable fluorescent voltage sensor exploiting fast Ci-VSP voltage sensing movements, PLoS One 3 (2008) e2514, https://doi.org/10.1371/journal.pone.0002514.
[177] E.E.L. Lee, F. Bezanilla, Biophysical characterization of genetically encoded voltage sensor ASAP1: dynamic range improvement, Biophys. J. 113 (2017) 2178–2181, https://doi.org/10.1016/j.bpj.2017.10.018.
[178] L. Barnett, J. Platisa, M. Popovic, V.A. Pieribone, A fluorescent, genetically-encoded voltage probe capable of resolving action potentials, PLoS One 7 (2012) e43454, https://doi.org/10.1371/journal.pone.0043454.
[179] W. Akemann, H. Mutoh, A. Perron, J. Rossier, T. Knöpfel, Imaging brain electric signals with genetically targeted voltage-sensitive fluorescent proteins, Nat. Methods 7 (2010) 643–649, https://doi.org/10.1038/nmeth.1479.
[180] L. Jin, Z. Han, J. Platisa, J.R.A. Wooltorton, L.B. Cohen, V.A. Pieribone, Single action potentials and subthreshold electrical events imaged in neurons with a fluorescent protein voltage probe, Neuron 75 (2012) 779–785, https://doi.org/10.1016/j.neuron.2012.06.040.
[181] H. Tsutsui, S. Karasawa, Y. Okamura, A. Miyawaki, Improving membrane voltage measurements using FRET with new fluorescent proteins, Nat. Methods 5 (2008) 683–685, https://doi.org/10.1038/nmeth.1235.
[182] V. Villette, M. Chavarha, I.K. Dimov, J. Bradley, L. Pradhan, B. Mathieu, S. W. Evans, S. Chamberland, D. Shi, R. Yang, B.B. Kim, A. Ayon, A. Jalil, F. St-Pierre, M.J. Schnitzer, G. Bi, K. Toth, J. Ding, S. Dieudonné, M.Z Lin, Ultrafast two-photon imaging of a high-gain voltage indicator in awake behaving mice, Cell 179 (2019) 1590–1608, https://doi.org/10.1016/j.cell.2019.11.004.
[183] Z. Liu, X. Lu, V. Villette, Y. Gou, K.L. Colbert, S. Lai, S. Guan, M.A. Land, J. Lee, T. Assefa, D.R. Zollinger, M.M. Korympidou, A.L. Vlasits, M.M. Pang, S. Su, C. Cai, E. Froudarakis, N. Zhou, S.S. Patel, C.L. Smith, A. Ayon, P. Bizouard, J. Bradley, K. Franke, T.R. Clandinin, A. Giovannucci, A.S. Tolias, J. Reimer, S. Dieudonné, F. St-Pierre, Sustained deep-tissue voltage recording using a fast indicator evolved for two-photon microscopy, Cell 185 (2022) 3408–3425, https://doi.org/10.1016/j.cell.2022.07.013.
[184] J. Platisa, X. Ye, A.M. Ahrens, C. Liu, I.A. Chen, I.G. Davison, L. Tian, V. A. Pieribone, J.L. Chen, High-speed low-light *in vivo* two-photon voltage imaging of large neuronal populations, Nat. Methods 20 (2023) 1095–1103, https://doi.org/10.1038/s41592-023-01820-3.
[185] S.W. Evans, D.Q. Shi, M. Chavarha, M.H. Plitt, J. Taxidis, B. Madruga, J.L. Fan, F. J. Hwang, S.C. van Keulen, C.M. Suomivuori, M.M. Pang, S. Su, S. Lee, Y.A. Hao, G. Zhang, D. Jiang, L. Pradhan, R.H. Roth, Y. Liu, C.C. Dorian, A.L. Reese, A. Negrean, A. Losonczy, C.D. Makinson, S. Wang, T.R. Clandinin, R.O. Dror, J. B. Ding, N. Ji, P. Golshani, L.M. Giocomo, G.Q. Bi, M.Z. Lin, A positively tuned voltage indicator for extended electrical recordings in the brain, Nat. Methods 20 (2023) 1104–1113, https://doi.org/10.1038/s41592-023-01913-z.
[186] Q. Yu, X. Wang, L. Nie, Optical recoding of brain functions based on voltage-sensitive dyes, Chin. Chem. Lett. 32 (2021) 1879–1887, https://doi.org/10.1016/j.cclet.2020.12.060.
[187] F. St-Pierre, J.D. Marshall, Y. Yang, Y. Gong, M.J. Schnitzer, M.Z. Lin, High-fidelity optical reporting of neuronal electrical activity with an ultrafast fluorescent voltage sensor, Nat. Neurosci. 17 (2014) 884–889, https://doi.org/10.1038/nn.3709.
[188] A. Perron, H. Mutoh, T. Launey, T. Knöpfel, Red-shifted voltage-sensitive fluorescent proteins, Chem. Biol. 16 (2009) 1268–1277, https://doi.org/10.1016/j.chembiol.2009.11.014.
[189] S.G. Gautam, A. Perron, H. Mutoh, T. Knöpfel, Exploration of fluorescent protein voltage probes based on circularly permuted fluorescent proteins, Front. Neuroeng. 2 (2009) 14, https://doi.org/10.3389/neuro.16.014.2009.
[190] A.I. Kostyuk, A.D. Demidovich, D.A. Kotova, V.V. Belousov, D.S. Bilant, Circularly permuted fluorescent protein-based indicators: history, principles, and

classification, Int. J. Mol. Sci. 20 (2019) 4200, https://doi.org/10.3390/ijms20174200.
[191] W. Liu, M. Deng, C. Yang, F. Liu, X. Guan, Y. Du, L. Wang, J. Chu, Genetically encoded single circularly permuted fluorescent protein-based intensity indicators, J. Phys. D: Appl. Phys. 53 (2020) 113001, https://doi.org/10.1088/1361-6463/ab5dd8.
[192] W.W. Ward, H.J. Prentice, A.F. Roth, C.W. Cody, S.C. Reeves, Spectral perturbations of the *Aequorea* green fluorescent protein, Photochem. Photobiol. 35 (1982) 803–808, https://doi.org/10.1111/j.1751-1097.1982.tb02651.x.
[193] A.S. Abdelfattah, S.L. Farhi, Y. Zhao, D. Brinks, P. Zou, A. Ruangkittisakul, J. Platisa, V.A. Pieribone, K. Ballanyi, A.E. Cohen, R.E. Campbell, A bright and fast red fluorescent protein voltage indicator that reports neuronal activity in organotypic brain slices, J. Neurosci. 36 (2016) 2458–2472, https://doi.org/10.1523/JNEUROSCI.3484-15.2016.
[194] T. Nakabayashi, K. Hino, Y. Ohta, S. Ito, H. Nakano, N. Ohta, Electric-field-induced changes in absorption and fluorescence of the green fluorescent protein chromophore in a PMMA film, J. Phys. Chem. B 115 (2011) 8622–8626, https://doi.org/10.1021/jp203090e.
[195] L.M. Leong, S.C. Shin, N. Frankiv, J.K. Rhee, H. Kim, J. Seong, J. Woo, K. Han, D. A. Storace, B.J. Baker, Modulating chromophore flexibility in GEVIs through threonine-based molecular switches reveals an influence of membrane curvature on protein activity, ACS Sens. 10 (2025) 8395–8410, https://doi.org/10.1021/acssensors.5c01748.
[196] B.E. Kang, S. Lee, B.J. Baker, Optical consequences of a genetically-encoded voltage indicator with a pH sensitive fluorescent protein, Neurosci. Res. 146 (2015) 13–21, https://doi.org/10.1016/j.neures.2018.10.006.
[197] R. Nakajima, A. Jung, B-J. Yoon, B.J. Baker, Optogenetic monitoring of synaptic activity with genetically encoded voltage indicators, Front. Synaptic Neurosci. 8 (2016) 22, https://doi.org/10.3389/fnsyn.2016.00022.
[198] M.Z. Lin, M.J. Schnitzer, Genetically encoded indicators of neuronal activity, Nat. Neurosci. 19 (2016) 1142–1153, https://doi.org/10.1038/nn.4359.
[199] A. Jung, J.E. Garcia, E. Kim, B-J. Yoon, B.J. Baker, Linker length and fusion site composition improve the optical signal of genetically encoded fluorescent voltage sensors, Neurophotonics 2 (2015) 021012, https://doi.org/10.1117/1.NPh.2.2.021012.
[200] D. Storace, M.S. Rad, B. Kang, L.B. Cohen, T. Hughes, B.J. Baker, Towards better genetically encoded sensors of membrane potential, Trends Neurosci 39 (2016) 277–289, https://doi.org/10.1016/j.tins.2016.02.005.
[201] M.S. Rad, Y. Choi, L.B. Cohen, B.J. Baker, S. Zhong, D.A. Storace, O.R. Braubach, Voltage and calcium imaging of brain activity, Biophys. J. 113 (2017) 2160–2167, https://doi.org/10.1016/j.bpj.2017.09.040.
[202] B. Yi, B.E. Kang, S. Lee, S. Braubach, B.J. Baker, A dimeric fluorescent protein yields a bright, red-shifted GEVI capable of population signals in brain slice, Sci. Rep. 8 (2018) 15199, https://doi.org/10.1038/s41598-018-33297-y.
[203] S-A. Li, X-Y. Meng, Y-J. Zhang, C-L. Chen, Y-X. Jiao, J-Q. Zhu, P-P. Liu, W. Sun, Progress in pH-sensitive sensors: essential tools for organelle pH detection, spotlighting mitochondrion and diverse application, Front. Pharmacol. 14 (2024) 1339518, https://doi.org/10.3389/fphar.2023.1339518.
[204] J.T.M. Kennis, D.S. Larsen, I.H.M. van Stokkum, M. Vengris, J.J. van Thor, Uncovering the hidden ground state of green fluorescent protein, Proc. Natl. Acad. Sci. U.S.A. 101 (2004) 17988–17993, https://doi.org/10.1073/pnas.0404262102.
[205] M. Drobizhev, R.S. Molina, P.R. Callis, J.N. Scott, G.G. Lambert, A. Salih, N. C. Shaner, T.E. Hughes, Local electric field controls fluorescence quantum yield of red and far-red fluorescent proteins, Front. Mol. Biosci. 8 (2021) 633217, https://doi.org/10.3389/fmolb.2021.633217.
[206] S. Inagaki, H. Tsutsui, K. Suzuki, M. Agetsuma, Y. Arai, Y. Jinno, G. Bai, M. J. Daniels, Y. Okamura, T. Matsuda, T. Nagai, Genetically encoded bioluminescent voltage indicator for multi-purpose use in wide range of bioimaging, Sci. Rep. 7 (2017) 42398, https://doi.org/10.1038/srep42398.
[207] P. Srinivasan, N.M Griffin, D. Thakur, P. Kulkarni, J.T. Eisdorfer, J.H. Rothman, C. Montell, L. Theogarajan, An autonomous molecular bioluminescent reporter (AMBER) for voltage imaging in freely moving animals, Adv. Biol. 5 (2021) 2100842, https://doi.org/10.1002/adbi.202100842.
[208] B.J. Baker, E.K. Kosmidis, D. Vucini, C.X. Falk, L.B. Cohen, M. Djurisic, D. Zecevic, Imaging brain activity with voltage- and calcium-sensitive dyes, Cell. Mol. Neurobiol. 25 (2005) 245–282, https://doi.org/10.1007/s10571-005-3059-6.
[209] G. Salama, B.-R. Choi, G. Azour, M. Lavasani, V. Tumbev, B.M. Salzberg, M. J. Patrick, L.A. Ernst, A.S. Waggoner, Properties of new, long-wavelength, voltage-sensitive dyes in the heart, J. Membr. Biol. 208 (2005) 125–140, https://doi.org/10.1007/s00232-005-0826-8.
[210] C.D. Acker, P. Yan, L.M. Loew, Recent progress in optical-sensor technology and applications to cardiac research: from single cells to whole hearts, Prog. Biophys. Mol. Biol. 154 (2020) 3–10, https://doi.org/10.1016/j.pbiomolbio.2019.07.004.
[211] P.E.Z. Klier, R. Roo, E.W. Miller, Fluorescent indicators for imaging membrane potential of organelles, Curr. Opin. Chem. Biol. 71 (2022) 102203, https://doi.org/10.1016/j.cbpa.2022.102203.
[212] P. Yan, C.D. Acker, V. Biasci, A. Monroe, L. Sacconi, L.M. Loew, Near-infrared voltage-sensitive dyes based on chromene donors, Proc. Natl. Acad. Sci. U.S.A. 120 (2023) e2305093120, https://doi.org/10.1073/pnas.2305093120.
[213] M.X. Navarro, N.C. Gerstner, S.M. Lipman, G.E. Dolgonos, E.W. Miller, Improved sensitivity in a modified Berkley Red sensor of transmembrane potential, ACS Chem. Biol. 19 (2024) 2214–2219, https://doi.org/10.1021/acschembio.4c00442.
[214] D.M. Nikolaev, V.N. Mironov, A.A. Shtyrov, I.D. Kvashnin, A.S. Mereshchenko, A. V. Vasin, M.S. Panov, M.N. Ryazantsev, Fluorescence imaging of cell membrane potential: from relative changes to absolute values, Int. J. Mol. Sci. 24 (2023) 2435, https://doi.org/10.3390/ijms24032435.
[215] Y. Xu, P. Zou, A.E. Cohen, Voltage imaging with genetically encoded indicators, Curr. Opin. Chem. Biol. 39 (2017) 1–10, https://doi.org/10.1016/j.cbpa.2017.04.005.
[216] H.H. Yang, F. St-Pierre, Genetically encoded voltage indicators: opportunities and challenges, J. Neurosci. 36 (2016) 9977–9989, https://doi.org/10.1523/JNEUROSCI.1095-16.2016.
[217] Y. Bando, C. Grimm, V.H. Cornejo, R. Yuste, Genetic voltage indicators, BMC Biol. 17 (2019) 71, https://doi.org/10.1186/s12915-019-0682-0.
[218] Y. Bando, M. Sakamoto, S. Kim, I. Ayzenshtat, R. Yuste, Comparative evaluation of genetically encoded voltage indicators, Cell Rep. 26 (2019) 802–813, https://doi.org/10.1016/j.celrep.2018.12.088.
[219] M. Canepari, D. Zecevic, O. Bernus (Eds.), Membrane Potential Imaging in the Nervous System and Heart, Springer International Publishing, Switzerland, 2015.
[220] T. Fiala, D. Sulzer, D. Sames, Seeing the spikes: the future of targetable synthetic voltage sensors, ACS Chem. Neurosci. 16 (2025) 761–771, https://doi.org/10.1021/acschemneuro.4c00849.
[221] Y.L. Huang, A.S. Walker, E.W. Miller, Photostable silicon rhodamine platform for optical voltage sensing, J. Am. Chem. Soc. 137 (2015) 10767–10776, https://doi.org/10.1021/jacs.5b06644.
[222] C.J. Roome, B. Kuhn, Voltage imaging with ANNINE dyes and two-photon microscopy of Purkinje dendrites in awake mice, Neurosci. Res. 152 (2020) 15–24, https://doi.org/10.1016/j.neures.2019.11.007.
[223] B. Ehrenberg, V. Montana, M.-D. Wei, J.P. Wuskell, L.M. Loew, Membrane potential can be determined in individual cells from Nernstian distribution of cationic dyes, Biophys. J. 53 (1988) 785–794, https://doi.org/10.1016/S0006-3495(88)83158-8.
[224] L. Bene, Oxonol has the potential to probe membrane fields, Cytometry A 83 (2013) 608–611, https://doi.org/10.1002/cyto.a.22314.
[225] S. Desai, S. Grefte, E. van de Westerlo, S. Lauwen, A. Paters, J.H.M. Prehn, Z. Gan, J. Keijer, M.J.W. Adjobo-Hermans, W.J.H. Koopman, Performance of TMRM and mitotrackers in mitochondrial morphofunctional analysis of primary human skin fibroblasts, Biochim. Biophys. Acta Bioenerg. 1865 (2024) 149027, https://doi.org/10.1016/j.bbabio.2023.149027.
[226] J.S. Treger, M.F. Priest, R. Iezzi, F. Bezanilla, Real-time imaging of electrical signals with an infrared FDA-approved dye, Biophys. Lett. 107 (2014) L09–L012, https://doi.org/10.1016/j.bpj.2014.07.054.
[227] I. Martišienė, R. Mačianskienė, R. Treinys, A. Navalinskas, M. Almanaitytė, D. Karčiauskas, A. Kučinskas, R. Grigalevičiūtė, V. Zigmantaitė, R. Benetis, J. Jurevičius, Voltage-sensitive fluorescence of indocyanine green in the heart, Biophys. J. 110 (2016) 723–732, https://doi.org/10.1016/j.bpj.2015.12.021.
[228] H. Zhang, X. He, X. Li, L. Guo, F. Meng, C. Li, Z. Liu, X. Yu, Permeability-controllable potentiometric probes enable visually discriminating near-zero and normal situations of cell membrane potential, Anal. Chem. 93 (2021) 2728–2732, https://doi.org/10.1021/acs.analchem.0c04928.
[229] I. Johnson, M.T.Z. Spence, The Molecular Probes Handbook, A Guide to Fluorescent Probes and Labeling Technologies, 11th ed., Invitrogen, 2010.
[230] J.E. González, M.P. Maher, Cellular fluorescent indicators and voltage/ion probe reader (VIPR): tools for ion channel and receptor drug discovery, Receptors and Channels 8 (2002) 283–295, https://doi.org/10.1080/10606820290005263.
[231] D. Wang, Z. Zhang, B. Chanda, M.B. Jackson, Improved probes for hybrid voltage sensor imaging, Biophys. J. 99 (2010) 2355–2365, https://doi.org/10.1016/j.bpj.2010.07.037.
[232] J. Bradley, R. Luo, T.S. Otis, D.A. DiGregorio, Submillisecond optical reporting of membrane potential *in situ* using neuronal tracer dye, J. Neurosci. 29 (2009) 9197–9209, https://doi.org/10.1523/JNEUROSCI.1240-09.2009.
[233] Y. Ma, P.O. Bayguinov, M.B. Jackson, Optical studies of action potential dynamics with hVOS probes, Curr. Opin. Biomed. Engin. 12 (2019) 51–58, https://doi.org/10.1016/j.cobme.2019.09.007.
[234] Z. Shapira, N. Degani-Katzav, S. Yudovich, A. Grupi, S. Weiss, Optical probing of local membrane potential with fluorescent polystyrene beads, Biophys. Rep. 1 (2021) 100030, https://doi.org/10.1016/j.bpr.2021.100030.
[235] H. Katano, Y. Kasahara, K. Ushimaru, C. Maruyama, Y. Hamono, Separation and purification of ε-poly-L-lysine with its colorimetric determination using dipicrylamine, Analyt. Sci. 31 (2015) 1273–1277. https://api.semanticscholar.org/CorpusID:33134297.
[236] B. Chanda, O.K. Asamoah, R. Blunck, B. Roux, F. Bezanilla, Gating charge displacement in voltage-gated ion channels involves limited transmembrane movement, Nature 436 (2005) 852–856, https://doi.org/10.1038/nature03888.
[237] H.J. Hughes, S.M.E. Demers, A. Zhang, J.H. Hafner, The orientation of a membrane probe from structural analysis by enhanced Raman scattering, Biochim. Biophys. Acta Biomembr. 1862 (2020) 183109, https://doi.org/10.1016/j.bbamem.2019.183109.
[238] A. Matiukas, B.G. Mitrea, M. Qin, A.M. Pertsov, A.G. Shvedko, M.D. Warren, A. V. Zaitsev, J.P. Wuskell, M. Wei, J. Watras, L.M. Loew, Near-infrared voltage-sensitive fluorescent dyes optimized for optical mapping in blood-perfused myocardium, Heart Rhythm. 4 (2007) 1441–1451, https://doi.org/10.1016/j.hrthm.2007.07.012.
[239] P. Yan, C.D. Acker, W-L. Zhou, P. Lee, C. Bollensdorff, A. Negrean, J. Lotti, L. Sacconi, S.D. Antic, P. Kohl, H.D. Mansvelder, F.S. Pavone, L.M. Loew, Palette of fluorinated voltage-sensitive hemicyanine dyes, Proc. Natl. Acad. Sci. U.S.A. 109 (2012) 20443–20448, https://doi.org/10.1073/pnas.1214850109.
[240] M. Ronzhina, T. Stracina, L. Lacinova, K. Ondacova, M. Pavlovicova, L. Marsanova, R. Smisek, O. Janousek, K. Fialova, J. Kolarova, M. Novakova, I. Provaznik, Di-4-ANEPPS modulates electrical activity and progress of

myocardial ischemia in rabbit isolated heart, Front. Physiol. 12 (2021) 667065, https://doi.org/10.3389/fphys.2021.667065.
[241] H. Zhang, H.N. Patton, G.A. Wood, P. Yan, L.M. Loew, C.D. Acker, G.P. Walcott, J. M. Rogers, Optical mapping of cardiac electromechanics in beating *in vivo* hearts, Biophys. J. 122 (2023) 4207–4219, https://doi.org/10.1016/j.bpj.2023.09.017.
[242] M. Kannan, G. Vasan, C. Huang, S. Haziza, J.Z. Li, H. Inan, M.J. Schnitzer, V. A. Pieribone, Fast, *in vivo* voltage imaging using a red fluorescent indicator, Nat. Methods 15 (2018) 1108–1116, https://doi.org/10.1038/s41592-018-0188-7.
[243] C. Beck, Y. Gong, A high-speed, bright, red fluorescent voltage sensor to detect neural activity, Sci. Rep. 9 (2019) 15878, https://doi.org/10.1038/s41598-019-52370-8.
[244] R.S. Bedlack, M-D. Wei, L.M. Loew, Localized membrane depolarizations and localized calcium influx during electric field-guided neurite growth, Neuron 9 (1992) 393–403, https://doi.org/10.1016/0896-6273(92)90178-g.
[245] W.Y. Kao, C.E. Davis, Y.I. Kim, J.M. Beach, Fluorescence emission spectral shift measurements of membrane potential in single cells, Biophys. J. 81 (2001) 1163–1170, https://doi.org/10.1016/S0006-3495(01)75773-6.
[246] R. Youngworth, B. Roux, Simulating the voltage-dependent fluorescence of di-8-ANEPPS in a lipid membrane, J. Phys. Chem. Lett. 14 (2023) 8268–8276, https://doi.org/10.1021/acs.jpclett.3c01257.
[247] M.J. Kirk, B.R Benlian, Y. Han, A. Gold, A. Ravi, P.E. Deal, R.S. Molina, M. Drobizhev, D. Dickman, K. Scott, E.W. Miller, Voltage imaging in *Drosophila* using a hybrid chemical-genetic rhodamine voltage reporter, Front. Neurosci. 15 (2021) 754027, https://doi.org/10.3389/fnins.2021.754027.
[248] P.E. Deal, R.U. Kulkarni, S.H. Al-Abdullatif, E.W. Miller, Isomerically pure tetramethylrhodamine voltage reporters, J. Am. Chem. Soc. 138 (2016) 9085–9088, https://doi.org/10.1021/jacs.6b05672.
[249] M.A. Gonzalez, A.S. Walker, K.J. Cao, J.R. Lazzari-Dean, N.S. Settineri, E.J. Kong, R.H. Kramer, E.W. Miller, Voltage imaging with a NIR-absorbing phosphine oxide rhodamine voltage reporter, J. Am. Chem. Soc. 143 (2021) 2304–2314, https://doi.org/10.1021/jacs.0c11382.
[250] S.C. Boggess, S.S. Gandhi, B.R. Benlian, E.W. Miller, Vinyl-fluorene molecular wires for voltage imaging with enhanced sensitivity and reduced phototoxicity, J. Am. Chem. Soc. 143 (2021) 11903–11907, https://doi.org/10.1021/jacs.1c04543.
[251] J.T. McCann, B.R. Benlian, S.K. Yaeger-Weiss, I.J. Knudson, M. He, E.W. Miller, Flipping the switch: reverse-demand voltage-sensitive fluorophores, J. Am. Chem. Soc. 144 (2022) 13050–13054, https://doi.org/10.1021/jacs.2c05385.
[252] A.M.M. Gest, J.R. Lazzari-Dean, G. Ortiz, S.K. Yaeger-Weiss, S.C. Boggess, E. W. Miller, Red-emitting carborhodamine for monitoring and measuring membrane potential, Proc. Natl. Acad. Sci. U.S.A 121 (2024) 28–35, https://doi.org/10.1073/pnas.2315264121.
[253] T. Jamieson, R. Bakhshi, D. Petrova, R. Pocock, M. Imani, A.M. Seifalian, Biological applications of quantum dots, Biomaterials 28 (2007) 4717–4732, https://doi.org/10.1016/j.biomaterials.2007.07.014.
[254] G. Chen, Y. Zhang, Z. Peng, D. Huang, C. Li, Q. Wang, Glutathione-capped quantum dots for plasma membrane labeling and membrane potential imaging, Nano Res. 12 (2019) 1321–1326, https://doi.org/10.1007/s12274-019-2283-1.
[255] O.K. Nag, M.H. Stewart, J.R. Deschamps, K. Susumu, E. Oh, V. Tsytsarev, Q. Tang, A.L. Efros, R. Vaxenburg, B.J. Black, Y. Chen, T.J. O'Shaughnessy, S.H. North, L. D. Field, P.E. Dawson, J.J. Pancrazio, I.L. Medintz, Y. Chen, R.S. Erzurumlu, A. L. Huston, J.B. Delehanty, Quantum dot-peptide-fullerene bioconjugates for visualization of *in vitro* and *in vivo* cellular membrane potential, ACS Nano 11 (2017) 5598–5613, https://doi.org/10.1021/acsnano.7b00954.
[256] M.H. Stewart, A.L. Huston, A.M. Scott, E. Oh, W.R. Algar, J.R Deschamps, K. Susumu, V. Jain, D.E. Prasuhn, J. Blanco-Canosa, P.E. Dawson, I.L. Medintz, Competition between Förster resonance energy transfer and electron transfer in stoichiometrically assembled semiconductor quantum dot-fullerene conjugates, ACS Nano 7 (2013) 9489–9505, https://doi.org/10.1021/nn403872x.
[257] R.N. Day, M.W. Davidson, The fluorescent protein palette: tools for cellular imaging, Chem. Soc. Rev. 38 (2009) 2887–2921, https://doi.org/10.1039/b901966a.
[258] I. Mollinedo-Gajate, C. Song, T. Knöpfel, Genetically encoded fluorescent calcium and voltage indicators, Handb. Exp. Pharmacol. 260 (2019) 209–229, https://doi.org/10.1007/164_2019_299.
[259] A. Perron, H. Mutoh, W. Akemann, S.G. Gautam, D. Dimitrov, Y. Iwamoto, T. Knöpfel, Second and third generation voltage-sensible fluorescent proteins for monitoring membrane potential, Front. Mol. Neurosci. 2 (2009) 5, https://doi.org/10.3389/neuro.02.005.2009.
[260] H. Mutoh, W. Akemann, T. Knöpfel, Genetically engineered fluorescent voltage reporters, ACS Chem. Neurosci. 3 (2012) 585–592, https://doi.org/10.1021/cn300041b.
[261] G. Miesenböck, D.A. Ahgelis, J.E. Rothman, Visualizing secretion and synaptic transmission with pH-sensitive green fluorescent proteins, Nature 394 (1998) 192–195, https://doi.org/10.1038/28190.
[262] P.O. Bayguinov, Y. Ma, Y. Gao, X. Zhao, M.B. Jackson, Imaging voltage in genetically defined neuronal subpopulations with a Cre recombinase-targeted hybrid voltage sensor, J. Neurosci. 37 (2017) 9305–9319, https://doi.org/10.1523/JNEUROSCI.1363-17.2017.
[263] Y. Gong, C. Huang, J.Z. Li, B.F. Grewe, Y. Zhang, S. Eismann, M.J. Schnitzer, High-speed recording of neural spikes in awake mice and flies with a fluorescent voltage sensor, Science 350 (2015) 1361–1366, https://doi.org/10.1126/science.aab0810.
[264] D. Dimitrov, Y. He, H. Mutoh, B.J. Baker, L. Cohen, A. Akemann, T. Knöpfel, Engineering and characterization of an enhanced fluorescent protein voltage sensor, PLoS One 5 (2007) e440, https://doi.org/10.1371/journal.pone.0000440.
[265] M.J. Lam, F. St-Pierre, Y. Gong, J.D. Marshall, P.J. Cranfill, M.A. Baird, M. R. McKeown, J. Wiedenmann, M.W. Davidson, M.J. Schnitzer, R.Y. Tsien, M. Z. Lin, Improving FRET dynamic range with bright green and red fluorescent proteins, Nat. Methods 9 (2012) 1005–1012, https://doi.org/10.1038/nmeth.2171.
[266] H. Tsutsui, Y. Tomita, Y. Niino, Y. Yamada, K. Mikoshiba, A. Miyawaki, Y. Okamura, Improved detection of electrical activity with a voltage probe based on a voltage-sensing phosphatase, J. Physiol. 591 (2013) 4427–4437, https://doi.org/10.1113/jphysiol.2013.257048.
[267] W. Akemann, H. Mutoh, A. Perron, J. Rossier, T. Knöpfel, Imaging neural circuit dynamics with a voltage-sensitive fluorescent protein, J. Neurophysiol. 108 (2012) 2323–2337, https://doi.org/10.1152/jn.00452.2012.
[268] U. Sung, M. Sepehri-Rad, H.H. Piao, L. Jin, T. Hughes, L.B. Cohen, B.J. Baker, Developing fast fluorescent protein voltage sensors by optimizing FRET interactions, PLoS One 10 (2015) e0141585, https://doi.org/10.1371/journal.pone.0141585.
[269] L.A. Kost, E.S. Nikitin, V.O. Ivanova, U. Sung, E.V. Putintseva, D.M. Chudakov, P. M. Balaban, K.A. Bogdanov, Insertion of voltage-sensitive domain into circularly permuted red fluorescent protein as a design for genetically encoded voltage sensor, PLoS One 12 (2017) e0184225, https://doi.org/10.1371/journal.pone.0184225.
[270] S. Lee, T. Geiller, A. Jung, R. Nakajima, Y.K. Song, B.J. Baker, Improving a genetically encoded voltage indicator by modifying the cytoplasmic charge composition, Sci. Rep. 7 (2017) 8286, https://doi.org/10.1038/s41598-017-08731-2.
[271] Z. Han, L. Jin, F. Chen, J.J. Loturco, L.B. Cohen, A. Bondar, J. Lazar, V. A. Pieribone, Mechanistic studies of the genetically encoded fluorescent protein voltage probe ArcLight, PLoS One 9 (2014) e113873, https://doi.org/10.1371/journal.pone.0113873.
[272] S. Chamberland, H.H. Yang, M.M. Pan, S.W. Evans, S. Guan, M. Chavarha, Y. Yang, C. Salesse, H. Wu, J.C. Wu, T.R. Clandinin, K. Toth, M.Z. Lin, F. St-Pierre, Fast two-photon imaging of subcellular voltage dynamics in neuronal tissue with genetically encoded indicator, eLife 6 (2017) e25690, https://doi.org/10.7554/eLife.25690.
[273] O.P. Ernst, D.T. Lodowski, M. Elstner, P. Hegemann, L.S. Brown, H. Kandori, Microbial and animal rhodopsins: structures, functions, and molecular mechanisms, Chem. Rev. 114 (2014) 126–163, https://doi.org/10.1021/cr4003769.
[274] Z. Liu, X. Lu, V. Villette, Y. Gou, K.L. Colbert, S. Lai, S. Guan, M.A. Land, J. Lee, T. Assefa, D.R. Zollinger, M.M. Korympidou, A.L. Vlasits, M.M. Pang, S. Su, C. Cai, E. Froudarakis, N. Zhou, S.S. Patel, C.L. Smith, A. Ayon, P. Bizouard, J. Bradley, K. Franke, T.R. Clandinin, A. Giovannucci, A.S. Tolias, J. Reimer, S. Dieudonné, F. St-Pierre, Sustained deep-tissue voltage recording using a fast indicator evolved for two-photon microscopy, Cell 1185 (2022) 3408–3425, https://doi.org/10.1016/j.cell.2022.07.013.
[275] Z. Han, L. Jin, J. Platisa, L.B. Cohen, B.J. Baker, V.A. Pierebone, Fluorescent protein voltage probes derived from ArcLight that respond to membrane voltage changes with fast kinetics, PLoS One 8 (2013) e81295, https://doi.org/10.1371/journal.pone.0081295.
[276] B.J. Baker, H. Mutoh, D. Dimitrov, W. Akemann, A. Perron, Y. Iwamoto, L. Jin, L. B. Cohen, E.Y. Isacoff, V.A. Pieribone, T. Hughes, T. Knöpfel, Genetically encoded fluorescent sensors of membrane potential, Brain Cell Biol. 36 (2008) 53–67, https://doi.org/10.1007/s11068-008-9026-7.
[277] Y. Mishina, H. Mutoh, C. Song, T. Knöpfel, Exploration of genetically encoded voltage indicators based on a chimeric voltage sensing domain, Front. Mol. Neurosci. 7 (2014) 78, https://doi.org/10.3389/fnmol.2014.00078.
[278] Y. Mishina, H. Mutoh, T. Knöpfel, Transfer of Kv3.1 voltage sensor features to the isolated Ci-VSP voltage-sensing domain, Biophys. J. 103 (2012) 669–676, https://doi.org/10.1016/j.bpj.2012.07.031.
[279] H. Tian, H.C. Davis, J.D. Wong-Campos, P. Park, L.Z. Fan, B. Gmeiner, S. Begum, C.A. Werley, G.B. Borja, H. Upadhyay, H. Shah, J. Jacques, Y. Qi, V. Parot, K. Deisseroth, A.E. Cohen, Video-based pooled screening yields improved far-red genetically encoded voltage indicators, Nat. Methods 20 (2023) 1082–1094, https://doi.org/10.1038/s41592-022-01743-5.
[280] H.H. Piao, D. Rajakumar, B.E. Kang, E.H. Kim, B.J. Baker, Combinatorial mutagenesis of the voltage-sensing domain enables the optical resolution of action potentials firing at 60 Hz by a genetically encoded fluorescent sensor of membrane potential, J. Neurosci. 35 (2015) 372–385, https://doi.org/10.1523/JNEUROSCI.3008-14.2015.
[281] J. Platisa, G. Vasan, A. Yang, V.A. Pieribone, Directed evolution of key residues in fluorescent protein inverses the polarity of voltage sensitivity in genetically encoded indicator ArcLight, ACS Chem. Neurosci. 8 (2017) 513–523, https://doi.org/10.1021/acschemneuro.6b00234.
[282] A. Petruškevičiūtė, U. Šimuliūnaitė, C.M. Polanco, B. Rojas, S. Kuras, B. Valatkaitė-Rakštienė, R. Norvilas, A.K. Vijaya, P. Muñoz, U. Neniškytė, A. Jakubauskas, A. Burokas, I. Nalvarte, J. Inzunza, D. Naumovas, M. Stoškus, L. Griškevičiusb, D. Baltriukienė, J. Arias, Generation of a genetically encoded voltage indicator MARINA reporter human iPS cell line using Cas9 (VULSCi002-A-2), Stem Cell Res. 82 (2025) 103628, https://doi.org/10.1016/j.scr.2024.103628.
[283] M.V. Monakhov, M.E. Matlashov, M. Colavita, C. Song, D.M. Shcherbakova, S. D. Antic, V.V. Verkhusha, T. Knöpfel, Screening and cellular characterization of genetically encoded voltage indicators based on near-infrared fluorescent proteins, ACS Chem. Neurosci. 11 (2020) 3523–3531, https://doi.org/10.1021/acschemneuro.0c00046.

[284] C. Song, M.E. Matlashov, D.M. Shcherbakova, S.D. Antic, V.V. Verkhusha, T. Knöpfel, Characterization of two near-infrared genetically encoded voltage indicators, Neurophotonics 11 (2024) 024201, https://doi.org/10.1117/1.NPh.11.2.024201.
[285] S.W. Evans, D-Q. Shi, M. Chavarha, M.H. Plitt, J. Taxidis, B. Madruga, J.L. Fan, F-J. Hwang, S.C. van Keulen, C-M. Suomivuori, M.M. Pang, S. Su, S. Lee, Y.A. Hao, G. Zhang, D. Jiang, L. Pradhan, R.H. Roth, Y. Liu, C.C. Dorian, A.L. Reese, A. Negrean, A. Losonczy, C.D. Makinson, S. Wang, T.R. Clandinin, R.O. Dror, J. B. Ding, N. Ji, P. Golshani, L.M. Giocomo, G-Q. Bi, M.Z. Lin, A positively tuned voltage indicator for extended electrical recordings in the brain, Nature Methods 20 (2023) 1104–1113, https://doi.org/10.1038/s41592-023-01913-z.
[286] J. Platisa, X. Ye, A.M. Ahrens, C. Liu, I.A. Chen, I.G. Davison, L. Tian, V. A. Pieribone, J.L. Chen, High-speed low-light *in vivo* two-photon voltage imaging of large neuronal populations, Nat. Methods 20 (2023) 1095–1103, https://doi.org/10.1038/s41592-023-01820-3.
[287] X. Lu, Y. Wang, Z. Liu, Y. Gou, D. Jaeger, F. St-Pierre, Widefield imaging of rapid pan-cortical voltage dynamics with an indicator evolved for one-photon microscopy, Nature Communications 14 (2023) 6423, https://doi.org/10.1038/s41467-023-41975-3.
[288] T.E. DeCoursey, Voltage-gated proton channels: molecular biology, physiology, and pathophysiology of the H(V) family, Physiol. Rev. 93 (2013) 599–652, https://doi.org/10.1152/physrev.00011.2012.
[289] W.A. Catterwall, Molecular properties of voltage-sensitive sodium channels, Annu. Rev. Biochem. 55 (1986) 953–985, https://doi.org/10.1146/annurev.bi.55.070186.004513.
[290] H.R. Guy, P. Seetharamulu, Molecular model of the action potential sodium channel, Proc. Natl. Acad. Sci. U.S.A. 83 (1986) 508–512, https://doi.org/10.1073/pnas.83.2.508.
[291] V. Ruta, J. Chen, R. MacKinnon, Calibrated measurement of gating-charge arginine displacement in the KvAP voltage-dependent K^+ channel, Cell 123 (2005) 463–475, https://doi.org/10.1016/j.cell.2005.08.041.
[292] W.A. Catterwall, Ion channel voltage sensors: structure, function, and pathophysiology, Neuron 67 (2010) 915–928, https://doi.org/10.1016/j.neuron.2010.08.021.
[293] A. Moreau, P. Gosselin-Badaroudine, M. Chahine, Biophysics, pathophysiology, and pharmacology of ion channel gating pores, Front. Pharmacol. 5 (2014) 53, https://doi.org/10.3389/fphar.2014.00053.
[294] M. de Lera Ruiz, R.L. Kraus, Voltage-gated sodium channels: structure, function, pharmacology, and clinical indications, J. Med. Chem. 58 (2015) 7093–7118, https://doi.org/10.1021/jm501981g.
[295] F. St-Pierre, M. Chavarha, M.Z. Lin, Designs and sensing mechanisms of genetically encoded fluorescent voltage indicators, Curr. Opin. Chem. Biol. 27 (2015) 31–38, https://doi.org/10.1016/j.cbpa.2015.05.003.
[296] C. Arcos-Hernández, T. Nishigaki, Ion currents through the voltage sensor domain of distinct families of proteins, J. Biol. Phys. 49 (2023) 393–413, https://doi.org/10.1007/s10867-023-09645-z.
[297] M. Köhn, Turn and face the strange: a new view on phosphatases, ACS Cent. Sci. 6 (2020) 467–477, https://doi.org/10.1021/acscentsci.9b00909.
[298] M. Guo, Z. Li, M. Gu, J. Gu, Q. You, L. Wang, Targeting phosphatases: from molecule design to clinical trials, Eur. J. Med. Chem. 264 (2024) 116031, https://doi.org/10.1016/j.ejmech.2023.116031.
[299] Y. Okamura, Y. Murata, H. Iwasaki, Voltage-sensing phosphatase: actions and potentials, J. Physiol. 587 (2009) 513–520, https://doi.org/10.1113/jphysiol.2008.163097.
[300] C.A. Villabla-Galea, Voltage-controlled enzymes: the new *Janus Bifrons*, Front. Pharmacol. 3 (2012) 161, https://doi.org/10.3389/fphar.2012.00161.
[301] S. Yamaguchi, T. Kurokawa, I. Taira, N. Aoki, S. Sakata, Y. Okamura, K. J. Homma, Potential role of voltage-sensing phosphatases in regulation of cell structure through the production of $PI(3,4)P_2$, J. Cell. Physiol. 229 (2014) 422–433, https://doi.org/10.1002/jcp.24463.
[302] S. Yamaguchi, N. Aoka, T. Kitajima, Y. Okamura, K.J. Homma, Expression of the voltage-sensing phosphatase gene in the chick embryonic tissues and in the adult cerebellum, Communicative & Integrative Biology 7 (2014) e9705021, https://doi.org/10.4161/19420889.2014.970502.
[303] J. Platisa, V.A. Pieribone, Genetically encoded fluorescent voltage indicators: are we here yet? Curr. Opin. Neurobiol. 50 (2018) 146–153, https://doi.org/10.1016/j.conb.2018.02.006.
[304] L.C. Panzera, M.B. Hoppa, Genetically encoded voltage indicators are illuminating subcellular physiology of the axon, Front. Cell. Neurosci. 13 (2019) 52, https://doi.org/10.3389/fncel.2019.00052.
[305] X. Meng, S. Ganapathy, L. van Roemburg, D. Brinks, Voltage imaging with engineered proton-pumping rhodopsins: insights from the proton transfer pathway, ACS Phys. Chem. Au 3 (2023) 320–333, https://doi.org/10.1021/acsphyschemau.3c00003.
[306] K. Kojima, Y. Sudo, Convergent evolution of animal and microbial rhodopsins, RSC Adv. 13 (2023) 5367–5381, https://doi.org/10.1039/D2RA07073A.
[307] E.G. Govorunova, O.A. Sineshchekov, H. Li, J.L. Spudich, Microbial rhodopsins: diversity, mechanisms, and optogenetic applications, Annu. Rev. Biochem. 86 (2017) 845–872, https://doi.org/10.1146/annurev-biochem-101910-144233.
[308] A. Rozenberg, K. Inoue, H. Kandori, O. Béjà, Microbial rhodopsins: the last two decades, Annu. Rev. Microbiol. 75 (2021) 427–447, https://doi.org/10.1146/annurev-micro-031721-020452.
[309] L.S. Brown, Light-driven proton transfers and proton transport by microbial rhodopsins – a biophysical perspective, BBA – Biomembranes 1864 (2022) 183867, https://doi.org/10.1016/j.bbamem.2022.183867.
[310] A. Okuyama, S. Hososhima, H. Kandori, S.P. Tsunoda, Driving forces of proton-pumping rhodopsins, Biophys. J. 123 (2024) 4274–4284, https://doi.org/10.1016/j.bpj.2024.09.007.
[311] D. Oesterhelt, W. Stoeckenius, Rhodopsin-like protein from the purple membrane of *Halobacterium halobium*, Nat. New Biol. 233 (1971) 149–152, https://doi.org/10.1038/newbio233149a0.
[312] J.K. Lanyi, Bacteriorhodopsin, Int. Rev. Cytol. 187 (1999) 161–202, https://doi.org/10.1016/s0074-7696(08)62418-3.
[313] O. Béjà, L. Aravind, E.V. Koonin, M.T. Suzuki, A. Hadd, L.P. Nguyen, S. B. Jovanovich, C.M. Gates, R.A. Feldman, J.L. Spudich, E.N. Spudich, E. F. DeLong, Bacterial rhodopsin: evidence for a new type of phototrophy in the sea, Science 289 (2000) 1902–1906, https://doi.org/10.1126/science.289.5486.1902.
[314] O. Béjà, E.N. Spudich, J.L. Spudich, M. Leclerc, E.F. DeLong, Proteorhodopsin phototrophy in the ocean, Nature 411 (2001) 786–789, https://doi.org/10.1038/35081051.
[315] T. Friedrich, S. Geibel, R. Kalmbach, I. Chizhov, K. Ataka, J. Heberle, M. Engelhard, E. Bamberg, Proteorhopsin is a light-driven proton pump with variable vectoriality, J. Mol. Biol. 321 (2002) 821–838, https://doi.org/10.1016/s0022-2836(02)00696-4.
[316] K. Ihara, T. Umemura, I. Katagirri, T. Kitajima-Ihara, Y. Sugiyama, Y. Kimura, Y. Mukohata, Evolution of archaeal rhodoposins: evolution rate changes by gene duplication and functional differentiation, J. Mol. Biol. 285 (1999) 163–174, https://doi.org/10.1006/jmbi.1998.2286.
[317] E.C. Saint Clair, J.L. Ogren, S. Mamaev, D. Russano, J.M. Kralj, K.J. Rothschild, Near-IR resonance Raman spectroscopy of archaerhodopsin 3: effects of transmembrane potential, J. Phys. Chem. B 116 (2012) 14592–14601, https://doi.org/10.1021/jp309996a.
[318] J.F. Bada Juarez, P.J. Judge, S. Adam, D. Axford, J. Vinals, J. Birch, T.O.C. Kwan, K.K. Hoi, H-Y. Yen, A. Vial, P-E. Milhiet, C.V. Robinson, I. Schapiro, I. Moraes, A. Watts, Structures of the archaerhodopsin-3 transporter reveal that disordering of internal water networks underpins receptor sensation, Nat. Comm. 12 (2021) 629, https://doi.org/10.1038/s41467-020-20596-0.
[319] K. Herasymenko, D. Walisinghe, M. Konno, L. Barneschi, I. de Waele, M. Sliwa, K. Inoue, M. Olivucci, S. Haacke, Archaerhodopsin 3 is an ideal template for the engineering of highly fluorescent optogenetic reporters, Chem. Sci. 16 (2024) 761–774, https://doi.org/10.1039/d4sc05120c.
[320] S.P. Tsunoda, D. Ewers, S. Gazzarrini, A. Moroni, D. Gradmann, P. Hegemann, H $^+$-pumping rhodopsin from the marine alga *Acetabularia*, Biophys. J. 91 (2006) 1471–1479, https://doi.org/10.1529/biophysj.106.086421.
[321] T. Wada, K. Shimono, T. Kikukawa, M. Hato, N. Shinya, S.Y. Kim, T. Kimura-Someya, M. Shirouzu, J. Tamogami, S. Miyauchi, K-H. Jung, N. Kamo, S. Yokoyama, Crystal structure of eukaryotic light-driven proton-pumping rhodopsin, *Acetabulgaria* rhodopsin II, from marine alga, J. Mol. Biol. 411 (2011) 986–998, https://doi.org/10.1016/j.jmb.2011.06.028.
[322] P. Kolodner, E.P. Lukashev, Y-C. Ching, D.L. Rousseau, Electric-field-induced Schiff-base deprotonation in D85N mutant bacteriorhodopsin, Proc. Natl. Acad. Sci. U.S.A. 93 (1996) 11618–11621, https://doi.org/10.1073/pnas.93.21.11618.
[323] A. Penzkofer, A. Silapetere, P. Hegemann, Photodynamics of the Archaerhodopsin 3 based fluorescent voltage sensor QuasAr1, Int. J. Mol. Sci. 20 (2019) 4086, https://doi.org/10.3390/ijms21010160.
[324] A. Penzkofer, A. Silapetere, P. Hegemann, Photodynamics of the Archaerhodopsin 3 based fluorescent voltage sensor Archon2, J. Photochem. Photobiol. B: Biol. 225 (2021) 112331, https://doi.org/10.1016/j.jphotobiol.2021.112331.
[325] A. Penzkofer, A. Silapetere, P. Hegemann, Theoretical investigation of the photocycle dynamics of the Archaerhodopsin 3 based fluorescent voltage sensor Archon2, J. Photochem. Photobiol. A: Chem. 437 (2023) 114366, https://doi.org/10.1016/j.jphotochem.2022.114366.
[326] F.P. Brooks, D. Gong, H.C. Davis, P. Park, Y. Qi, A.E. Cohen, Photophysics-informed two-photon voltage imaging using FRET-opsin voltage indicators, Sci. Adv. 11 (2025) eadp5763, https://doi.org/10.1126/sciadv.adp5763.
[327] L. Barneschi, E. Marsili, L. Pedraza-González, D. Padula, L. De Vico, D. Kaliakin, A. Blanco-González, N. Ferré, M. Huix-Rotllant, M. Filatov, M. Olivucci, On the fluorescence enhancement of arch neuronal optogenetic reporters, Nat. Comm. 13 (2022) 6432, https://doi.org/10.1038/s41467-022-33993-4.
[328] D. di Prima, L.M. Pedraza-González, P. Reinholdt, J. Kongsted, Fluorescent rhodopsins: a challenging test for cost-effective QM/MM approaches, J. Phys. Chem. 129 (2025) 1769–1778, https://doi.org/10.1021/acs.jpca.4c07733.
[329] Y. Gong, J.Z. Li, M.J. Schnitzer, Enhanced Archaerhodopsin fluorescent protein voltage indicators, PLoS One 8 (2013) e66959, https://doi.org/10.1371/journal.pone.0066959.
[330] N.C. Flytzanis, C.N. Bedbrook, M.K.M. Engqvist, C. Xiao, K.Y. Chan, P. W. Sternberg, F.H. Arnold, V. Gradinaru, Archaerhodopsin variants with enhanced voltage-sensitive fluorescence in mammalian and *Caenorhabditis elegans* neurons, Nat. Comm. 5 (2014) 4894, https://doi.org/10.1038/ncomms5894.
[331] Y. Adam, J.J. Kim, S. Lou, Y. Zhao, M.E. Xie, D. Brinks, H. Wu, M.A. Mostajo-Radji, S. Kheifets, V. Parot, S. Chettih, K.J. Williams, B. Gmeiner, S.L. Farhi, L. Madisen, E.K. Buchanan, I. Kinsella, D. Zhou, L. Paninski, C.D. Harvey, H. Zeng, P. Arlotta, R.E. Campbell, A.E. Cohen, Voltage imaging and optogenetics reveal behavior-dependent changes in hippocampal dynamics, Nature 569 (2019) 413–417, https://doi.org/10.1038/s41586-019-1166-7.
[332] K.D. Piatkevich, E.E. Jung, C. Straub, C. Linghu, D. Park, H.J. Suk, D. R. Hochbaum, D. Goodwin, E. Pnevmatikakis, N. Pak, T. Kawashima, C.T. Yang, J. L. Rhoades, O. Shemesh, S. Asano, Y.G. Yoon, L. Freifeld, J.L. Saulnier, C. Riegler, F. Engert, T. Hughes, M. Drobizhev, B. Szabo, M.B. Ahrens, S.W. Flavell, B. L. Sabatini, E.S. Boyden, A robotic multidimensional directed evolution approach

applied to fluorescent voltage reporters, Nat. Chem. Biol. 14 (2018) 352–360, https://doi.org/10.1038/s41589-018-0004-9.
[333] K.D. Piatkevich, S. Bensussen, H. Tseng, S.N. Shroff, V.G. Lopez-Huerta, D. Park, E.E. Jung, O.A. Shemesh, C. Straub, H.J. Gritton, M.F. Romano, E. Costa, B. L. Sabatini, Z. Fu, E.S. Boyden, X. Han, Population imaging of neural activity in awake behaving mice, Nature 574 (2019) 413–417, https://doi.org/10.1038/s41586-019-1641-1.
[334] M-P. Chien, D. Brinks, G. Testa-Silva, H. Tian, F.P. Brooks III, Y. Adam, B. Bloxham, B. Gmeiner, S. Kheifets, A.E. Cohen, Photoactivated voltage imaging in tissue with an archaerhodopsin-derived reporter, Sci. Adv. 7 (2021) eabe3216, https://doi.org/10.1126/sciadv.abe3216.
[335] G. Mei, C.M. Cavini, N. Mamaeva, P. Wang, W.J. DeGrip, K.J. Rothschild, Optical switching between long-lived states of opsin transmembrane voltage sensors, Photochem. Photobiol. 97 (2021) 1001–1015, https://doi.org/10.1111/php.13428.
[336] R.S. McIsaac, M.K. Engqvist, T. Wannier, A.Z. Rosenthal, L. Herwig, N. C. Flytzanis, E.S. Imasheva, J.K. Lanyi, S.P. Balashov, V. Gradinaru, F.H. Arnold, Directed evolution of a far-red fluorescent rhodopsin, Proc. Natl. Acad. Sci. U.S.A. 111 (2014) 13043–13049, https://doi.org/10.1073/pnas.1413987111.
[337] X. Xiao, A. Yang, H. Zhang, D. Park, Y. Wang, B. Szabo, E.S. Boyden, K. D. Piatkevich, Engineering of genetically encoded bright near-infrared fluorescent voltage indicator, Int. J. Mol. Sci. 26 (2025) 1442, https://doi.org/10.3390/ijms26041442.
[338] D.M. Nikolaev, V.N. Mironov, E.M. Metelkina, A.A. Shtyrov, A.S. Mereshchenko, N.A. Demidov, S.Y. Vyazmin, T.B. Tennikova, S.E. Moskalenko, S.A. Bondarev, G. A. Zhouravleva, A.V. Vasin, M.S. Panov, M.N. Ryazantsev, Rational design of far-red archaerhodopsin-3-based fluorescent genetically encoded voltage indicators: from elucidation of the fluorescence mechanism in Archers to novel red-shifted variants, ACS Phys. Chem. Au 4 (2024) 347–362, https://doi.org/10.1021/acsphyschemau.3c00073.
[339] K. Kojima, R. Kurihara, M. Sakamoto, T. Takanashi, H. Kuramochi, X.M. Zhang, H. Bito, T. Tahara, Y. Sudo, Comparative studies of the fluorescence properties of microbial rhodopsins: spontaneous emission versus photointermediate fluorescence, J. Phys. Chem. B 124 (2020) 7361–7367, https://doi.org/10.1021/acs.jpcb.0c06560.
[340] A. Penzkofer, A. Silapetere, P. Hegemann, Absorption and emission spectroscopic investigation of the thermal dynamics of the Archaerhodopsin 3 based fluorescent voltage sensor Archon2, Int. J. Mol. Sci. 21 (2020) 6576, https://doi.org/10.3390/ijms20174086.
[341] G. Mei, N. Mamaeva, S. Ganapathy, P. Wang, J. DeGrip, K.J. Rothschild, Analog retinal redshifts visible absorption of QuasAr transmembrane voltage sensors into near-infrared, Photochem. Photobiol. 96 (2020) 55–66, https://doi.org/10.1111/php.13169.
[342] D. Brinks, A. Klein, A. Cohen, Two-photon lifetime imaging of voltage indicating proteins as a probe of absolute membrane voltage, Biophys. J. 109 (5) (2015) 914–921, https://doi.org/10.1016/j.bpj.2015.07.038.
[343] E. Kiskinis, J.M. Kralj, P. Zou, E.N. Weinstein, H. Zhang, K. Tsioras, O. Wiskow, J. A. Ortega, K. Eggan, A.E. Cohen, All-optical electrophysiology for high-throughput functional characterization of a human iPSC-derived motor neuron model of ALS, Stem Cell Rep. 10 (2018) 1991–2004, https://doi.org/10.1016/j.stemcr.2018.04.020.
[344] L.Z. Fan, R. Nehme, Y. Adam, E.S. Jung, H. Wu, K. Eggan, D.B. Arnold, A. E. Cohen, All-optical synaptic electrophysiology probes mechanism of ketamine-induced disinhibition, Nat. Methods 15 (2018) 823–831, https://doi.org/10.1038/s41592-018-0142-8.
[345] L.Z. Fan, S. Kheifets, U.L. Bohm, H. Wu, K.D. Piatkevich, M.E. Xie, V. Parot, Y. Ha, K.E. Evans, E.S. Boyden, A.E. Takesian, A.E. Cohen, All-optical electrophysiology reveals the role of lateral inhibition in sensory processing in cortical layer 1, Cell 180 (2020) 521–535, https://doi.org/10.1016/j.cell.2020.01.001.
[346] S. Liu, C. Lin, Y. Xu, H. Luo, L. Peng, X. Zeng, H. Zheng, P.R. Chen, P. Zou, A far-red hybrid voltage indicator enabled by bioorthogonal engineering of rhodopsin on live neurons, Nat. Chem. 13 (2021) 472–479, https://doi.org/10.1038/s41557-021-00641-1.
[347] Y. Xu, L. Peng, S. Wang, A. Wang, R. Ma, Y. Zhou, J. Yang, D.E. Sun, W. Lin, X. Chen, P. Zou, Hybrid indicators for fast and sensitive voltage imaging, Angew. Chem. Int. Ed. 57 (2018) 3949–3953, https://doi.org/10.1002/anie.201712614.
[348] A.S. Abdelfattah, J. Zheng, A. Singh, Y.C. Huang, D. Reep, G. Tsegaye, A. Tsang, B.J. Arthur, M. Rehorova, C.V.L. Olson, Y. Shuai, L. Zhang, T.M. Fu, D.E. Milkie, M.V. Moya, T.D. Weber, A.L. Lemire, C.A. Baker, N. Falco, Q. Zheng, J.B. Grimm, M.C. Yip, D. Walpita, M. Chase, L. Campagnola, G.J. Murphy, A.M. Wong, C. R. Forest, J. Mertz, M.N. Economo, G.C. Turner, M. Koyama, B.J. Lin, E. Betzig, O. Novak, L.D. Lavis, K. Svoboda, W. Korff, T.W. Chen, E.R. Schreiter, J. P. Hasseman, I. Kolb, Sensitivity optimization of a rhodopsin-based fluorescent voltage indicator, Neuron 111 (2023) 1547–1563, https://doi.org/10.1016/j.neuron.2023.03.009.
[349] Y. Adam, All-optical electrophysiology in behaving animals, J. Neurosci. Methods 353 (2021) 109101, https://doi.org/10.1016/j.jneumeth.2021.109101.
[350] A. Klimas, C.M. Ambrosi, J. Yu, J.C. Williams, H. Bien, E. Entcheva, OptoDyCE as an automated system for high-throughput all-optical dynamic cardiac electrophysiology, Nat. Commun. 7 (2016) 11542, https://doi.org/10.1038/ncomms11542.
[351] J. Streit, S. Kleinlogel, Dynamic all-optical drug screening on cardiac voltage gated ion channels, Scientific Reports 8 (2018) 1153, https://doi.org/10.1038/s41598-018-19412-z.
[352] H. Zhang, E. Reichert, A.E. Cohen, Optical electrophysiology for probing function and pharmacology of voltage-gated ion channels, eLife 5 (2026) e15202, https://doi.org/10.7554/eLife.15202.
[353] X. Meng, L. Huismans, T. Huijben, G. Szabo, R. van Tol, I. de Heer, S. Ganapathy, D. Brinks, A compact microscope for voltage imaging, J. Opt. 24 (2022) 054004, https://doi.org/10.1088/2040-8986/ac5dd5.
[354] 1 S. Lou, Y. Adam, E.N. Weinstein, E. Williams, K. Williams, V. Parot, N. Kavokine, S. Liberles, L. Madisen, H. Zeng, A.E. Cohen, Genetically targeted all-optical electrophysiology with a transgenic Cre-dependent optopatch mouse, J. Neurosci. 36 (2016) 11059–11073, https://doi.org/10.1523/JNEUROSCI.1582-16.2016.
[355] G. Nagel, T. Szellas, W. Huhn, S. Kateriya, N. Adeishvili, P. Berthold, D. Ollig, P. Hegemann, E. Bamberg, Channelrhodopsin-2, a directly light-gated cation-selective membrane channel, Proc. Natl. Acad. Sci. (USA) 100 (2003) 13940–13945, https://doi.org/10.1073/pnas.1936192100.
[356] D.M. Shcherbakova, Near-infrared and far-red genetically encoded indicators of neuronal activity, J. Neurosci. Methods 362 (2021) 109314, https://doi.org/10.1016/j.jneumeth.2021.109314.
[357] C. Dong, Y. Zheng, K. Long-Iyer, E.C. Wright, Y. Li, L. Tian, Fluorescence imaging of neural activity, neurochemical dynamics, and drug-specific receptor conformation with genetically encoded sensors, Annu. Rev. Neurosci. 45 (2022) 273–294, https://doi.org/10.1146/annurev-neuro-110520-031137.
[358] Y. Jung, S. Lee, J.K. Rhee, C-E. Lee, B.J. Baker, Y-K. Song, Imaging electrical activity of retinal ganglion cells with fluorescent voltage and calcium indicator proteins in retinal degenerative *rd1* blind mice, ACS Chem. Neurosci. 16 (2025) 4711–4724, https://doi.org/10.1021/acschemneuro.5c00740.
[359] M.C. Müllenbroich, A. Kelly, C. Acker, G. Bub, T. Bruegmann, A. Di Bona, E. Entcheva, C. Ferrantini, P. Kohl, S.E. Lehnart, M. Mongillo, C. Parmeggiani, C. Richter, P. Sasse, T. Zaglia, L. Sacconi, G.L. Smith, Novel optics-based approaches for cardiac electrophysiology: a review, Front. Physiol. 12 (2021) 769586, https://doi.org/10.3389/fphys.2021.769586.
[360] T.D. Weber, M.V. Moya, K. Kiliç, J. Mertz, M.N. Economo, High-speed multiplane confocal microscopy for voltage imaging in densely labeled neuronal populations, Nat. Neurosci. 26 (2023) 1642–1650, https://doi.org/10.1038/s41593-023-01408-2.
[361] S. Haziza, R. Chrapkiewicz, Y. Zhang, V. Kruzhilin, J. Li, J. Li, G. Delamare, R. Swanson, G. Buzsáki, M. Kannan, G. Vasan, M.Z. Lin, H. Zeng, T.L. Daigle, M. J. Schnitzer, Imaging high-frequency voltage dynamics in multiple neuron classes of behaving mammals, Cell 188 (2025) 4401–4423. https://creativecommunications.org/licenses/by/4.0/.
[362] H.J. Lee, Y. Jiang, J-X. Cheng, Label-free imaging of membrane potential, Current Opinion in Biomedical Engineering 12 (2019) 118–125, https://doi.org/10.1016/j.cobme.2019.11.001.
[363] Y. Zhou, E. Liu, H. Müller, B. Cui, Optical electrophysiology: towards the goal of label-free voltage imaging, J. Am. Chem. Soc. 143 (2021) 10482–10499, https://doi.org/10.1021/jacs.1c02960.
[364] Y. Yang, X. Liu, S. Wang, N. Tao, Plasmonic imaging of subcellular electromechanical deformation in mammalian cells, J. Biomed. Opt. 24 (2019) 066007, https://doi.org/10.1117/1.JBO.24.6.066007.
[365] L.D. Mosgaard, A. Gonzalez-Perez, R. Budvytyte, E. Villagran-Vargas, A. D. Jackson, T. Heimburg, Solitary electromechanical pulses in lobster neurons, Biophys. Chem. 216 (2016) 51–59, https://doi.org/10.1016/j.bpc.2016.06.005.
[366] B.W. Graf, T.S. Ralston, H-J. Ko, S.A. Boppart, Detecting intrinsic scattering changes correlated to neuron action potentials using optical coherence imaging, Opt. Express 17 (2009) 13447–13457, https://doi.org/10.1364/oe.17.013447.
[367] A.H. Badreddine, T. Jordan, I.J. Bigio, Real-time imaging of action potentials in nerves using changes in birefringence, Biomed. Opt. Express 7 (2026) 1966–1973, https://doi.org/10.1364/BOE.7.001966. ·.
[368] J.F. Barry, M.J. Turner, J.M. Schloss, D.R. Glenn, Y. Song, M.D. Lukin, H. Park, R. L. Walsworth, Optical magnetic detection of single neuron action potentials using quantum defects in diamond, Proc. Natl. Acad. Sci. U.S.A. 113 (2016) 14133–14138, https://doi.org/10.1073/pnas.1601513113.
[369] S. Oh, C. Fang-Yen, W. Choi, Z. Yaqoob, D. Fu, Y. Park, R.R. Dassari, M.S. Feld, Label-free imaging of membrane potential using membrane electromotility, Biophys. J. 103 (2012) 11–18, https://doi.org/10.1016/j.bpj.2012.05.020.
[370] T. Ling, K.C. Boyle, V. Zuckerman, T. Flores, C. Ramakrishnan, K. Deiseroth, D. Palanker, High-speed interferometric imaging reveals dynamics of neuronal deformation during the action potential, Proc. Natl. Acad. Sci. U.S.A. 117 (2020) 10278–10285, https://doi.org/10.1073/pnas.1920039117.
[371] B. Liu, H.J. Lee, D. Zhang, C-S. Liao, N. Ji, Y. Xia, J-X. Cheng, Label-free spectroscopic detection of membrane potential using stimulated Raman scattering, Appl. Phys. Lett. 106 (2015) 173704, https://doi.org/10.1063/1.4919104.
[372] H.J. Lee, D. Zhang, Y. Jiang, X. Wu, P-Y. Shih, C-S. Liao, B. Bungart, X-M. Xu, R. Drenan, E. Bartlett, J-X. Cheng, Label-free vibrational spectroscopic imaging of neuronal membrane potential, J. Phys. Chem. Lett. 8 (2017) 1932–1936, https://doi.org/10.1021/acs.jpclett.7b00575.
[373] J. Li, N. Shao, Y. Zhang, X. Liu, H. Zhang, L. Tian, K.D. Piatkevich, D. Zhang, H. J. Lee, Screening of vibrational spectroscopic voltage indicator by stimulated Raman scattering microscopy, Small Methods 9 (2025) 2402124, https://doi.org/10.1002/smtd.202402124.
[374] M. Didier, O. Tarun, P. Jourdain, P. Magistretti, S. Roke, Membrane water for probing neuronal membrane potentials and ionic fluxes at the single cell level, Nat. Commun. 9 (2018) 5287, https://doi.org/10.1038/s41467-018-07713-w.
[375] H.B. Balch, A.F. McGuire, J. Horng, H-Z. Tsai, K.K. Qi, Y-S. Duh, P.R. Forrester, M. F. Crommie, B. Cui, F. Wang, Graphene electric field sensor enables single shot

label-free imaging of bioelectrical potentials, Nano Lett. 21 (2021) 4944–4949, https://doi.org/10.1021/acs.nanolett.1c00543.
[376] F.S. Alfonso, Y. Zhou, E. Liu, A.F. McGuire, Y. Yang, H. Kantarci, D. Li, E. Copenhaver, J.B. Zuchero, H. Müller, B. Cui, Label-free optical detection of bioelectric potentials using electrochromic thin films, Proc. Natl. Acad. Sci. U.S.A. 117 (2020) 17260–17268. www.pnas.org/cgi/doi/10.1073/pnas.2002352117.
[377] Y. Zhou, E. Liu, F.S. Alfonso, Y. Yang, B. Ahmed, K. Nakasone, C. Forró, H. Müller, B. Cui, Dual-color optical recording of bioelectric potentials by polymer electrochromism, J. Am. Chem. Soc. 144 (2022) 23505–23515, https://doi.org/10.1021/jacs.2c10198.
[378] Y. Ren, C. De-Eknamkul, F. Sun, M. Ramezani, G. Gonzalez, W. Huang, J. H. Schwab, M.N. Wilson, A.J. Engler, D. Kuzum, E. Cubukcu, Trionic all-optical biological voltage sensing via quantum statistics, Nature Photonics 19 (2025) 540–548, https://doi.org/10.1038/s41566-025-01637-w.

Alfons Penzkofer was a professor of physics at the University of Regensburg from 1978 to 2008. After retirement in 2008 he continues there to work on photobiological spectroscopic research towards the characterization of photocycles of flavin and retinal based photoreceptors applied in optogenetics. He studied physics at the Technical University of Munich (diploma 1971, doctoral degree 1974, and habilitation 1977). He worked on following topics: ultrafast laser development; solid-state laser, organic dye laser, and luminescent polymer laser development; nonlinear optics; linear optical spectroscopy; nonlinear time-resolved optical spectroscopy; and optical spectroscopic characterization of artificial and biological photoreceptors.